

# Abstract

Trade-offs in Bacterial Chemotaxis and the Adaptation of Non-genetic Diversity

Nicholas W. Frankel

2015

Cell-to-cell variability is a critical issue in biomedical science and plays a role in drug resistance of bacteria and cancer, as well as in the formation of biofilms and differentiation of stem cells. Despite its broad relevance, quantitatively understanding cellular heterogeneity from its sources to its consequences is still an open challenge. The chemotaxis system of the bacterium *Escherichia coli* is an ideal model for such investigations since it is very well characterized genetically and biochemically. Chemotaxis, which is cellular movement toward favorable chemical conditions, is an important behavior across microbiology and human physiology, but the impact of cell-to-cell heterogeneity on chemotaxis is mostly unexplored.

Despite sharing the same genetically-encoded machinery, individual *E. coli* cells exhibit substantial differences in chemotactic behaviors. Here, we characterize the consequences of this behavioral heterogeneity for population performance by using modeling, simulations, and experiments. We find that there exist trade-offs in which a single chemotactic behavior cannot perform optimally in all environmental challenges. We show that, in some cases, optimal populations can benefit from non-genetic diversity to provide specialists for different tasks. We demonstrate that this is mechanistically possible through mutations in genetic regulatory sequences that alter the distribution of protein levels in the population. We therefore propose a framework for analyzing the sources, consequences, and adaptability of non-genetic diversity wherein noisy distributions of proteins give rise to heterogeneous phenotypes, which in turn give rise to differential performance and ultimately collective fitness.

# Trade-offs in Bacterial Chemotaxis and the Adaptation of Non-Genetic Diversity



A Dissertation

Presented to the Faculty of the Graduate School

of

Yale University

in Candidacy for the Degree of

Doctor of Philosophy

by

Nicholas William Frankel

Dissertation Advisor: Thierry Emonet

May 2015



© 2015 by Nicholas William Frankel

All rights reserved.

# Table of Contents

Abstract.....	i
Table of Contents.....	iv
Acknowledgements .....	viii
Disclosures .....	ix
References	ix
Part 1: Introduction.....	1
One network → Many functions	1
Figure 1–1. From proteins to fitness. ....	4
Bacterial chemotaxis as a model system	4
Figure 1–2. From proteins to fitness. ....	6
Figure 1–3. Variability in tumble bias among clonal cells on a glass slide .....	7
The tension between noise and robustness in biology	9
Population diversity as an adaptive strategy for fitness trade-offs	11
Figure 1–4. Relationship between trade-off shape and population strategy. ....	13
A multidisciplinary approach to studying diversified populations	14
References	15
Part 2: Simulations .....	25
Introduction	25
Results	26
A model to map proteins to phenotype to behavior.....	26
Figure 2–1. Comparing the model to single cell and population averaged measurements. ....	27
Different environments require different behaviors.....	28

Figure 2–2. Performance of chemotactic phenotypes depends on environmental conditions.....	31
Figure 2–3–1. Foraging performance as a function of distance to source.....	32
Figure 2–3–2. Colonization performance as a function of distance to source.....	33
Figure 2–3–3. Effect of time restrictions on foraging performance.....	34
Figure 2–3–4. Effect of source concentration on performance.....	35
Figure 2–3–5. Effect of CheY-P dynamic range on performance.....	36
<b>Trade-off strength and optimal population strategy depend on the nature of selection</b>	
.....	36
Figure 2–4. Performance trade-offs in <i>E. coli</i> chemotaxis.....	38
Figure 2–5. Effect of time limits on near/far foraging trade-offs.....	39
Figure 2–6. Selection can reshape trade-offs.....	41
Figure 2–7. Fitness trade-offs under alternate models of selection.....	42
<b>Genetic control of non-genetic diversity enables populations to resolve trade-offs.....</b>	43
Figure 2–8. Genetic control of phenotypic diversity.....	44
Figure 2–9. Optimized gene expression noise under trade-offs, very low noise permitted .....	47
Figure 2–10. Optimized gene expression noise under trade-offs with biological noise limits.....	49
<b>Potential future experiments suggested by the theory.....</b>	51
<b>Discussion</b>	52
<b>Methods</b>	53
<b>Single-cell model of chemotaxis with population-level model of gene expression .....</b>	53
Flagellar motors .....	53
Bacterial chemoreceptors .....	55
Molecular model of chemotaxis .....	56
Linearization of the molecular model.....	57
Magnitude of spontaneous fluctuations .....	58
Gene expression model .....	59
Constant biochemical parameters of the model.....	60
Phenotypic model of chemotaxis .....	62
Model parameter summary .....	64
Comparison of Molecular and Phenotypic Models .....	65

Stochastic simulations of the model in ecological challenges.....	65
Environment definitions .....	65
Simulating performance of phenotypes .....	66
Calculating fitness from performance.....	69
Optimization of gene expression parameters under trade-offs.....	70
Table 2–1. Parameter Values and Variables.....	75
References	76
<b>Part 3: Experiments .....</b>	<b>83</b>
Introduction	83
Results	84
Single-cell capillary assay exerts selection on protein level.....	84
Figure 3–1. Quantification of high-throughput capillary assay performance .....	86
Figure 3–2. Effect of variability in YFP-CheR expression on capillary assay performance.....	87
Microfluidic measurements of chemotactic behavior of cells and populations .....	88
Clonal populations segregate spatiotemporally into distinct subpopulations .....	89
Figure 3–3. Characterization of chemotaxis phenotypes in a gradient. ....	90
Figure 3–4. Acquiring and processing data from the microfluidic gradient experiment.....	91
Figure 3–5. (Opposite page) Performance of different phenotypes in different environments. ....	93
Figure 3–6. Simulations of diverse or non-diverse populations in a microfluidic device. ....	95
Figure 3–7. Diffusion of non-tumbling cells compared to wildtype drift and diffusion.....	96
Tuning protein levels changes behavior and gradient-specific performance .....	96
Figure 3–8. CheR expression affects phenotypic distribution and chemotactic performance. ....	98
Discussion	99
Methods	100
Modified high-throughput capillary assay .....	100
Microfluidic device design and fabrication .....	101

Microfluidic gradient experiment.....	103
Figure 3–9. Fabrication of two-layer PDMS microfluidic devices.....	104
Single-cell tracking and run/tumble processing.....	106
Analysis of trajectories .....	107
Simulations of cell behavior in microfluidic device geometry .....	108
Construction of strain with inducible CheR expression .....	109
Measurement of drift velocity via phase-differential microscopy .....	111
References	113
Part 4: Conclusion .....	119
A new framework, a new starting point	119
A broader perspective	120
References	121

# Acknowledgements

- ❖ My advisor, Prof. Thierry Emonet, for the mentoring.
- ❖ My thesis committee, Profs. Christine Jacobs-Wagner (chair), Thomas Pollard, and Paul Turner, for the guidance.
- ❖ The Yale MCDB department, and especially my classmates Patrick McMillen and Jill Goldstein, for putting up with my antics.
- ❖ My colleagues and co-authors in the Emonet lab, Adam Waite, Junjiajia Long, Yann Dufour, Luis Hernandez Nuñez, William Pontius, and the rest of the lab, for the tireless hours of discussion and work.
- ❖ The first graduate students of the lab, “the chemotaxis crew,” William Pontius and Michael Sneddon, for getting everything up and running with me.
- ❖ All of the faculty we’ve discussed our work with, both at Yale and other institutions.
- ❖ My wife, my parents, my sister, and my friends in the Yale Department of Music, for their support and the many needed distractions.

# Disclosures

- ~~~ This dissertation was written in partial fulfillment of the requirements for a doctor of philosophy degree.
- ~~~ All of Part 2, as well as some of Parts 1 and 4, has been closely reproduced from a recent publication (Frankel et al., 2014).
- ~~~ The formulation of the chemotaxis models in Part 2 was done with W. V. Pontius and T. Emonet. Simulations were performed using code written by T. Emonet.
- ~~~ The research in Part 3 is being prepared as a manuscript for publication (Waite\*, Frankel\*, Dufour\*, & Emonet, In preparation).
- ~~~ In Part 3, Y. S. Dufour designed the microfluidic device. A. J. Waite and I performed assays with the device. I performed the capillary assay. I created the fluorescent strain. The phase-differential microscopy experiments that used the fluorescent strain were performed by A. J. Waite. D. Chawla performed simulations under my direction.
- ~~~ Simulations and data analysis were performed at Yale High Performance Computing. Microfluidics wafer lithography was performed at Yale Becton Cleanroom.

## References

- Frankel, N. W., Pontius, W., Dufour, Y. S., Long, J., Hernandez-Nunez, L., & Emonet, T. (2014). Adaptability of non-genetic diversity in bacterial chemotaxis. *eLife*, 3. doi: 10.7554/eLife.03526
- Waite, A. W.\* , Frankel, N. W.\* , Dufour, Y. S.\* , & Emonet, T. (In preparation). Non-genetic diversity results in differential performance in bacterial chemotaxis. \*Equal contribution



# Part 1: Introduction

Bacterial chemotaxis,  
non-genetic diversity,  
functional trade-offs 

One network → Many functions

Life is not possible without reproducible interactions between vast arrays of molecules. These molecules are organized into functional networks that directly affect the viability of organisms, from the pathological signaling networks that drive cancer cells to be insensitive to the body's messages to stop growing (Hanahan & Weinberg, 2000), to the metabolic networks that give brewer's yeast the ability to ferment grape juice into wine (Quiros et al., 2013). Much of our understanding about such networks is predicated on the conceptual paradigm that one network has one function: when a cell contains the proteins of a network, that network will execute its function in a predictable and unvarying manner. This function may be broken or altered by genetic mutations in network genes, but as a first approximation it is assumed that cells possessing the same genetic material encoding a certain network will behave approximately the same way.

In fact, the actual concentration and ratios of proteins within a network can dramatically change the function of a biological network. One way in which this function can change is in how the network behaves in time, which is to say its dynamics (Alexander, Kim, Emonet, & Gerstein, 2009). An on-off switching behavior could change to an oscillatory behavior, and the distinction between these is crucial for proper function (Ferrell, Tsai, & Yang, 2011). The former behavior may be more relevant to an organism's metabolic response to the appearance or disappearance of a certain nutrient in the environment, whereas the second type of response

is necessary to correctly coordinate the growth and division process of the cell cycle. Confusing these types of behaviors could hypothetically result in the starvation of an organism or the development of hyperproliferative cancerous cells (Hanahan & Weinberg, 2000).

The sensitivity of network dynamics—and consequently network function—to molecular quantities would not have a substantial impact on organismal behavior were organisms able to perfectly ensure that every cell had an exactly predictable number of molecules. In reality, cells make many “errors”: different cells that have the same genetic material are nonetheless observed to have different numbers of proteins (and other components) due to random fluctuations (Paulsson, 2004; Raser & O’Shea, 2005). This biological “noise” raises the question of whether variations in molecular abundance can alter the function of biological networks and consequently the fitness of the organism. Indeed, cell-to-cell variability is a critical issue in biomedical science, as it plays a role in drug resistance of bacteria (Balaban, Merrin, Chait, Kowalik, & Leibler, 2004) and cancer (Spencer, Gaudet, Albeck, Burke, & Sorger, 2009), as well as in the formation of biofilms (P. S. Stewart & Franklin, 2008) and differentiation of cells during development and tumorigenesis (Huang, 2009).

This dissertation at the broadest level seeks to establish a linkage between proteins and fitness in single cells and explicitly consider the ramifications of cell-to-cell variations in molecular numbers for the survival of cellular populations. It is my hope that the framework that I establish here will be useful in the future to examine medically- and industrially-relevant biological systems in greater detail by revising our understanding from “one network → one function” to “one network → many functions.”

Specifically, the conceptual framework of this dissertation (Figure 1–1) describes how a distribution of different protein levels among genetically-identical cells gives rise to different cells in the same population (or organism) having different phenotypes. Here, I largely define phenotypes, or phenotypic parameters, as properties of cells that characterize the response of the individual to different stimuli in space and time. As such these phenotypic parameters determine how a cell will perform in different environmentally-imposed tasks. Finally,

evolutionary selection acts on the cells' performance, bestowing proliferative rewards or doling out population-culling punishment depending on how well or how poorly cells perform in a given environmental challenge, to determine fitness. This dissertation is mainly dedicated to understanding how cell-to-cell variability propagates through these different quantities—from variability in protein numbers to phenotypes to performance to fitness—and how this propagation determines the survival of populations.

This conceptual flow diverges from the conventionally posed relationship between genotype, phenotype, and fitness in a few respects and for a few reasons. Since I will focus on non-genetic variation (noisy differences in protein amounts due only to random fluctuations rather than individually borne mutations), the impact of genotypic variability will be ignored. Second, “phenotype” conventionally defined is too broad for the purpose of these investigations. I believe that it is more precise to separate the part of phenotype that concerns cellular response characteristics (“phenotype”), from the part of the phenotype that describes the behavior of an organism in a specific environment (“performance”), from the part of the phenotype that describes the growth or death rate resulting from the behavior (“fitness”). In total, these three subgroups of the “conventional phenotype”—phenotype, performance, and fitness—will shape the total fitness of an entire noisy population over time, which I define in Part 2 as “big”  $F$ .

As I will show in this dissertation, this framework affords us a new level of detail that permits the interrogation of new and interesting questions. How does cell-to-cell variability in protein levels affect population fitness, and are there situations in which more or less variability is advantageous? How can such variability be controlled biologically, in other words, how could mutations lead to competitive adaptation of cell-to-cell variability when said variability is non-genetic in origin? In order to address these broad questions, I will use the well-characterized *E. coli* chemotaxis system as a biological model and borrow extensively from physics and biology to create a multidisciplinary approach from simulations to experiments.

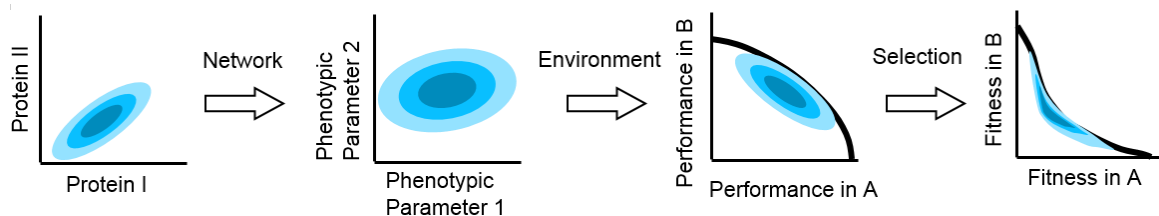


**Figure 1–1. From proteins to fitness.**

From a single genotype, noise in gene expression leads to a distribution of proteins expression levels (blue shaded contours in protein space; left); network design determines how proteins quantities map onto phenotypic parameters (middle left); the performance of all possible phenotypic parameter values across environments will determine the outer boundary of performance space (middle right); selection bestows a fitness reward based on performance and will reshape the performance front into the Pareto front (thick black line), which, for optimal fitness, the population distribution should be constrained to (right).

## Bacterial chemotaxis as a model system

Many cells are able to move around their environment, and some can use information that they sense to move toward favorable conditions and away from unfavorable ones. This behavior, called chemotaxis for movement in response to chemicals, phototaxis for light, thermotaxis for temperature, aerotaxis for dissolved gases, *et cetera*, allows bacteria to find nutrition and avoid toxins. Pathogenic bacteria use chemotaxis to infect host tissues (Lane et al., 2005; Stecher et al., 2004; M. K. Stewart & Cookson, 2012; Sze, Zhang, Kariu, Pal, & Li, 2012). Many cells in our bodies also perform chemotaxis, from nerve cells to skin cells to cells of the immune system and sperm (Eisenbach & Lengeler, 2004), making it a key cell behavior in development, disease, and reproduction.

One of the earliest scientists to observe chemotaxis in bacteria experimentally, the botanist Willhelm Pfeffer (1845–1920), famously decreed “Bewegung ist Leben [Movement is life]!”

Perhaps it is because of our association of movement with life that chemotaxis in the bacterium *Escherichia coli* has garnered as much attention as it has from such diverse fields, inviting multidisciplinary collaborations as early as the late 1960s (Hazelbauer, 2012). Constant study since then has made the chemotaxis system in *E. coli* not only one of the best-characterized model systems biologically, but also one of the best-understood theoretically thanks to the constant involvement of physicists, mathematicians and engineers over the decades. This synergy between theory and biology has made *E. coli* chemotaxis an extremely fruitful system for advances in theoretical and systems biology. (Incidentally, “Bewegung ist Leben” is now the name of a fitness club in Austria.)

The system itself consists of a small network of proteins that, although simple, contains many of the fundamental features of larger and more complex systems. *E. coli* uses a single chemotaxis protein network to navigate gradients of chemical attractants and repellents, as well as gradients of temperature, oxygen, and pH (Sourjik & Wingreen, 2012) (Figure 1–2A). The core of the network is a two-component signal transduction system that carries chemical information gathered by transmembrane receptors to flagellar motors responsible for cell propulsion. A second group of proteins allows the cells to physiologically adapt to changing background signal levels, allowing them to track signal gradients over many orders of magnitude. While different receptors allow cells to sense different signals, all signals are then processed through the same set of four cytoplasmic proteins responsible for signal transduction and adaptation. The mechanistic details of these protein–protein interactions (Kentner & Sourjik, 2009) are thoroughly characterized. Protein structures have been solved, interaction domains identified, biochemical constants fit from data.

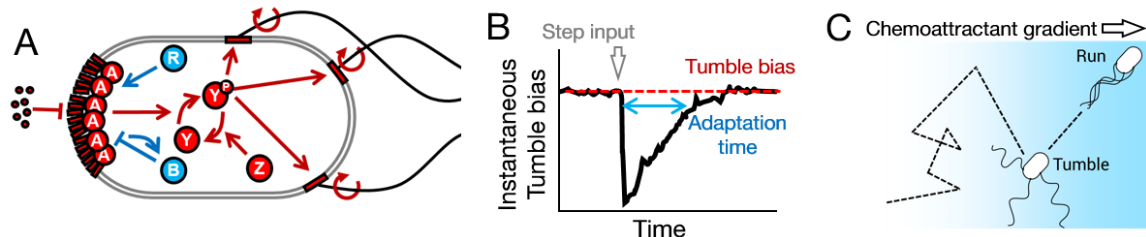


**Figure 1–2. From proteins to fitness.**

**A.** The cell receives extracellular ligand signals through transmembrane receptors. Changes in signal are rapidly communicated to the flagellar motors through the kinase CheA and response regulator CheY. CheZ opposes the kinase activity of CheA. At a slower timescale, the activity of the receptor complex physiologically adapts to its steady-state activity through the antagonistic actions of CheR and CheB. **B.** Cartoon diagram of the response of the system to transient step-stimulus and definition of the key phenotypic parameters of the system. Without stimulation, the system has a steady-state tumble bias, or fraction of time spent tumbling. Upon stimulus with a step, CheY activity and therefore tumble bias drops and the cell starts running more, then slowly adapts back to the steady-state with a characteristic timescale (adaptation time). The steady-state tumble bias and adaptation time are tuned by the concentrations of proteins in A. **C.** Cells explore their environment by alternating between straight runs and direction-changing tumbles. When cells sense that they are traveling up a concentration gradient, they suppress tumbles to increase run length. Precisely how a cell navigates a gradient depends on its phenotypic parameters in B.

The cell explores its environment in a run-and-tumble fashion (Berg & Brown, 1972). The flagella that cells use to move through the environment that are driven by rotary motors. Counterclockwise rotation of the flagella promotes the formation of a helical bundle that propels the cell forward in a run, whereas clockwise rotation of one or more flagellar motors interrupts the run with a brief direction-changing tumble. It has been observed that clonal cells, grown and observed under the same conditions without stimulation, will differ substantially in the fraction of time the motors spend in the clockwise state, or clockwise bias (Park et al., 2010). Analogously, tumble bias is defined as the fraction of time spent tumbling

Variability in tumble bias can also be observed in a clonal population by tracking the motion of cells, picked from a single colony, on a microscope slide. Even without stimulation, differences in swimming patterns emerge almost instantly. Cells with high tumble bias make crumpled tracks causing very little displacement, whereas cell with lower tumble bias swim much straighter for long periods, exploring their local environment more freely, albeit potentially less thoroughly (Figure 1–3). Such obvious differences between clonal cells (grown and observed in the same way and arising from no additional treatment) visually states the spatial impact of cell-to-cell variability in phenotypes. (Methods in Part 4.)

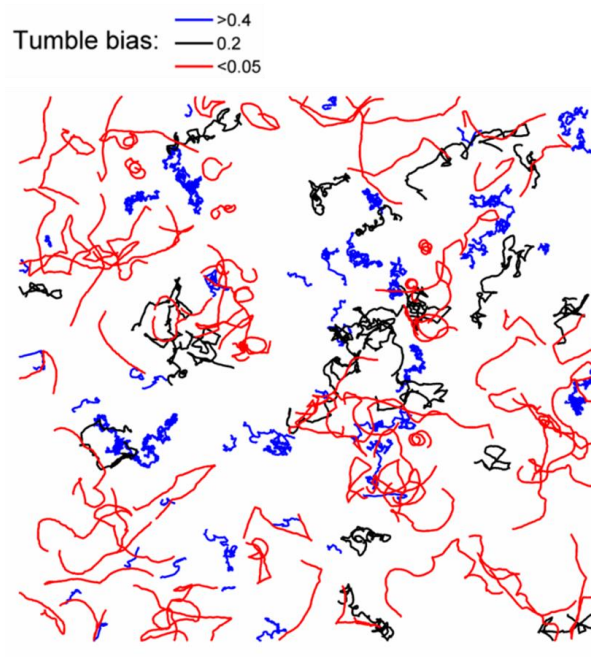


**Figure 1–3. Variability in tumble bias among clonal cells on a glass slide**

Two-minute-long movie of cells captured at 10x. The frame is 1.3 mm x 1.3 mm with a depth of approximately 10  $\mu\text{m}$ . Cells were tracked and tumble bias assigned as described in Part 4, Methods. Low, average, and high are so named because a tumble bias of 0.2 is roughly the mean tumble bias among wildtype cells.

The central logic of *E. coli* chemotaxis is to transiently decrease tumble bias in response to an increase in attractant signal (Figure 1–2B). This approach allows cells to climb gradients of attractants by lengthening runs up the gradient (Figure 1–2C). The adaptation process that maintains receptor sensitivity is mediated by the covalent modification of the chemoreceptors through addition and subtraction of methyl groups by the enzymes CheR and CheB, respectively. Like tumble bias, the timescale of this adaptation process has been observed to vary among clonal cells (Spudich & Koshland, 1976).

This observation was made by tethering cells to slides by their flagella and watching their bodies spin in different directions in response to the delivery of an attractant. Individuals took more or less to return to steady-state behavior following a strong dose of attractant. The visual nature of this study, which may have popularized the now-standard term “non-genetic individuality,” inspired scientific essayist Lewis Thomas to expressively describe the cells in this now oft-quoted way:

If you watch them closely, tethered by their flagellae to the surface of an antibody-coated slide, you can tell them from each other by the way they twirl, as accurately as though they had different names. (Thomas, 1979)

Heterogeneity in protein levels is a compelling hypothesis for this behavioral variability. The intracellular levels of CheR and CheB proteins are known to change both adaptation timescale and tumble bias (Alon, Surette, Barkai, & Leibler, 1999). Chemoreceptor activity is communicated to the motors via phosphorylation of the response regulator CheY to form CheY-P by the receptor-associated kinase CheA. CheZ opposes the action of CheA by dephosphorylating CheY-P. Consequently, the balance of CheA and CheZ affects tumble bias. Furthermore, the total amount of CheY in the cell will determine the range of possible CheY-P levels, and due to noise in the expression of CheY (Kollmann, Lovdok, Bartholome, Timmer, & Sourjik, 2005) this dynamic range will likewise vary between clonal cells.

These three phenotypic parameters—tumble bias, adaptation time, and CheY-P dynamic range—are the main determinants of how *E. coli* performs chemotaxis. These in turn depend

on the quantities of chemotaxis proteins within each individual cell. The abundance of these proteins therefore determine the capability of the individual to navigate its environment, regardless of the type of signal being followed.

## The tension between noise and robustness in biology

The central dogma of biology describes how proteins are made, translated from the molecular instructions of mRNA molecules which themselves are transcribed from a DNA template (Crick, 1970). As this process unfolds in time through the actions of RNA polymerase, ribosomes, tRNAs, and a massive cast of regulators, it is tempting to view the process as an automatic watch mechanism—everything happening precisely according to plan. The agents involved herein move randomly, however, not deterministically, and, as with other stochastic systems like street traffic and stock markets, there will necessarily be irregularities, for better or for worse. As a result of these stochastic nonlinear dynamics, different cells with the same gene will end up with different numbers of the protein that the gene encodes.

Observations of cell-to-cell variability necessarily require single-cell measurements. Although initially observed in early studies using flow cytometry (Darzynkiewicz, Crissman, Traganos, & Steinkamp, 1982), this phenomenon only began to be described in detail in the last decade or so with the rise of quantitative single-cell and single-molecule microscopy, made possible by advances in fluorescent dyes, proteins, and microscopes. By carefully measuring the dynamics of protein synthesis (Cai, Friedman, & Xie, 2006) and the distribution of protein quantities in clonal populations (Swain, Elowitz, & Siggia, 2002), we now understand that there are several contributors to cell-to-cell variation (Paulsson, 2004; Raser & O'Shea, 2005). The transcription process and the translation process introduce different sources of noise, as does the randomly unequal partitioning of cellular contents during cell division. Factors affecting the variance include the particular interaction between RNA polymerase and the region of DNA that initiates transcription, or promoter, the analogous relationship between the ribosome and its binding sites, and the localization pattern of a protein in the cell when

it comes time to divide. The average expression level of a protein will also affect the variance of its expression levels in a clonal population.

In the *E. coli* chemotaxis system, measurements of expression of fluorescently-labeled chemotaxis proteins CheA and CheY from the native chromosomal loci have shown substantial cell-to-cell variation in protein concentration (Kollmann et al., 2005). That observation combined with the relationship between protein abundance and cellular phenotype led us to hypothesize as others have (Levin, Morton-Firth, Abouhamad, Bourret, & Bray, 1998) that gene expression noise is likely responsible for much of the observed non-genetic behavioral diversity in clonal populations.

With the rising awareness of non-genetic variability in protein levels, biologists, physicists, and engineers alike have begun asking questions of how organisms could maintain proper function in the face of these fluctuations. In other words, how can biological systems be robust to protein noise? Evolutionary biologists have grappled with a similar question for quite a long time in a different form, seeking to understand how populations of viruses or bacteria can balance the benefits of high mutation rates in granting evolutionary access to new phenotypes with the downsides of sometimes wrecking core systems (Montville, Froissart, Remold, Tenaillon, & Turner, 2005). Evolutionary robustness defined as such is more concerned with the insensitivity of a biological function to mutation. Now, biological robustness in the systems biology sense refers to the maintenance of function in the face of non-genetic variations (Barkai & Leibler, 1997).

*E. coli* chemotaxis has been successfully used as a model system to broach the robustness question of systems biology. Chemotaxis genes are chromosomally organized in operons—that is, expression of multiple genes is driven by common promoters. This organization is known to introduce correlations in cell-to-cell variability, wherein total amounts of proteins may vary from cell to cell, but the ratio of one protein to another will vary substantially less (Lovdok et al., 2009). Combined with the negative integral feedback design of the protein network, this conservation of protein ratios greatly reduces the occurrence of cells with “non-functional”

parameter values—for instance, those that only run or only tumble—and maintains the precision of the physiological adaptation process (Alon et al., 1999; Barkai & Leibler, 1997; Kollmann et al., 2005; Lovdok, Kollmann, & Sourjik, 2007; Yi, Huang, Simon, & Doyle, 2000). These parameter values are considered “non-functional” for chemotaxis since, without a combination of both runs and tumbles, it is not possible to bias a random walk. For these and other reasons (Endres & Wingreen, 2006; Mears, Koirala, Rao, Golding, & Chemla, 2014; Oleksiuk et al., 2011; Schulmeister, Grosse, & Sourjik, 2011; Sneddon, Pontius, & Emonet, 2012; Vladimirov, Lebiedz, & Sourjik, 2010), chemotaxis in *E. coli* is often said to be robust—in the systems biology sense.

## Population diversity as an adaptive strategy for fitness trade-offs

Within the range of “functional” behaviors, substantial variability exists, and the fact that this variability has not been selected against raises the question of whether it might serve an adaptive function. Population diversity is known to be an adaptive strategy for environmental uncertainty (Donaldson-Matasci, Lachmann, & Bergstrom, 2008; Haccou & Iwasa, 1995; Kussell & Leibler, 2005). For chemotaxis this would suggest that different cells in the population may hypothetically have behaviors specialized to navigate different environments. Indeed, past simulations (Dufour, Fu, Hernandez-Nunez, & Emonet, 2014; Jiang, Qi, & Tu, 2010; Vladimirov, Lovdok, Lebiedz, & Sourjik, 2008) have shown that the speed at which cells climb exponential gradients depends on tumble bias and adaptation time, and experiments using the capillary assay—an experiment that tests cells’ ability to find the mouth of a pipette filled with attractant—have shown that inducing expression of CheR and CheB at different levels changes the chemotactic response (Park, Guet, Emonet, & Cluzel, 2011). In order to understand the impact of these findings on population diversity, we must place them in an ecological context.

Relatively little is known about the ecology of *E. coli* chemotaxis, but it is probable that they, like other freely swimming bacteria, encounter a wide variety of environments, from

gradients whipped up by turbulent eddies (Taylor & Stocker, 2012) to those generated during the consumption of large nutrient caches (Blackburn, Fenchel, & Mitchell, 1998; Saragosti et al., 2011). In each case, variations in environmental parameters, such as in the amount of turbulence, the diffusivity of the nutrients, or the number of cells, will change the steepness of these gradients over orders of magnitude (Seymour, Marcos, & Stocker, 2009; Stocker, Seymour, Samadani, Hunt, & Polz, 2008; Taylor & Stocker, 2012). Still other challenges include maintaining cell position near a source (Clark & Grant, 2005), exploration in the absence of stimuli (Matthaus, Jagodic, & Dobnikar, 2009), navigating gradients of multiple compounds (Kalinin, Neumann, Sourjik, & Wu, 2010), navigating toward sites of infection (Terry, Williams, Connolly, & Ottemann, 2005), and evading host immune cells (Stossel, 1999).

Considering all of these eventualities, it would seem unlikely that a population consisting only of a single phenotype would be well-suited to all environments. If, for instance, two different environments require different specialists, this could lead to performance trade-offs wherein mutual optimization of both tasks is not possible (Figure 1–1, panel 3). Depending on how survival and reproduction depend on their performance, performance trade-offs could lead to fitness trade-offs (Figure 1–1, panel 4), which are known to have direct consequences for the evolution of diversity (Donaldson-Matasci et al., 2008; Haccou & Iwasa, 1995; Kussell & Leibler, 2005; Shoval et al., 2012).

Fitness trade-offs can lead to the development of multiple biological modules (Rueffler, Hermission, & Wagner, 2012). Some modules, like new limbs, may be permanent fixtures, while others, like metabolic pathways, may be switched on and off, either in response to the environment as it changes, or stochastically in anticipation of environmental fluctuation. This latter case, often called “bet-hedging” (Veening, Smits, & Kuipers, 2008), is a strategy used by bacteria to avoid extinction from antibiotic stress during infection (M. K. Stewart & Cookson, 2012) and has evolved in the laboratory under fluctuating selection (Beaumont, Gallie, Kost, Ferguson, & Rainey, 2009). In these examples, environmental extremes lead to discrete partitioning of the population. It is unknown whether there is an intermediate case, a possible

evolutionary stepping stone, in which a single function is continuously diversified in the population without the formation of a wholly different state.

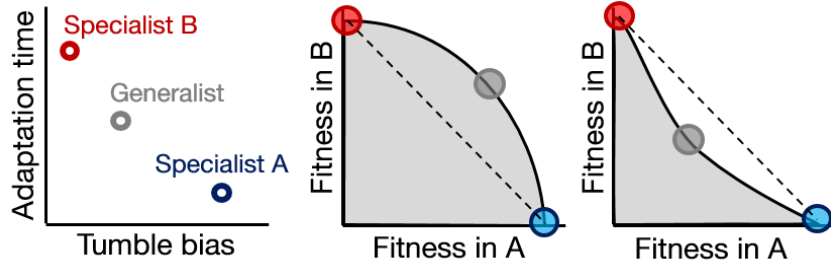


**Figure 1–4. Relationship between trade-off shape and population strategy.**

Left: Two environments, A and B, select for different optimal phenotypes, specialist A and specialist B (blue and red circles). The generalist phenotype (gray circle) performs well, but not optimally, in both environments. Middle and right: Trade-off plots. Gray region: fitness set composed of the fitness of all possible phenotypes in each environment; Black line: Pareto front of most competitive phenotypes; Dashed line: fitness of mixed populations of specialists; Circles: fitness of phenotypes corresponding the circles in the left plot. Middle: In a weak trade-off (convex front), the optimal population distribution will consist purely of a generalist phenotype that lies on the Pareto front. Right: In a strong trade-off (concave front), the optimal population will be distributed between the specialists for the different environments. Here, the fitness of a mixed population of specialists (dashed line), exceeds that of the generalist in both environments.

To understand the consequences of fitness trade-offs, we must analyze whether they are weak or strong. Such analysis will reveal in which cases populations should adopt homogenous or diversified strategies, respectively, for optimal collective function. For a two-environment trade-off, the fitness of all possible phenotypes in both environments occupies a region in two-dimensional fitness space called the fitness set (Levins, 1962) (Figure 1–4, gray regions). Specialists in this set will be located at the region's maxima in each axis (red and blue circles).

Between the specialists, the outer boundary of the set is called the Pareto front (Shoval et al., 2012): a group of phenotypes that have jointly optimized both tasks (black line). A generalist phenotype will occupy a position on this front (gray circle). When this front is convex (middle panel), the generalist has higher joint performance. A concave front (right panel), however, is optimized by a mixed strategy of specialists, due to the fact that a combination of specialists (dashed line, the “extended fitness set”) will exceed the fitness of any phenotype in the fitness set (Donaldson-Matasci et al., 2008).

## A multidisciplinary approach to studying diversified populations

Arising from the abovementioned literature, I formulate several hypotheses :

- ❖ Stochastically generated cell-to-cell variations in protein abundance will lead to diversity in chemotactic behaviors.
- ❖ The diversity of possible chemotactic challenges will exert trade-off problems on the chemotaxis network, potentially requiring diversified populations if the trade-offs are strong.
- ❖ Mutations that alter cell-to-cell variability will allow for adaptive diversified strategies in the face of trade-offs.

To test these hypotheses, it is necessary to understand our model system in many ways: as a mutable genotype, as a collection of biomolecules, as a dynamical system, as a strategic agent, and as a population of individuals each of which may be a little different. Each of these facets will borrow techniques from applicable fields: evolutionary biology, cell biology, physics, engineering, and systems biology. While many of the techniques employed are now long established, bringing them together as I have in this dissertation will be new.

The research content of the dissertation consists of two parts to reflect the two fundamental styles of research that I will be combining: simulations and experiments. In the following Part 2, I will use simulations of bacteria in different environments to demonstrate that no single phenotype performs optimally in all environments, leading to trade-off problems in

chemotactic behaviors, which was recently published (Frankel et al., 2014). Using an experimentally-constrained model of noisy gene expression in a clonal population, I will theoretically predict that cells with different protein levels will have different chemotactic behaviors, and that mutations that alter the noise in gene expression can permit adaptation to resolve chemotactic trade-offs at the population level.

This theoretical work leads to several testable predictions which I then begin to study experimentally in the final research part, namely that clonal populations should have functional diversity in chemotaxis behaviors, and that different chemotactic challenges should require different chemotactic behaviors for optimal performance. To measure the diversity in chemotactic behaviors in clonal populations and connect it to diversity in protein levels, I describe the development of assays to separate cells based on chemotactic performance and demonstrate cases in which performance depends on cell phenotype and on the level of expression of chemotaxis proteins (Waite\*, Frankel\*, Dufour\*, & Emonet, In preparation). These results are consistent with predictions developed in the theoretical section and other recent modeling work (Dufour et al., 2014).

The final Part 4 of the dissertation brings together findings from theory and experiments to describe the impact of the dissertation on future research on this topic and beyond. In the end, my goal to use this well-characterized model system to establish the efficacy and broaden the awareness of what I hope will be a useful framework for the study of diversity in other systems—biological and otherwise.

## References

- Alexander, R. P., Kim, P. M., Emonet, T., & Gerstein, M. B. (2009). Understanding modularity in molecular networks requires dynamics. *Sci Signal*, 2(81), pe44. doi: 10.1126/scisignal.281pe44
- Alon, U., Surette, M. G., Barkai, N., & Leibler, S. (1999). Robustness in bacterial chemotaxis. *Nature*, 397(6715), 168-171.

- Balaban, N. Q., Merrin, J., Chait, R., Kowalik, L., & Leibler, S. (2004). Bacterial persistence as a phenotypic switch. *Science*, 305(5690), 1622-1625. doi: 10.1126/science.1099390
- Barkai, N., & Leibler, S. (1997). Robustness in simple biochemical networks. *Nature*, 387(6636), 913-917.
- Beaumont, H. J. E., Gallie, J., Kost, C., Ferguson, G. C., & Rainey, P. B. (2009). Experimental evolution of bet hedging. *Nature*, 462(7269), 90-U97. doi: Doi 10.1038/Nature08504
- Berg, H. C., & Brown, D. A. (1972). Chemotaxis in *Escherichia coli* analysed by three-dimensional tracking. *Nature*, 239(5374), 500-504.
- Blackburn, N., Fenchel, T., & Mitchell, J. (1998). Microscale nutrient patches in planktonic habitats shown by chemotactic bacteria. *Science*, 282(5397), 2254-2256. doi: DOI 10.1126/science.282.5397.2254
- Cai, L., Friedman, N., & Xie, X. S. (2006). Stochastic protein expression in individual cells at the single molecule level. *Nature*, 440(7082), 358-362. doi: 10.1038/nature04599
- Clark, D. A., & Grant, L. C. (2005). The bacterial chemotactic response reflects a compromise between transient and steady-state behavior. *Proc Natl Acad Sci U S A*, 102(26), 9150-9155. doi: 10.1073/pnas.0407659102
- Crick, F. (1970). Central dogma of molecular biology. *Nature*, 227(5258), 561-563.
- Darzynkiewicz, Z., Crissman, H., Traganos, F., & Steinkamp, J. (1982). Cell heterogeneity during the cell cycle. *J Cell Physiol*, 113(3), 465-474. doi: 10.1002/jcp.1041130316
- Donaldson-Matasci, M. C., Lachmann, M., & Bergstrom, C. T. (2008). Phenotypic diversity as an adaptation to environmental uncertainty. *Evolutionary Ecology Research*, 10(4), 493-515.
- Dufour, Y. S., Fu, X., Hernandez-Nunez, L., & Emonet, T. (2014). Limits of feedback control in bacterial chemotaxis. *PLoS Comput Biol*, 10(6), e1003694. doi: 10.1371/journal.pcbi.1003694
- Eisenbach, Michael, & Lengeler, Joseph W. (2004). *Chemotaxis*. London: Imperial College Press.

- Endres, R. G., & Wingreen, N. S. (2006). Precise adaptation in bacterial chemotaxis through "assistance neighborhoods". *Proceedings of the National Academy of Sciences of the United States of America*, 103(35), 13040-13044. doi: 10.1073/pnas.0603101103
- Ferrell, J. E., Jr., Tsai, T. Y., & Yang, Q. (2011). Modeling the cell cycle: why do certain circuits oscillate? *Cell*, 144(6), 874-885. doi: 10.1016/j.cell.2011.03.006
- Frankel, N. W., Pontius, W., Dufour, Y. S., Long, J., Hernandez-Nunez, L., & Emonet, T. (2014). Adaptability of non-genetic diversity in bacterial chemotaxis. *eLife*, 3. doi: 10.7554/eLife.03526
- Haccou, P., & Iwasa, Y. (1995). Optimal Mixed Strategies in Stochastic Environments. *Theoretical Population Biology*, 47(2), 212-243. doi: DOI 10.1006/tpbi.1995.1009
- Hanahan, D., & Weinberg, R. A. (2000). The hallmarks of cancer. *Cell*, 100(1), 57-70.
- Hazelbauer, G. L. (2012). Bacterial chemotaxis: the early years of molecular studies. *Annu Rev Microbiol*, 66, 285-303. doi: 10.1146/annurev-micro-092611-150120
- Huang, S. (2009). Non-genetic heterogeneity of cells in development: more than just noise. *Development*, 136(23), 3853-3862. doi: Doi 10.1242/Dev.035139
- Jiang, L. L., Qi, O. Y., & Tu, Y. H. (2010). Quantitative Modeling of Escherichia coli Chemotactic Motion in Environments Varying in Space and Time. *Plos Computational Biology*, 6(4). doi: ARTN e1000735 DOI 10.1371/journal.pcbi.1000735
- Kalinin, Y., Neumann, S., Sourjik, V., & Wu, M. M. (2010). Responses of Escherichia coli Bacteria to Two Opposing Chemoattractant Gradients Depend on the Chemoreceptor Ratio. *Journal of Bacteriology*, 192(7), 1796-1800. doi: Doi 10.1128/Jb.01507-09
- Kentner, D., & Sourjik, V. (2009). Dynamic map of protein interactions in the Escherichia coli chemotaxis pathway. *Molecular Systems Biology*, 5. doi: Artn 238 Doi 10.1038/Msb.2008.77
- Kollmann, M., Lovdok, L., Bartholome, K., Timmer, J., & Sourjik, V. (2005). Design principles of a bacterial signalling network. *Nature*, 438(7067), 504-507.

- Kussell, E., & Leibler, S. (2005). Phenotypic diversity, population growth, and information in fluctuating environments. *Science*, 309(5743), 2075-2078. doi: 10.1126/science.1114383
- Lane, M. C., Lockatell, V., Monterosso, G., Lamphier, D., Weinert, J., Hebel, J. R., . . . Mobley, H. L. (2005). Role of motility in the colonization of uropathogenic Escherichia coli in the urinary tract. *Infect Immun*, 73(11), 7644-7656. doi: 10.1128/IAI.73.11.7644-7656.2005
- Levin, M. D., Morton-Firth, C. J., Abouhamad, W. N., Bourret, R. B., & Bray, D. (1998). Origins of individual swimming behavior in bacteria. *Biophysical journal*, 74(1), 175-181. doi: 10.1016/S0006-3495(98)77777-X
- Levins, R. (1962). Theory of Fitness in a Heterogeneous Environment .1. Fitness Set and Adaptive Function. *American Naturalist*, 96(891), 361-&. doi: Doi 10.1086/282245
- Lovdok, L., Bentele, K., Vladimirov, N., Muller, A., Pop, F. S., Lebiedz, D., . . . Sourjik, V. (2009). Role of translational coupling in robustness of bacterial chemotaxis pathway. *PLoS Biol*, 7(8), e1000171. doi: 10.1371/journal.pbio.1000171
- Lovdok, L., Kollmann, M., & Sourjik, V. (2007). Co-expression of signaling proteins improves robustness of the bacterial chemotaxis pathway. *Journal of Biotechnology*, 129(2), 173-180. doi: DOI 10.1016/j.jbiotec.2007.01.024
- Matthaus, F., Jagodic, M., & Dobnikar, J. (2009). E. coli Superdiffusion and Chemotaxis Search Strategy, Precision, and Motility. *Biophysical Journal*, 97(4), 946-957. doi: DOI 10.1016/j.bpj.2009.04.065
- Mears, P. J., Koirala, S., Rao, C. V., Golding, I., & Chemla, Y. R. (2014). Escherichia coli swimming is robust against variations in flagellar number. *eLife*, 3, e01916. doi: 10.7554/eLife.01916
- Montville, R., Froissart, R., Remold, S. K., Tenaillon, O., & Turner, P. E. (2005). Evolution of mutational robustness in an RNA virus. *PLoS Biol*, 3(11), e381. doi: 10.1371/journal.pbio.0030381

- Oleksiuk, O., Jakovljevic, V., Vladimirov, N., Carvalho, R., Paster, E., Ryu, W. S., . . . Sourjik, V. (2011). Thermal robustness of signaling in bacterial chemotaxis. *Cell*, *145*(2), 312-321. doi: 10.1016/j.cell.2011.03.013
- Park, H., Guet, C. C., Emonet, T., & Cluzel, P. (2011). Fine-Tuning of Chemotactic Response in *E. coli* Determined by High-Throughput Capillary Assay. *Current Microbiology*, *62*(3), 764-769. doi: DOI 10.1007/s00284-010-9778-z
- Park, H., Pontius, W., Guet, C.C., Marko, J.F., Emonet, T., & Cluzel, P. (2010). Interdependence of behavioural variability and response to small stimuli in bacteria. *Nature*, *468*(7325), 819-823.
- Paulsson, J. (2004). Summing up the noise in gene networks. *Nature*, *427*(6973), 415-418. doi: 10.1038/nature02257
- Quiros, M., Martinez-Moreno, R., Albiol, J., Morales, P., Vazquez-Lima, F., Barreiro-Vazquez, A., . . . Gonzalez, R. (2013). Metabolic flux analysis during the exponential growth phase of *Saccharomyces cerevisiae* in wine fermentations. *PLoS One*, *8*(8), e71909. doi: 10.1371/journal.pone.0071909
- Raser, J. M., & O'Shea, E. K. (2005). Noise in gene expression: origins, consequences, and control. *Science*, *309*(5743), 2010-2013. doi: 10.1126/science.1105891
- Rueffler, C., Hermisson, J., & Wagner, G. P. (2012). Evolution of functional specialization and division of labor. *Proceedings of the National Academy of Sciences of the United States of America*, *109*(6), E326-E335. doi: DOI 10.1073/pnas.1110521109
- Saragosti, J., Calvez, V., Bournaveas, N., Perthame, B., Buguin, A., & Silberzan, P. (2011). Directional persistence of chemotactic bacteria in a traveling concentration wave. *Proceedings of the National Academy of Sciences of the United States of America*, *108*(39), 16235-16240. doi: DOI 10.1073/pnas.1101996108
- Schulmeister, S., Grosse, K., & Sourjik, V. (2011). Effects of receptor modification and temperature on dynamics of sensory complexes in *Escherichia coli* chemotaxis. *Bmc Microbiology*, *11*. doi: Artn 222 Doi 10.1186/1471-2180-11-222

Seymour, J. R., Marcos, & Stocker, R. (2009). Resource Patch Formation and Exploitation throughout the Marine Microbial Food Web. *American Naturalist*, 173(1), E15-E29. doi: Doi 10.1086/593004

Shoval, O., Sheftel, H., Shinar, G., Hart, Y., Ramote, O., Mayo, A., . . . Alon, U. (2012). Evolutionary trade-offs, Pareto optimality, and the geometry of phenotype space. *Science*, 336(6085), 1157-1160. doi: 10.1126/science.1217405

Sneddon, M. W., Pontius, W., & Emonet, T. (2012). Stochastic coordination of multiple actuators reduces latency and improves chemotactic response in bacteria. *Proceedings of the National Academy of Sciences of the United States of America*, 109(3), 805-810. doi: 10.1073/pnas.1113706109

Sourjik, V., & Wingreen, N. S. (2012). Responding to chemical gradients: bacterial chemotaxis. *Curr Opin Cell Biol*, 24(2), 262-268. doi: 10.1016/j.ceb.2011.11.008

Spencer, S. L., Gaudet, S., Albeck, J. G., Burke, J. M., & Sorger, P. K. (2009). Non-genetic origins of cell-to-cell variability in TRAIL-induced apoptosis. *Nature*, 459(7245), 428-432. doi: 10.1038/nature08012

Spudich, J. L., & Koshland, D. E. (1976). Non-Genetic Individuality - Chance in Single Cell. *Nature*, 262(5568), 467-471.

Stecher, B., Hapfelmeier, S., Muller, C., Kremer, M., Stallmach, T., & Hardt, W. D. (2004). Flagella and chemotaxis are required for efficient induction of *Salmonella enterica* serovar *Typhimurium* colitis in streptomycin-pretreated mice. *Infect Immun*, 72(7), 4138-4150. doi: 10.1128/IAI.72.7.4138-4150.2004

Stewart, M. K., & Cookson, B. T. (2012). Non-genetic diversity shapes infectious capacity and host resistance. *Trends in Microbiology*, 20(10), 461-466. doi: DOI 10.1016/j.tim.2012.07.003

Stewart, P. S., & Franklin, M. J. (2008). Physiological heterogeneity in biofilms. *Nat Rev Microbiol*, 6(3), 199-210. doi: 10.1038/nrmicro1838

- Stocker, R., Seymour, J. R., Samadani, A., Hunt, D. E., & Polz, M. F. (2008). Rapid chemotactic response enables marine bacteria to exploit ephemeral microscale nutrient patches. *Proceedings of the National Academy of Sciences of the United States of America*, 105(11), 4209-4214. doi: DOI 10.1073/pnas.0709765105
- Stossel, T. P. (1999). Crawling Neutrophil Chasing a Bacterium. Retrieved 3 February, 2015, from [http://php.med.unsw.edu.au/cellbiology/index.php?title=Neutrophil\\_Chemotaxis\\_Movie](http://php.med.unsw.edu.au/cellbiology/index.php?title=Neutrophil_Chemotaxis_Movie)
- Swain, P. S., Elowitz, M. B., & Siggia, E. D. (2002). Intrinsic and extrinsic contributions to stochasticity in gene expression. *Proc Natl Acad Sci U S A*, 99(20), 12795-12800.
- Sze, C. W., Zhang, K., Kariu, T., Pal, U., & Li, C. (2012). *Borrelia burgdorferi* needs chemotaxis to establish infection in mammals and to accomplish its enzootic cycle. *Infect Immun*, 80(7), 2485-2492. doi: 10.1128/IAI.00145-12
- Taylor, J. R., & Stocker, R. (2012). Trade-Offs of Chemotactic Foraging in Turbulent Water. *Science*, 338(6107), 675-679. doi: DOI 10.1126/science.1219417
- Terry, K., Williams, S. M., Connolly, L., & Ottemann, K. M. (2005). Chemotaxis plays multiple roles during *Helicobacter pylori* animal infection. *Infection and Immunity*, 73(2), 803-811. doi: Doi 10.1128/Iai.73.2.803-811.2005
- Thomas, Lewis. (1979). *The medusa and the snail : more notes of a biology watcher*. New York: Viking Press.
- Veening, J. W., Smits, W. K., & Kuipers, O. P. (2008). Bistability, epigenetics, and bet-hedging in bacteria. *Annu Rev Microbiol*, 62, 193-210. doi: 10.1146/annurev.micro.62.081307.163002
- Vladimirov, N., Lebiedz, D., & Sourjik, V. (2010). Predicted Auxiliary Navigation Mechanism of Peritrichously Flagellated Chemotactic Bacteria. *Plos Computational Biology*, 6(3). doi: ARTN e1000717 DOI 10.1371/journal.pcbi.1000717

Vladimirov, N., Lovdok, L., Lebiedz, D., & Sourjik, V. (2008). Dependence of bacterial chemotaxis on gradient shape and adaptation rate. *PLoS Comput Biol*, 4(12), e1000242.

doi: 10.1371/journal.pcbi.1000242

Waite, A. W.\* , Frankel, N. W.\* , Dufour, Y. S.\* , & Emonet, T. (In preparation). Non-genetic diversity results in differential performance in bacterial chemotaxis. \*Equal contribution

Yi, T. M., Huang, Y., Simon, M. I., & Doyle, J. (2000). Robust perfect adaptation in bacterial chemotaxis through integral feedback control. *Proceedings of the National Academy of Sciences of the United States of America*, 97(9), 4649-4653. doi: DOI 10.1073/pnas.97.9.4649





## Part 2: Simulations

### Resolving trade-offs through the genetic control of non-genetic diversity

#### Introduction

In this part, we seek to determine to what extent advantageous diversity can be created from a single biological network, as well as the mechanisms that permit adaptation of this diversity in response to selective pressures. In order to this, we must be able to translate an individual cell's protein concentrations into its fitness in different environments.

Chemotaxis in *E. coli* is a system uniquely well-suited to this purpose because of the wealth of molecular and cellular data that has been gathered by different research groups over the last several decades, making it one of the best-characterized systems in biology for the study of single-cell signal transduction and behavior. We will fit many of these data sets with a single molecular model of *E. coli* chemotaxis that accounts for the interactions of all of the proteins in the network.

From this model, we will be able to calculate phenotypic parameters such as adaptation and tumble bias as a function of protein concentrations. We will then simulate the performance of virtual *E. coli* cells with these phenotypic parameters to characterize any trade-offs that *E. coli* may face in performing fundamental chemotactic tasks. Using different ecological models of selection, we will examine how performance trade-offs give rise to fitness trade-offs. Finally, we will use a model of population diversity based on noisy gene expression to determine whether changing genetic regulation could allow populations to achieve a collective fitness advantage.

## Results

A model to map proteins to phenotype to behavior

The first step in creating a single-cell conversion from protein levels into fitness was to build a model of the chemotaxis network. We began with a standard molecular model of signal transduction based explicitly on biochemical interactions of network proteins. We simultaneously fit the model to multiple datasets measured in clonal wildtype cells by multiple labs (Kollmann, Lovdok, Bartholome, Timmer, & Sourjik, 2005; Park et al., 2010; Shimizu, Tu, & Berg, 2010). Along with previous measurements reported in the literature, this fitting procedure fixed the values of all biochemical parameters (i.e. reaction rates and binding constants), leaving protein concentrations as the only quantities determining cell behavior (Methods, Table 2–1).

The fit took advantage of newer single-cell data not used in previous models that characterize the distribution of tumble bias and adaptation time in a clonal population (Park et al., 2010). In order to fit this data, we coupled the molecular model with a model of noisy gene expression, adapted from Lovdok et al. (2009). In this model of gene expression, the abundance of each protein is approximately lognormal-distributed and depends on a few parameters that determine the mean expression level and the extrinsic (correlated) and intrinsic (uncorrelated) noise in gene expression (Swain, Elowitz, & Siggia, 2002). By combining these components, we were able to use our model to simultaneously fit the mean behavior of the population (Kollmann et al., 2005; Shimizu et al., 2010) and the noisy distribution of single-cell behaviors (Park et al., 2010) (Figure 2–1ABC). In all cases, a single set of fixed biochemical parameters was used, the only driver of behavioral differences between cells being differences in protein abundance generated by the noisy gene expression model. (For more details and discussion, see Methods section “Constant biochemical parameters of the model”)

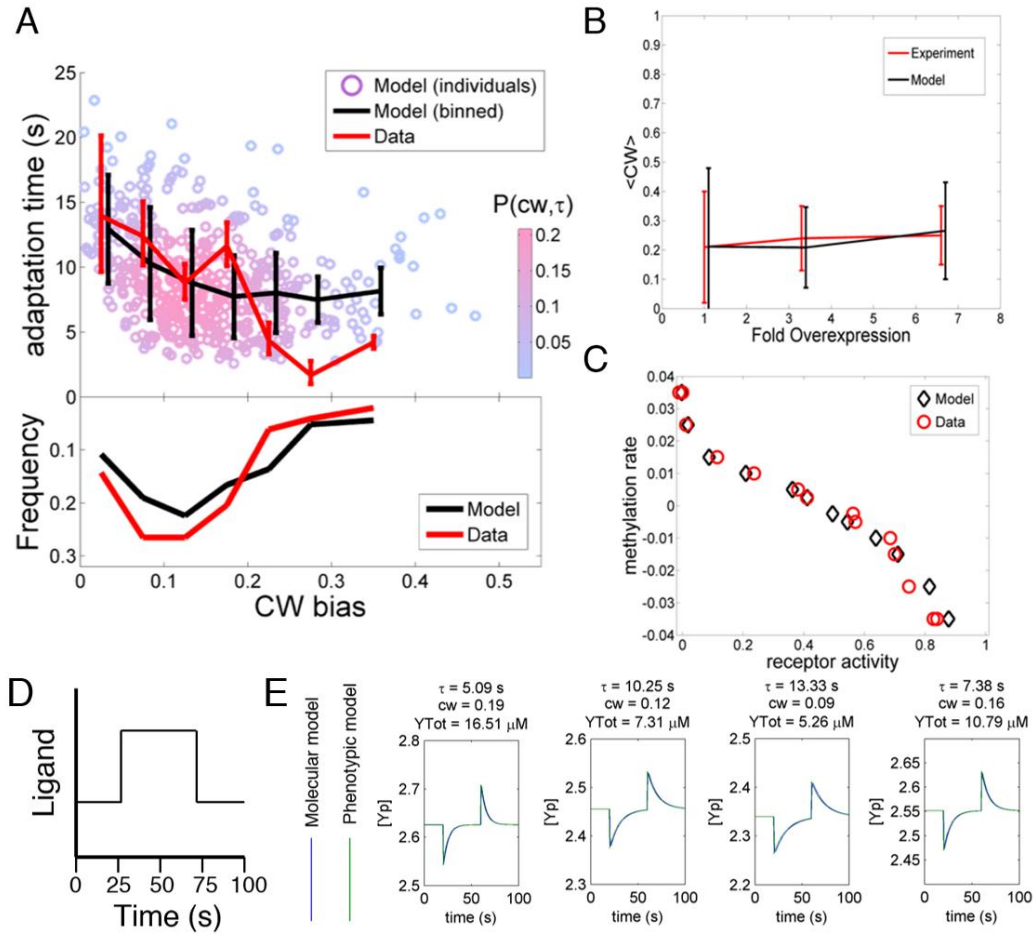


**Figure 2-1. Comparing the model to single cell and population averaged measurements.**

The same set of model parameter values is used for all the plots. **A.** Adaptation time and motor clockwise (CW) bias. Bottom: normalized histogram of motor clockwise bias in the population. Top: The mean and standard deviation of adaptation time in each bin of CW bias. Red lines: experimental data from Park et al. (2010). Black lines: model. Circles: Individual cells from the model. Color: probability density. **B.** Population-averaged CW bias as a function of fold changes in mean expression level of all pathway proteins after Kollmann et al. (2005). Red: data. Black: model. **C.** Population-averaged methylation rate as a function of population-averaged receptor activity obtained by exposing cells to exponential ramps of methyl-aspartate as described in Shimizu et al. (2010). Red circles: data. Black: simulation of model. **A.** Schematic of step function of ligand delivered to immobilized cells in simulation to test response dynamics. **B.** Direct comparison of response of molecular model (blue) and phenotypic model (green), with the same parameters, to stimulus of the form in A illustrating close agreement.

Given an individual with a particular set of protein levels, we then needed to be able to calculate the phenotypic parameters: adaptation time, tumble bias, and CheY-P dynamic range. To do so we solved for the steady state of the model and its linear response to small deviations in stimuli relative to background (Methods). This produced formulae for the phenotypic parameters in terms of protein concentrations. Using these definitions, we reduced the molecular model into a phenotypic model written in terms of phenotypic parameters rather than protein levels (Methods). Simulating the step-response of the molecular model with a given set of protein levels matched the behavior of the phenotypic model with corresponding phenotypic parameters (Figure 2–1DE). Because there are half as many phenotypic parameters as different proteins, the phenotypic model made it computationally possible to explore large ranges of behavior in the simulations we describe in the next section.

Different environments require different behaviors

To characterize chemotactic trade-offs faced by *E. coli*, we began by investigating which chemotactic phenotypes performed best in different ecological tasks. Here, we defined a phenotype as a particular set of values of the phenotypic parameters: adaptation time, tumble bias, and CheY-P dynamic range. We used the phenotypic model to simulate the behavior of individual phenotypes in various environments and measured the performance of each phenotype based on metrics appropriate to each ecological challenge. In total, these steps provided us with a direct mapping from individual protein levels to chemotactic performance in the ecological tasks we describe below.

*E. coli*, like other commensals and pathogens, must survive relatively nutrient-poor environments outside the host until it can colonize a new host. To simulate this scenario, we created two challenges (Detailed discussion in Methods section “Stochastic simulations of the model in ecological challenges”). The first is a foraging challenge in which a spherical parcel of nutrient appears at a certain distance from the cell and immediately begins to diffuse away. This occurs, for instance, upon lysis of a unicellular eukaryote (Blackburn, Fenchel, & Mitchell, 1998). The location of the parcel is unpredictable and could be close or far. For simplicity, each

environment contains only one parcel. Each cell in the simulation accumulated nutrient by collecting an amount proportional to the concentration at its position at every timestep. Performance was defined as the amount of nutrient acquired (Figure 2–2A) within a certain time limit. For computational simplicity we assume that consumption by an individual is small enough not to have an impact on the gradient itself. Feedback of populations onto the shape of the gradient certainly plays a role in many ecological scenarios and could be considered in this framework in the future.

The second environment recapitulates a colonization task, in which a colonization site opens up at a random distance from the cell and immediately starts releasing an attractant signal by diffusion. This case is analogous to the classic capillary experiment (Mesibov & Adler, 1972) and may have relevance to infection by species such as uropathogenic *E. coli* (Lane et al., 2005). We approximated the site as a persistent spherical zone with a non-depleting concentration of attractant. Performance was defined by minimizing the time to reach the site, or maximizing the reciprocal of the arrival time, before some global time limit, which may be determined by the carrying capacity of the site or the periodic purging of the area around the site (Figure 2–2D). Cells unable to reach the colonization site by that time were given an infinite arrival time and consequently a zero performance value. Later, we consider the reduction of this time limit as an ecological factor.

For each ecological task, we scanned different environmental parameters (the distance at which the source appears [Figure 2–3–1,2], the time allotted [Figure 2–3–4], and the source concentration [Figure 2–3–5]) and simulated the performance of different phenotypes. For each phenotype, the performance of 6,000–30,000 replicate trajectories was averaged together. We began with no constraints or correlations between phenotypic parameters and scanned them independently; later we consider the effect of biological constraints on phenotypic distributions.

When a nearby source appeared, cells in the foraging challenge immediately experienced high nutrient levels and were challenged to maintain their position despite having been

stimulated with a large increase in signal. Successful cells had high tumble bias, which curtails long runs, and short adaptation time, which mitigates large responses (Figure 2–2B). Conversely, when a source appeared farther away, cells had to use longer runs to reach the expanding front of the gradient and long adaptation times to integrate the weaker signals at its tails (Figure 2–2C). If time is further limited, this far-source effect is exaggerated (Figure 2–3–3). Consequently, trade-offs become much stronger when the environment turns over rapidly (Figure 2–5).

The case of colonization was similar, except that very high tumble biases were excluded in all cases, since staying in one place was not an option. Additionally, shorter adaptation times were favored overall as compared to foraging. This was because the gradient geometry is much steeper in the vicinity of the source due to its persistently high concentration (Figure 2–2, D inset versus A inset). Climbing steep gradients requires fast adaptation to stay abreast of quickly changing background levels.

The source concentration played a minor role in colonization; however, when foraging less concentrated sources, the favored strategy for far distances flips from low to high tumble bias (Figure 2–3–4). The dynamic range of CheY-P has a negligible effect on cell performance so long as it is sufficiently high as to ensure that the response of CheY-P to kinase activity is linear and does not saturate (Figure 2–3–5). For this reason, when we discuss optimal performance in the subsequent analysis, we assume that the total amount of CheY molecules in the cell has been selected to be high enough to avoid these limitations. (Greater detail on these trends can be found in Methods section “Simulating performance of phenotypes.”)

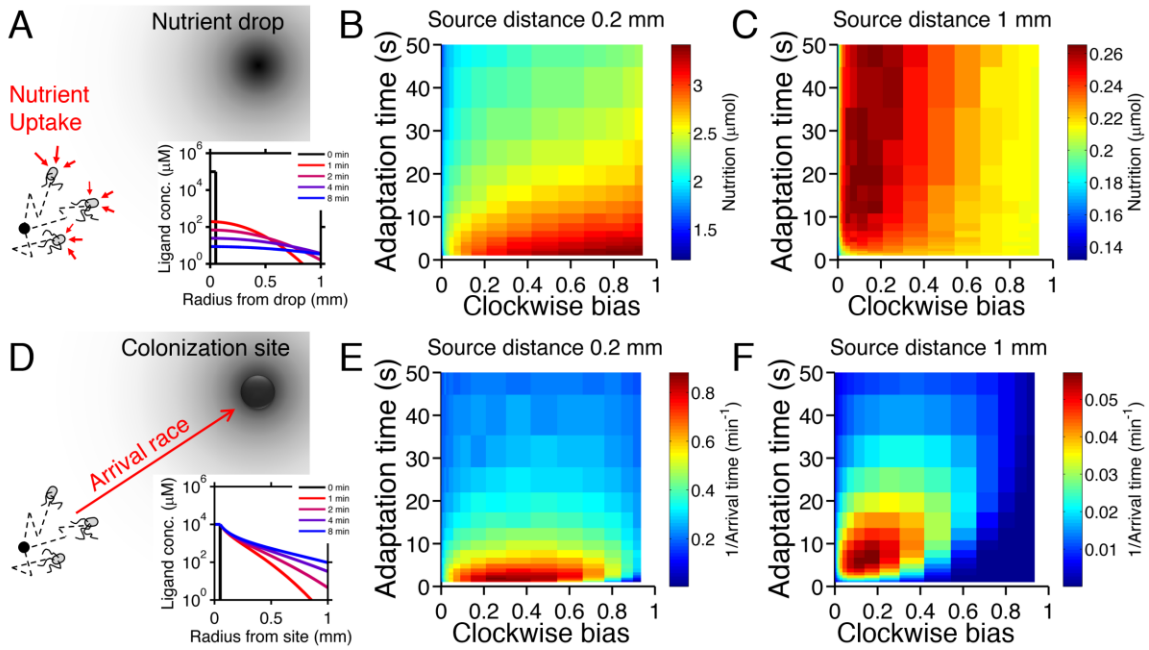


**Figure 2-2. Performance of chemotactic phenotypes depends on environmental conditions.**

**A.** Cartoon diagram (not to scale) of the foraging challenge: cells navigating a 3-D time-varying gradient created by diffusion of a spherical drop of nutrient 100  $\mu\text{m}$  in diameter with diffusion coefficient of 550  $\mu\text{m}^2/\text{s}$ . Inset: radial profile of the attractant concentration over time **B**. Average nutrient collected by each phenotype (combination of tumble bias and adaptation time) in environment in A over 8000 replicates per phenotype. Tumble bias and adaptation time were sample in log-spaced bins. Cells start near to the source (0.2 mm from its center), and are allowed to swim for 13 minutes while accumulating a small fraction of the nutrient they sense. **C**. Same as B except that cells start farther away from the source (1 mm from its center) and 14000 replicates per phenotype were used. **D–F**. Similar to A–C but the environment consists of a colonization challenge: diffusion of ligand out of a spherical non-depleting source representing a colonization site. Rather than nutrient collection, performance (E, F) is quantified as the reciprocal of the arrival time at the source averaged over all replicates (9000 and 36000 for E and F respectively) with a maximum time allotted of 15 minutes.

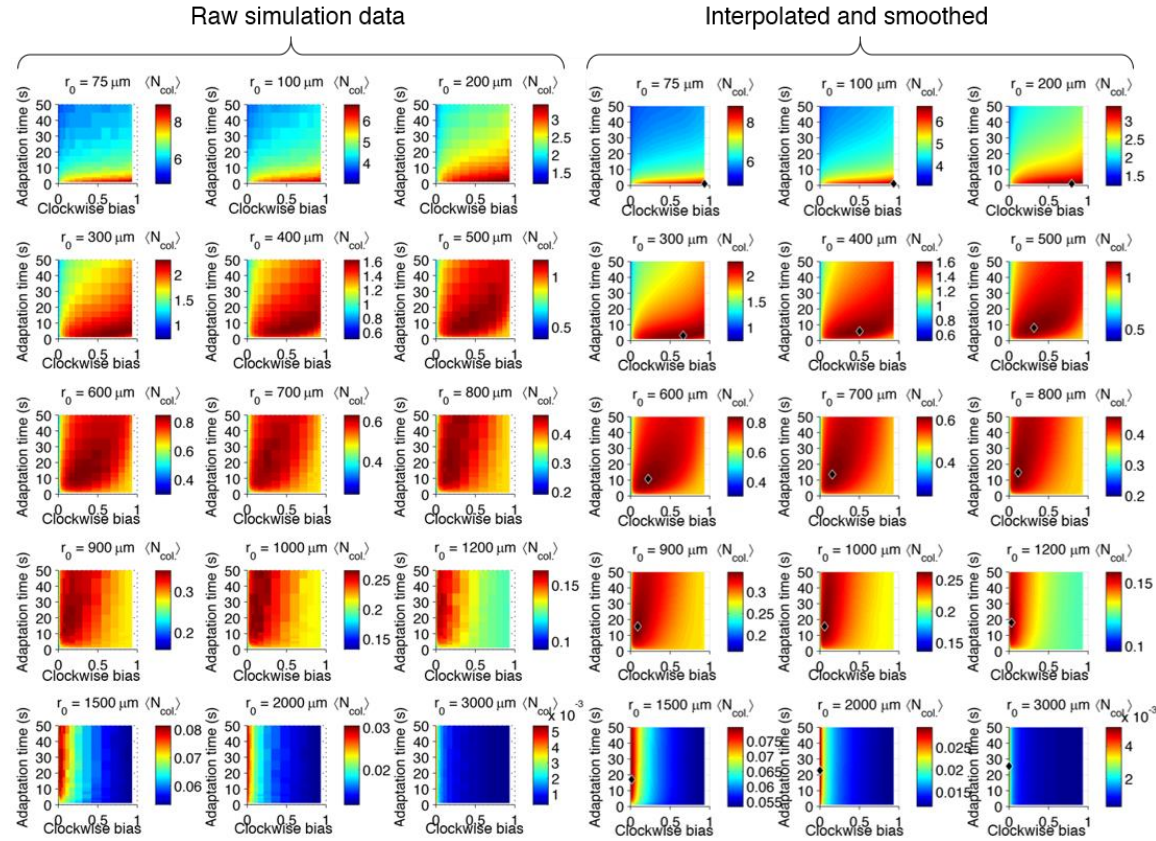


**Figure 2-3-1. Foraging performance as a function of distance to source.**

Left set: Cells with various phenotypes were challenged to forage a source presented at varying distances,  $r_0$  from  $75\mu\text{m}$  to  $3\text{mm}$ . Between 6000 and 30000 replicates were simulated for each phenotype.  $\langle N_{\text{col.}} \rangle$  : the average nutrient collected by all replicates of a given phenotype in  $\mu\text{mol}$ . Right set: Data on left smoothed with a Gaussian filter and resampled on a higher resolution grid of phenotypic parameters. Diamond: phenotype with highest performance.

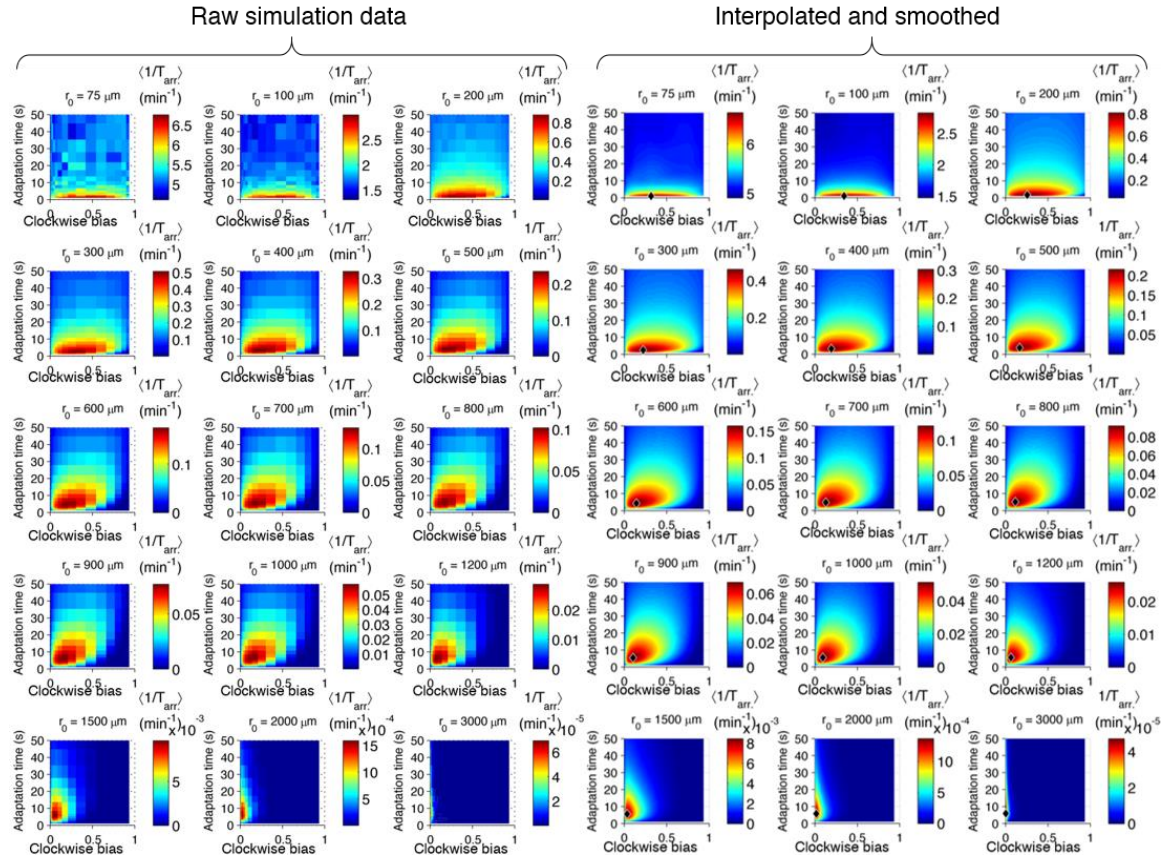


**Figure 2-3-2. Colonization performance as a function of distance to source.**

Left set: Cells with various phenotypes were challenged to colonize a source presented at varying distances,  $r_0$  from 75  $\mu\text{m}$  to 3 mm. Between 6000 and 30000 replicates were simulated for each phenotype,  $\langle 1/T_{arr.} \rangle$ : the average reciprocal-of-arrival-time of all of the replicates of a given phenotype in  $\text{min}^{-1}$ . Right set: Data on left smoothed with a Gaussian filter and resampled on a higher resolution grid of phenotypic parameters. Diamond: phenotype with highest performance.

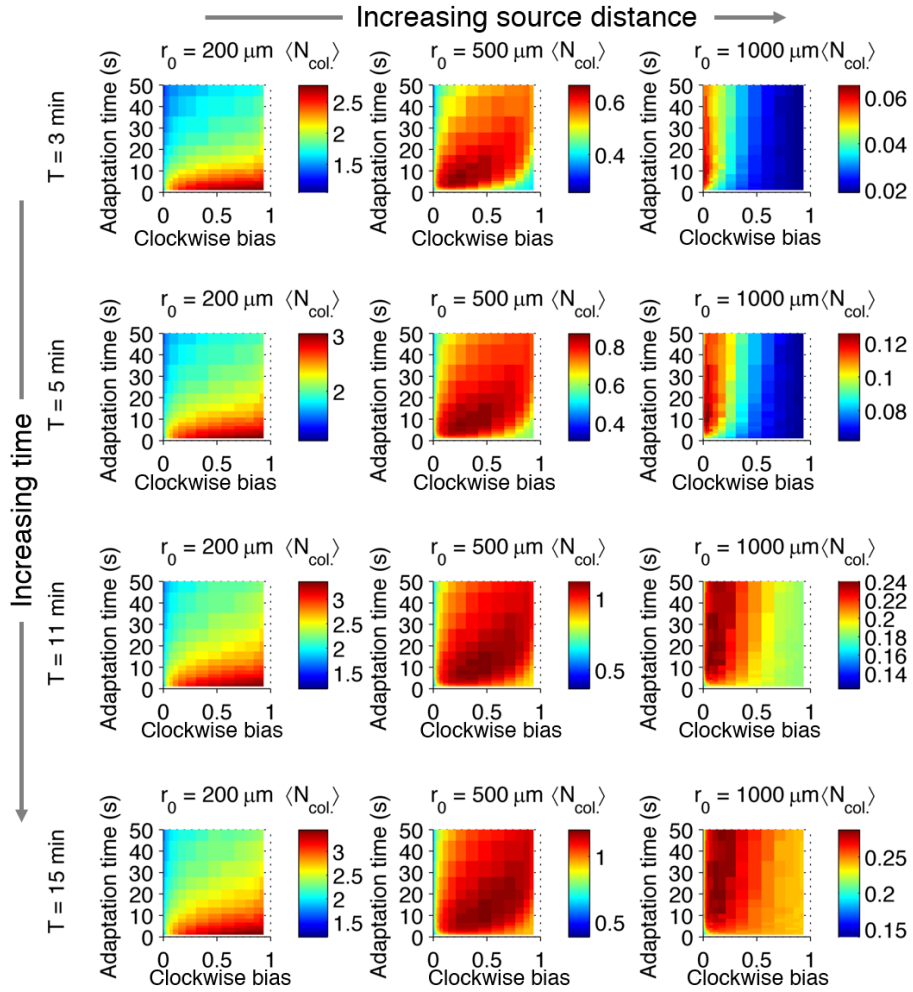


**Figure 2–3–3. Effect of time restrictions on foraging performance.**

Cells were challenged to forage sources that appeared at distances of 200, 5000, or 1000  $\mu\text{m}$  away (columns from left to right). Different amounts of time were allotted to cells to accumulate ligand: 3 min, 5 min, 11 min, 15 min (rows from top to bottom).  $\langle N_{\text{col.}} \rangle$  : the average nutrient collected by replicates of a given phenotype in  $\mu\text{mol}$ .

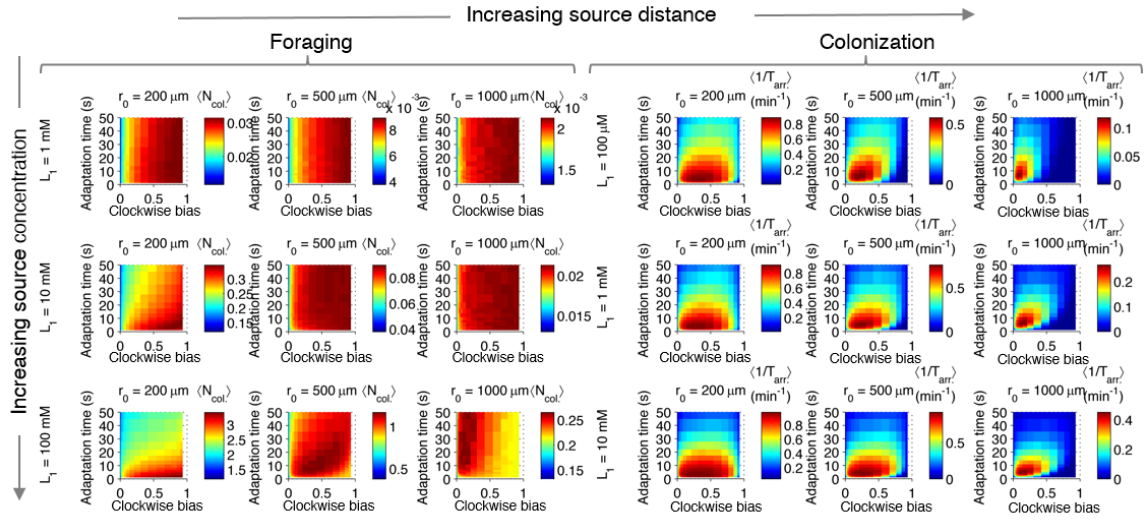


**Figure 2–3–4. Effect of source concentration on performance.**

Left block: foraging performance for increasing source distance (columns) and increasing source concentration (rows):  $L_1 = 1 \text{ mM}$ ,  $10 \text{ mM}$ ,  $100 \text{ mM}$ . Right block: colonization performance for increasing source distance (columns) and increasing source concentration (rows):  $L_1 = 100 \mu\text{M}$ ,  $1 \text{ mM}$ ,  $10 \text{ mM}$ .

In both challenges, the distance at which the source appeared substantially changed which phenotypes outperformed the others. Distant sources required lower tumble bias and longer adaptation time than nearby ones (Figure 2–2, C compared to B and F compared to E). These results are consistent with a recent analytical study (Dufour, Fu, Hernandez-Nunez, & Emonet, 2014) that calculated the velocity of cells climbing static one-dimensional gradients as a function of phenotype. There, trade-off was demonstrated wherein steep gradients required fast adaptation time and high tumble bias for optimal velocity, whereas shallow gradients required slow adaptation time and low tumble bias. Our present simulations in ecological tasks show that a similar trade-off also exists in more complex chemotactic scenarios. Here, simulations of distant sources are similar to simple shallow gradients and nearer sources are analogous to steeper gradients.

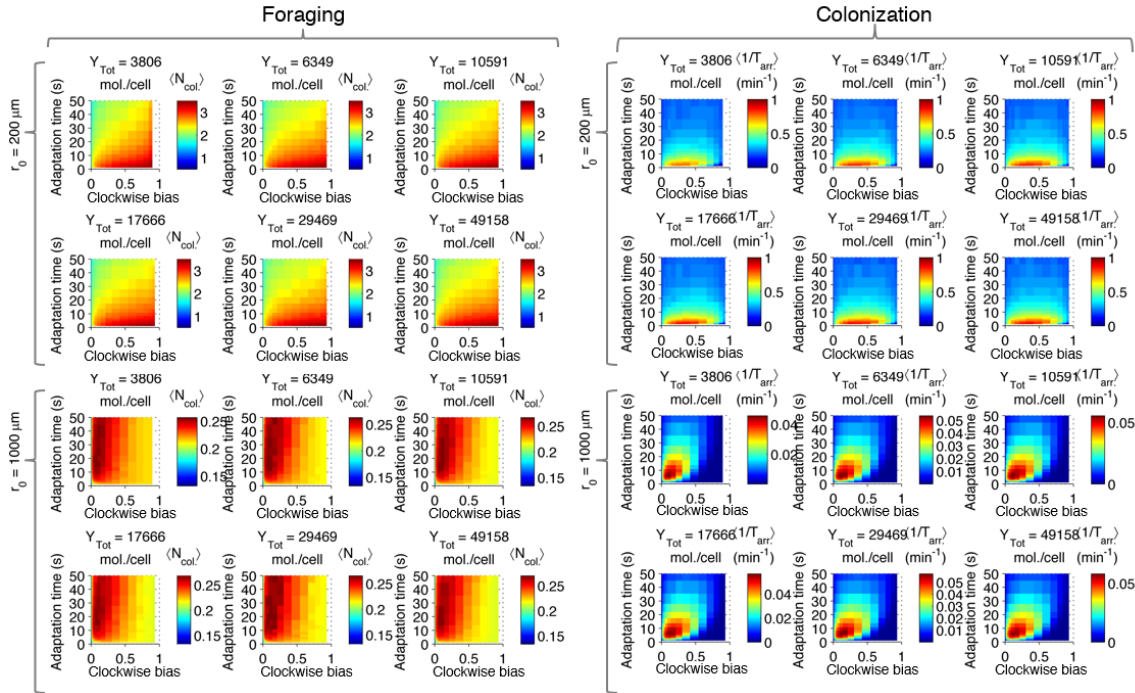


**Figure 2–3–5. Effect of CheY-P dynamic range on performance.**

Left block: foraging performance for near ( $200 \mu\text{m}$ ) and far ( $1000 \mu\text{m}$ ) sources and increasing CheY-P dynamic range, which was changed through the total number of CheY molecules,  $Y_{\text{tot}}$ , as described in the Methods. Right block: same as left block but for colonization.

Trade-off strength and optimal population strategy depend on the nature of selection

Assuming cells have negligible ability to control or predict at what distance the next source will appear, cells are mutually tasked with survival in both near and far sources. We examined trade-offs between pairs of near and far environments to test to the extent to which cells can cope with environmental variability. In each environment, performance was evaluated on a scale relative to the richness of that environment. That is to say, nearby sources naturally result in higher performance values than distant ones. Differences in scale between different tasks do not change the significance of the curvature of the Pareto front; axes can even have different units and the meaning of the curvature will be the same (Shoval et al., 2012)

Trade-offs in performance arose when cells were required to mutually optimize foraging or colonization of nearby and faraway sources (Figure 2–4). This is a consequence of the fact that unique specialists are needed for each environment. As the disparity between these source distances becomes greater, the front of the trade-off transitions from convex to concave (Figure 2–4, from A to C for foraging and from D to F for colonization), demonstrating that performance trade-offs in fundamental tasks can be strong when environmental variability is high.

Nutrition and arrival time, however, are not themselves equivalent to fitness. Fitness defines how these performance metrics would contribute to cellular survival and reproduction. Taking a neutral performance trade-off case for each task type (Figure 2–4, B and E), we asked the questions: how are performance trade-offs translated into fitness trade-offs, and how does the nature of selection influence their strength?

In the case of foraging, survival depends on the ability to scavenge sufficient nutrition. The metabolic reactions that mediate this survival are nonlinear biochemical processes. Many such reactions follow sigmoidal relationships, like the Hill equation, rather than linear ones. We created a simple metabolic relationship in which the survival probability of an individual cell was expressed as a Hill function with two parameters: the amount of food required for survival, and how strongly survival probability depended on that amount (Figure 2–6A). To obtain the fitness of each phenotype, we calculated the expected value of its survival by averaging the survival probability of all replicate cells with that phenotype (Methods section “Calculating fitness from performance”).

When the nutrition requirement was low and the dependency was weak, the previously neutral trade-off became a weak fitness trade-off (Figure 2–6B). Increasing the nutrition requirement and dependency imposed stricter selection, which penalized all but the top performers. This transformed the underlying neutral performance trade-off into a strong fitness trade-off (Figure 2–6C). Therefore, the selection parameters themselves can determine the strength of fitness trade-offs. Discrete transitions between survival outcomes gave qualitatively similar results (Figure 2–7ABC).

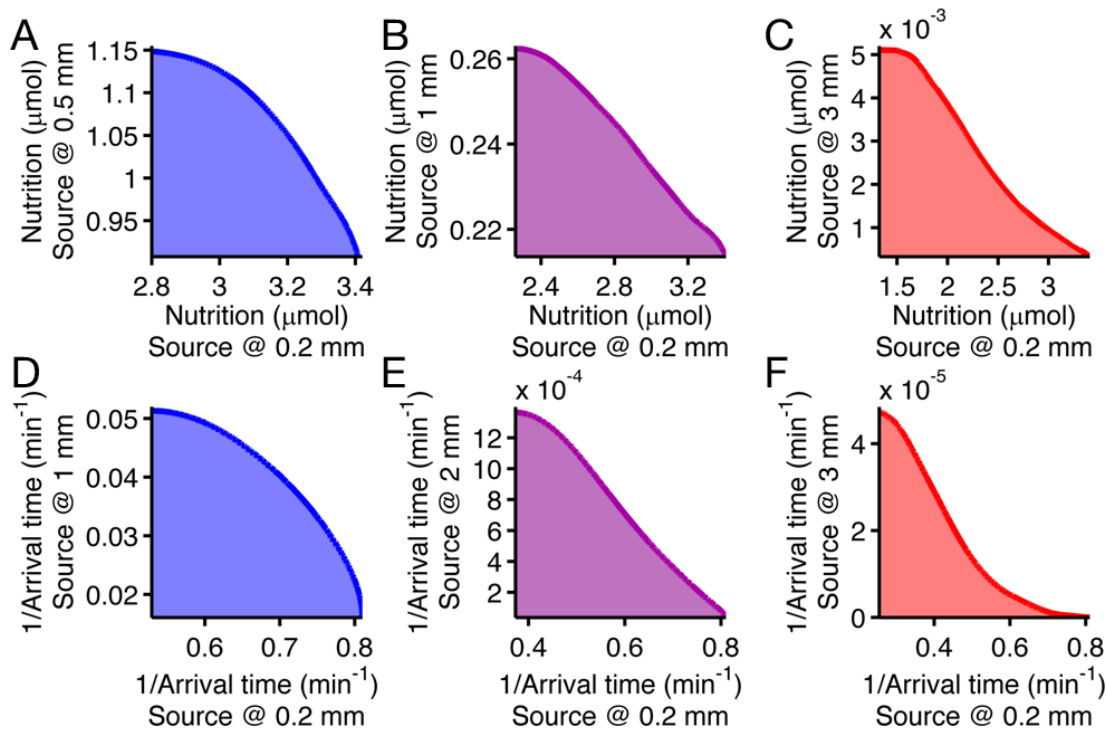


**Figure 2–4. Performance trade-offs in *E. coli* chemotaxis.**

Ecological chemotaxis tasks pose trade-off problems for *E. coli* that become strong when environmental variation is high. **A–C.** Trade-off plot between nutrient accumulation when starting near and when starting far from a source. Plotting the performance of all possible clockwise bias and adaptation time combinations in both near and far cases (colored region) reveals the strength of the trade-off in the curvature of the front. As the disparity between starting distance becomes greater (left to right plots), the trade-off front goes from convex to concave, signifying a transition from weak to strong performance trade-offs. Source distances are indicated on axis labels. **D–F.** Same as A–C but for the colonization challenge.

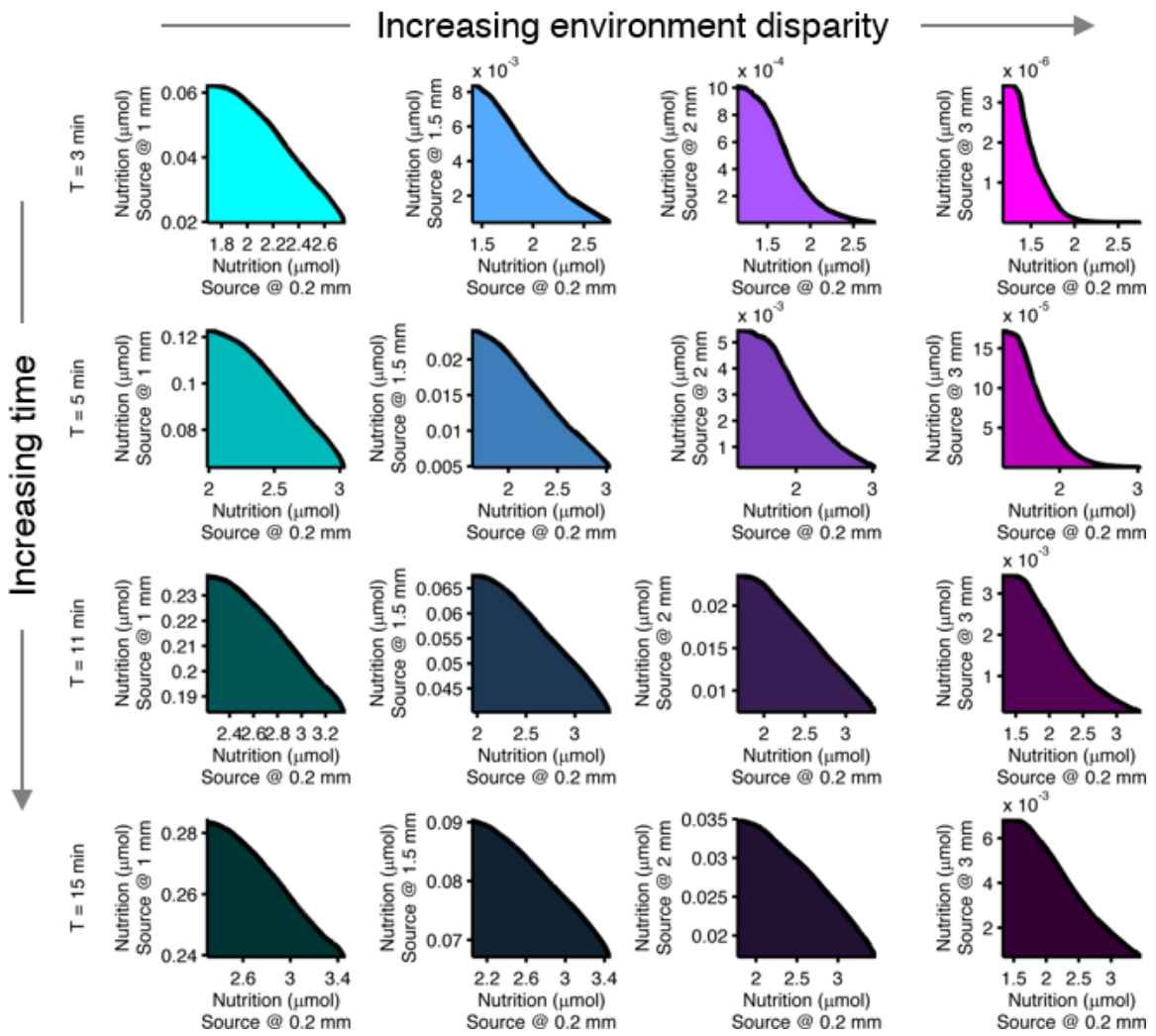


**Figure 2–5. Effect of time limits on near/far foraging trade-offs.**

Trade-offs in performance between foraging near and far sources are shown. From left to right (cyan to magenta), the far case is progressively more distant compared to the near case: 1 mm, 1.5 mm, 2 mm, 3mm. From top to bottom (bright to dark colors), the time allotted is increasing: 3 min, 5 min, 11 min, 15 min. Reduced time allotment makes the front (black line) more concave for the same pair of environments.

In the case of colonization, individual success was binary: either the colonization site was successfully reached, securing that cell's survival for the near future, or the cell was purged from the site – e.g. consumed by a neutrophil – and left no progeny. We approximate the fitness reward for each replicate as a function of the arrival time that steps down from one to zero after a time limit (Figure 2–6D).

As in the foraging case, we calculated the colonization fitness, or survival expectation, of a phenotype as the average of the zero and one outcomes of all the individual replicate cells of that phenotype. When the time limit was high, the previously neutral performance trade-off gave rise to a weak fitness trade-off (Figure 2–6E). When the transition point was lower, the same performance trade-off became a strong fitness trade-off (Figure 2–6F). These effects mirror those demonstrated in the foraging case. As an alternative calculation of fitness we also considered a continuous reward function, which qualitatively produced the same results (Figure 2–7DEF).

The common thread between these cases is that the nonlinear relationship between performance and fitness can increase or reduce the fitness difference between the high-performing specialists and intermediate-performing generalist, strengthening or weakening the trade-off, respectively. Thus, whether diversification is advantageous depends not only on performance trade-offs, but also on the selection process, which has the potential to reverse the strength of trade-offs. Understanding fitness trade-offs therefore requires consideration of both performance and selection. This relationship will receive a detailed treatment in Part 3.

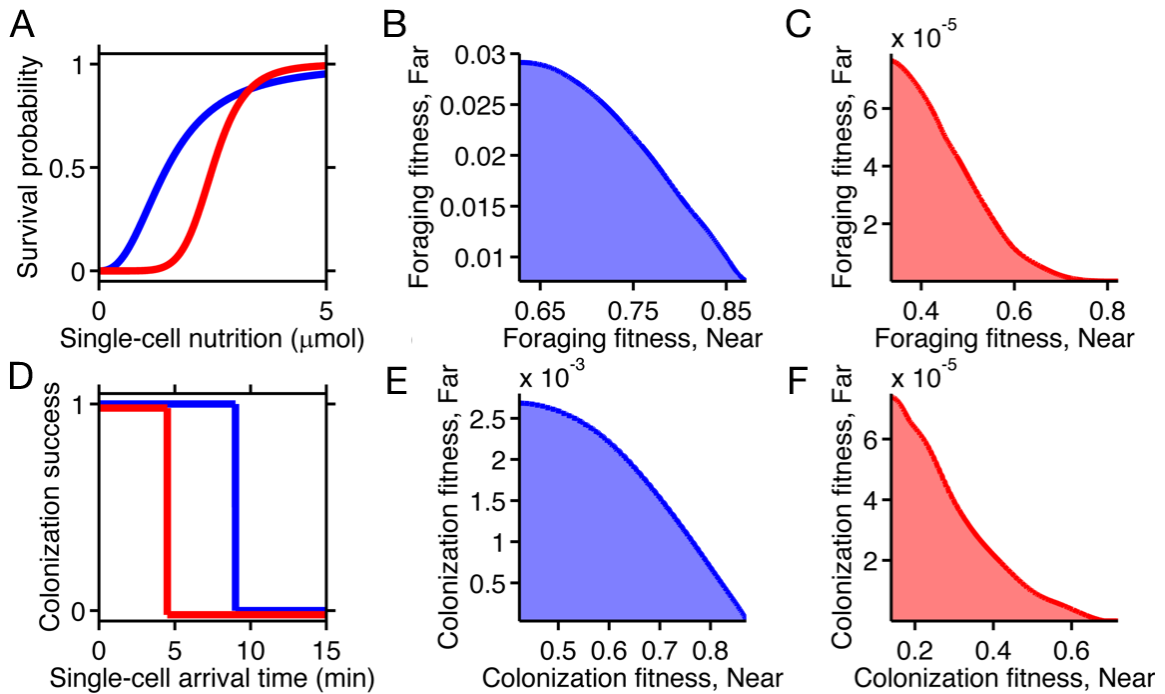


**Figure 2–6. Selection can reshape trade-offs.**

**A.** Simple metabolic model of survival applied to the chemotactic foraging challenge. Each individual replicate is given a survival probability based on a Hill function of the nutrition they achieve from chemotaxis. For each phenotype, the foraging fitness is the average survival probability across replicates. The effect of more (red) and less (blue) stringent survival functions are compared. Transitional nutrition value: 1.5  $\mu\text{mol}$  (blue), 2.5  $\mu\text{mol}$  (red), Hill coefficient: 2.5 (blue), 7 (red). **B–C.** Beginning with the neutral foraging performance trade-off in Figure 2–4B, application of the survival model in A gives rise to either a weak (B) or strong (C) fitness trade-off, depending on where the thresholds and steepness are low (blue curve in A) or high (red curve in A). **D.** Simple threshold model of survival applied to the chemotactic colonization challenge. Each individual replicate survives only if it arrives at the goal within the cut-off time. For each phenotype, the colonization fitness is the probability to colonize measured over all replicates. The effect of more (red) and less (blue) stringent survival functions are compared. Time threshold value: 5 min (blue), 1.5 min (red). **E–F.** Beginning with the neutral colonization trade-off in Figure 2–4E, application of the selection model in C gives rise to either a weak (E) or strong (F) fitness trade-off.

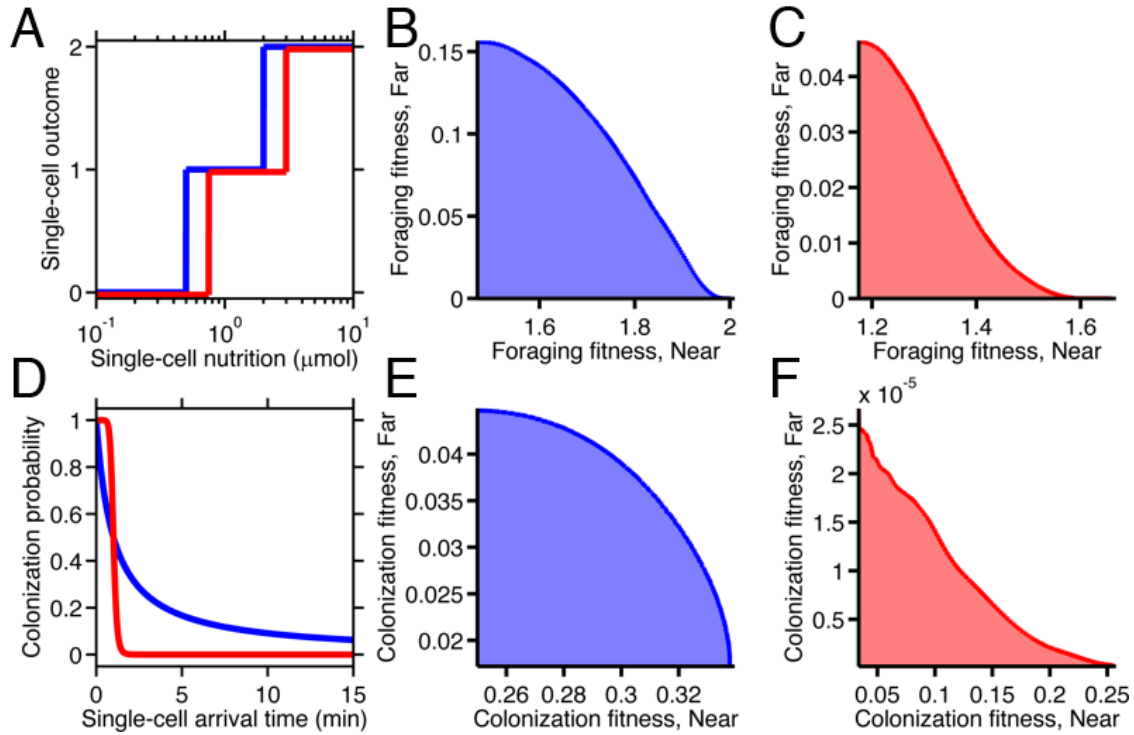


**Figure 2-7. Fitness trade-offs under alternate models of selection.**

**A.** Model of discrete physiological transitions applied to the chemotactic foraging challenge. Each individual replicate is given a number of progeny (0, 1, or 2) based on a two-step function of the nutrition they achieve from chemotaxis. For each phenotype, the foraging fitness is the average progeny across replicates. The effect of more (red) and less (blue) stringent nutrient requirements are compared. Survival requirement: 0.5  $\mu\text{mol}$  (blue), 0.75  $\mu\text{mol}$  (red), Division requirement: 2  $\mu\text{mol}$  (blue), 3  $\mu\text{mol}$  (red).

**B-C.** Beginning with the foraging performance trade-off in Figure 2-4B, application of the survival model in A gives rise to either a weak (B) or strong (C) fitness trade-off, depending on where the thresholds and steepness are low (blue curve in A) or high (red curve in A). **D.** Probabilistic model of survival applied to the chemotactic colonization challenge. Each individual replicate survives has chance to survive depending on how soon it arrives. For each phenotype, the colonization fitness is the probability to colonize measured over all replicates. The effect of more (red) and less (blue) stringent survival functions are compared. Time threshold in both cases is 1 min with dependency 1 (blue) or 10 (red). **E-F.** Beginning with the arrival performance trade-off in Figure 2-4E, application of the selection model in C gives rise to either a weak (E) or strong (F) fitness trade-off.

Genetic control of non-genetic diversity enables populations to resolve trade-offs

We have identified conditions in which diversified populations have a fitness advantage: those in which the environment is highly variable and those in which selection truncates populations to the top performers. While we cannot know precisely what trade-offs wildtype *E. coli* have experienced, we do know that they exhibit substantial phenotypic heterogeneity in their swimming behavior. While there are certainly other sources of variations, our model shows that noise in protein levels is a plausible driver for behavioral diversity in *E. coli* chemotaxis.

We asked the question of whether selection on genetic regulatory features of the chemotaxis network could serve as an adaptive mechanism that can shape diversity in protein abundance, and thus phenotypes, to resolve trade-offs. Such features include the organization of the genes on the chromosome and the sequences of ribosomal binding sites (RBSs) and promoter regions. Selection for individuals with mutations in these features would give rise to adaptation of the distribution without changing highly-conserved network proteins. In our model of gene expression, such alterations were realized through changes in the levels of extrinsic and intrinsic noise and the mean expression level of each protein. We first varied these parameters individually to investigate their effects on phenotypic diversity (Figure 2–8).

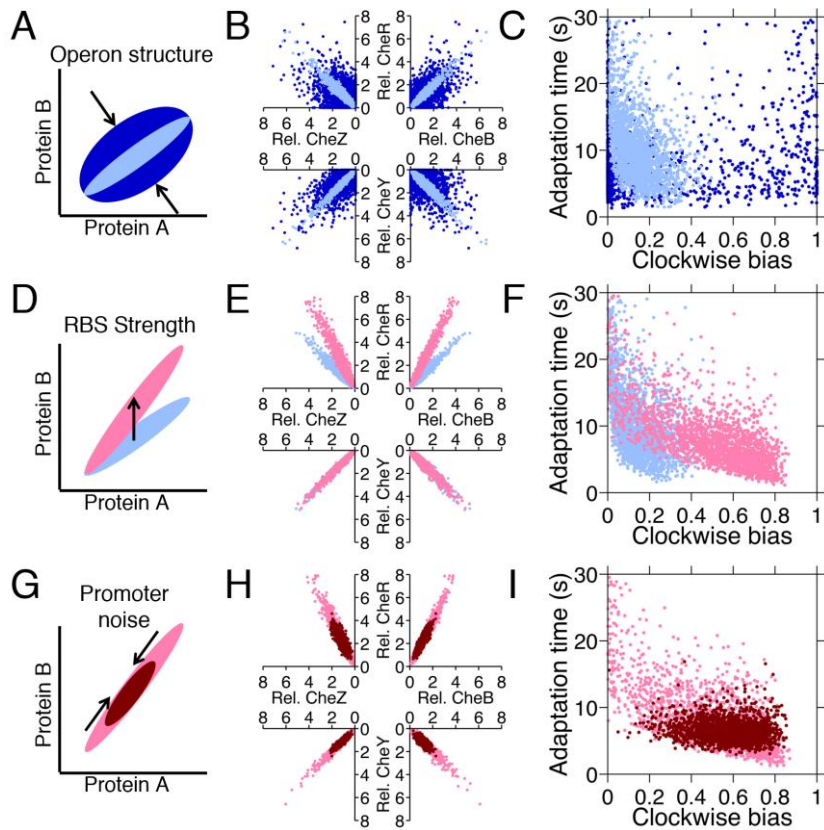


**Figure 2-8. Genetic control of phenotypic diversity.**

**A.** Clustering genes on multicistronic operons constrains the ratios in protein abundance. **B.** Protein expression of core chemotaxis proteins CheRBYZ are shown relative to the mean level in wildtype cells. Two thousand cells are plotted. Light blue: mean levels of the proteins CheRBYZAW and receptors are equal to the mean levels in wildtype cells, which we take to be 140, 240, 8200, 3200, 6700, 6700, 15000 mol./cell, respectively (Li & Hazelbauer, 2004); the extrinsic noise scaling parameter,  $\omega$ , is 0.26 and the intrinsic noise scaling parameter,  $\eta$ , is 0.125, which are both fit to wildtype variability (Figure 2—1). Dark blue: same but with  $\omega = 0.8$ , which is greater than wildtype level. Note the substantial variability around the mean even in the case of wildtype noise levels (light blue). **C.** Clockwise bias and adaptation time of individuals in A. **D.** Changes in the strength of individual RBSs will independently change the mean levels of individual proteins. **E,F.** Light blue: gene expression of cells with same population parameters as in A, light blue. Pink: mean levels of CheR changed to twice wildtype mean. **G.** Promoter sequences can be inherently more or less noisy, resulting in amplification or attenuation of the variability of total protein amounts without affecting protein ratios. **H,I.** Pink: gene expression of cells with same population parameters as in E, pink. Red:  $\omega$  reduced from 0.26 to 0.1.

Intrinsic noise results in diversification of protein ratios (Figure 2–8A). Intrinsic noise can be reduced when multiple genes are expressed from one operon—as are the core chemotaxis genes *cheRBYZ* (Lovdok et al., 2009). When we compared populations that had low or high intrinsic noise (Figure 2–8B, light blue and dark blue, respectively) we observed that high intrinsic noise resulted in many cells having tumble bias near 0 or 1 and therefore being non-chemotactic (Figure 2–8C, dark blue). Reducing intrinsic noise had two effects: more cells had phenotypic parameters within the functional range, and there was an inverse correlation between tumble bias and adaptation time that is known to arise from the architecture of the network (Park et al., 2010; Pontius, Sneddon, & Emonet, 2013) (Figure 2–8C, light blue).

Altering the strength of an RBS changes the mean protein ratios, resulting in a shift in the mean phenotype of the population without directly affecting population variability (Figure 2–8D). Experimentally, mutations in RBSs at the single-nucleotide level are known to have profound effects on expression levels of chemotaxis genes in *E. coli* (Oleksiuk et al., 2011). We tested this by increasing the mean level of CheR (Figure 2–8E, pink). CheR is responsible for receptor methylation, so increasing its mean level decreased the mean adaptation time (Figure 2–8F). There was also an increase in mean tumble bias due to the fact that increasing CheR relative to CheB increases the steady-state methylation level (in spite of the mitigating effect of the CheB-P feedback), leading to higher tumble bias.

Extrinsic noise (Figure 2–8G) arises both from variations in global factors in the cell as well as from the noisiness of promoters that drive multicistronic operons (Bruggeman, Bluthgen, & Westerhoff, 2009; Freed et al., 2008; Miller-Jensen, Skupsky, Shah, Arkin, & Schaffer, 2013). Reduction of extrinsic noise resulted in a population with a tighter, generalist-like distribution of phenotypes (Figure 2–8HIJ, red). Hence, through pathway-specific mutations in the promoter or its regulators, we predict that clonal populations could approach a more generalist-like distribution or a more multi-specialist-like distribution.

To determine whether changing these regulatory parameters alone can generate Pareto-efficient population distributions, we numerically maximized population fitness (Methods),

allowing only the two noise magnitudes and the mean expression levels to vary. Populations are comprised a discrete set of individual cells generated by the noisy gene expression model, each having a fitness in each environment. Following previous studies (Haccou & Iwasa, 1995), the fitness of the population in a given environment was defined as the average fitness of all of its individuals in that environment. For simplicity we assumed that the population encounters environments one at a time and must survive all environments. Therefore the population fitness over all environments was the geometric mean of the population fitness in each environment, weighted by the probability of encountering each environment (Methods). The environments considered were the same as in Figure 2–6, which include examples of both strong and weak fitness trade-offs for each ecological task.

We first performed the optimization with lower limits on the noise parameters that were very low (Methods). When we optimized populations for weak trade-off in either foraging or colonization tasks, the resulting populations in both tasks exhibited low levels of protein noise (Figure 2–9A for foraging and 2–9E for colonization, blue points) and low phenotypic variability (Figure 2–9B and F). In contrast, populations optimized for the strong foraging or colonization trade-offs exhibited higher protein noise (Figure 2–9A and E, red compared to blue points) and higher phenotypic variability (Figure 2–9B and F). In all cases, the spread of individuals in the optimal populations was constrained to the Pareto front (Figure 2–9CDGH). The spread was more condensed in the weak trade-offs than in the strong trade-off in the same task (Figure 2–9C compared to D for foraging and G compared to H for colonization). Interestingly, the driver of diversity in the case of the foraging trade-off was extrinsic noise whereas in the colonization case it was intrinsic (Figure 2–9A compared E, red points). This resulted in a negative correlation between tumble bias and adaptation time in the foraging case, but no such correlation in the colonization case (Figure 2–9B compared to F, red points).

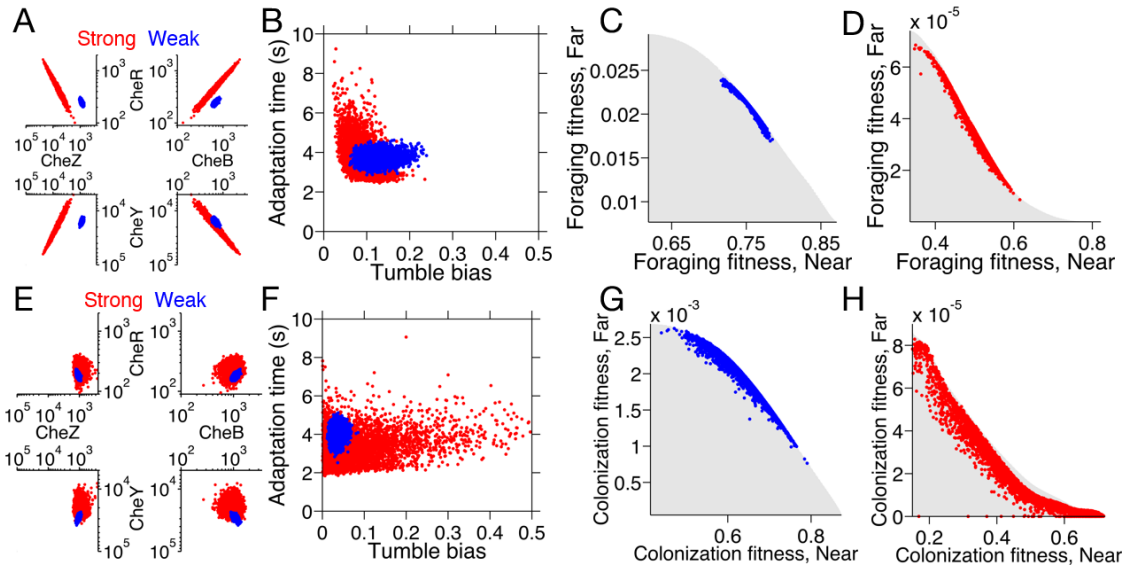


**Figure 2–9. Optimized gene expression noise under trade-offs, very low noise permitted**

Protein expression of populations were optimized for either weak or strong foraging fitness trade-offs (same trade-offs as in Figure 2–6B and C). For each population, 5000 individuals are plotted, protein expression shown relative to the mean level in wildtype cells. **A.** Gene expression parameters of the population optimized for the weak foraging trade-off: mean expression levels of CheRBYZAW and receptors relative to mean wildtype expression level were 1.79, 2.925, 1.98, 1.08, 1.08, 1.08, and 1.08 fold, respectively, with an intrinsic noise scaling parameter,  $\eta$ , of 0.04 and an extrinsic noise scaling parameter,  $\omega$ , of noise 0.02. For the strong foraging trade-off: mean CheRBYZAW and receptors relative to wildtype were 4, 3.35, 2.75, 10, 10, 10, and 10 fold, respectively, with  $\eta = 0.04$  and  $\omega = 0.15$ . **B.** Clockwise bias and adaptation time of individuals in A with the corresponding dot color. **C.** Fitness of the population that was optimized for the weak foraging trade-off (corresponding to blue dots in A and B). **D.** Same as C but for the population optimized for the strong foraging trade-off. **E–H.** Same as A–D for the colonization fitness trade-offs shown in Figure 2–6D and E. Population parameters optimized for weak colonization trade-off: mean CheRBYZAW and receptors levels relative to wildtype were 4.58, 3.61, 1.32, 1.32, 1.32, and 1.32 fold, respectively, with  $\eta = 0.04$  and  $\omega = 0.02$ . Population parameters optimized for strong colonization trade-off: mean CheRBYZAW and receptors levels were 1.72, 4.17, 2.44, 1.21, 1.21, 1.21, and 1.21 fold, respectively, with  $\eta = 0.18$  and  $\omega = 0.02$ .

We then established a lower limit on the noise parameters that was higher, which reflects an irreducibility of biological noise. We used the wildtype level of intrinsic noise obtained in our fit to experimental data (Figure 2–1) as a lower bound in the optimization, with the rationale that multiple experimental studies show that wildtype cells have reduced intrinsic noise for improved chemotactic function (Kollmann et al., 2005; Lovdok et al., 2009; Lovdok, Kollmann, & Sourjik, 2007), from which we inferred that they may be operating near a fundamental lower limit. We also set a lower bound on the total noise level based on experimental measurements in *E. coli* of protein abundance in individual cells over a large range of proteins (Taniguchi et al., 2010) (Methods). This bound is primarily from irreducible extrinsic noise arising from various mechanisms such as the unavoidability unequal partitioning of proteins during cell division. We set an upper bound on mean protein levels to 5 fold above the wildtype mean in order to be within a range of experimentally established observations (Kollmann et al., 2005; Li & Hazelbauer, 2004) (Methods).

Similar to above, when we optimized populations for weak trade-off in either foraging or colonization tasks, the resulting populations in both tasks exhibited lower levels of protein noise (Figure 2–10A for foraging and E for colonization, blue points) and lower phenotypic variability (Figure 2–10B and F), in comparison to populations optimized for the respective strong foraging or colonization trade-offs (Figure 2–10ABEF, red compared to blue points), although the difference was smaller than in the case of looser constraints on gene expression parameters (i.e. Figure 2–9). The spread of individuals was again constrained to the Pareto front (Figure 2–10CDGH). The spread was more slightly condensed in the weak trade-offs than in the strong trade-off in the same task (Figure 2–10C compared to D for foraging and G compared to H for colonization)

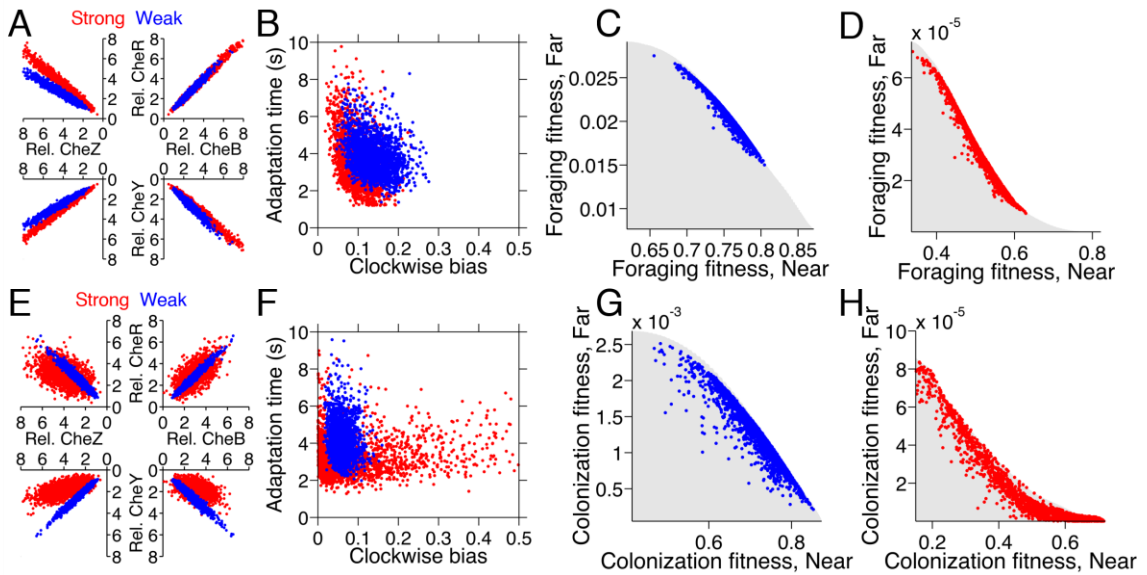


**Figure 2–10. Optimized gene expression noise under trade-offs with biological noise limits**

Protein expression of populations were optimized for either weak or strong foraging fitness trade-offs (same trade-offs as in Figure 2–6B and C). For each population, 2000 individuals are plotted, protein expression shown relative to the mean level in wildtype cells. **A.** Gene expression parameters of the population optimized for the weak foraging trade-off: mean expression levels of CheRBYZAW and receptors relative to mean wildtype expression level were 2.54, 2.53, 2.50, 4.20, 4.50, 3.49, and 3.49 fold, respectively, with an intrinsic noise scaling parameter,  $\eta$ , of 0.051 and an extrinsic noise scaling parameter,  $\omega$ , of noise 0.128. For the strong foraging trade-off: mean CheRBYZAW and receptors relative to wildtype were 3.27, 3.27, 2.86, 3.83, 4.17, 2.82, and 5.00 fold, respectively, with  $\eta = 0.051$  and  $\omega = 0.200$ . **B.** Clockwise bias and adaptation time of individuals in A with the corresponding dot color. **C.** Fitness of the population that was optimized for the weak foraging trade-off (corresponding to blue dots in A and B). **D.** Same as C but for the population optimized for the strong foraging trade-off. **E–H.** Same as A–D for the colonization fitness trade-offs shown in Figure 2–6D and E. Population parameters optimized for weak colonization trade-off: mean CheRBYZAW and receptors levels relative to wildtype were 2.42, 2.52, 2.32, 2.50, 4.16, 3.25, and 5.00 fold, respectively, with  $\eta = 0.055$  and  $\omega = 0.126$ . Population parameters optimized for strong colonization trade-off: mean CheRBYZAW and receptors levels were 2.90, 2.92, 1.71, 3.845, 2.25, 3.80, and 3.76 fold, respectively, with  $\eta = 0.221$  and  $\omega = 0.090$ .

In the weak trade-off cases, condensation into a single point on the Pareto front was impeded by lower bounds on noise. Even though a pure generalist strategy was unattainable, adjustments in the means and correlations between protein abundance enabled the system to shape the “residual” noise to distribute cells along the Pareto front. This could be a general phenomenon in biological systems: given that molecular noise is irreducible, the best solution is to constrain diversity to the Pareto front. Our results suggest this may be achievable via mutations in the regulatory elements of a pathway.

In the strong foraging trade-off, the optimized population took advantage of the fact that correlated noise in protein levels leads to an inverse relationship between clockwise bias and adaptation time (Figure 2–9 and 2–10, A and B, red) due to the architecture of the network. By capitalizing on this feature, the population contained specialists for near sources, which had higher clockwise bias and shorter adaptation times, and those for far sources, which had lower clockwise bias and longer adaptation time. Cells with clockwise bias above 0.25 were avoided because steep gradients were very short-lived in this challenge.

The strong colonization trade-off also required high clockwise bias for near sources and low clockwise bias for far sources. However, since the gradient in the site’s vicinity did not flatten, a short adaptation time was always necessary to climb the final part of the gradient and clockwise bias above 0.25 could become advantageous when the source is close. In order to achieve greater diversity in clockwise bias while keeping adaptation time low, the optimized population for this trade-off had increased intrinsic noise, which diversified protein ratios and disrupted the inverse correlation between clockwise bias and adaptation time (Figure 2–9 and 2–10, E and F, red).

In all cases, selection on regulatory elements of the network resulted in phenotypic diversity being remarkably constrained to the Pareto front. Furthermore, the levels of diversity in these populations are consistent with the sign of the curvature of the Pareto front they occupy. The adaptability of these distributions predicts that genetic alterations to basic regulatory mechanisms may allow clonal cells to resolve multi-objective problems at the

population level using a single signaling network. This mechanism could allow populations to cope with the need to navigate diverse environments, or follow diverse signals, without partitioning into discrete subpopulations through the use of switches or modules.

Potential future experiments suggested by the theory

Our results could be tested using several types of chemotactic performance experiments. The radial symmetry of our environments makes it possible to use the capillary (Park, Guet, Emonet, & Cluzel, 2011) and plug assays (Lanfranconi, Alvarez, & Studdert, 2003), which present cells with a concentrated source of attractant. The soft agar swarm plate assay (Lovdok et al., 2007) could be used as well if modified to introduce nutrient solution to one spot of the plate instead of the whole. Microfluidic chemotaxis assays (Kalinin, Neumann, Sourjik, & Wu, 2010) could be constructed using soft lithography to reproduce these environments with a higher level of precision. In each of these cases, the distance between cells and the source and the duration for which the source is presented could be varied, as well as the source concentration. Cells with high performance should be selected, analyzed for their phenotypes and protein abundance, and re-grown, either under continual presentation of the same condition or switching between two or more conditions.

Using these types of experiments, our theoretical results predict several specific outcomes. First, seeding the same clonal population in different assays that have different length- or time-scales should select for different optimal subpopulations with different phenotypic parameters and different levels of protein expression. Such measurements would make it experimentally possible to verify the chemotactic trade-offs we predict. Experimental work using the capillary assay already supports this claim (Park et al., 2011), which will be further investigated in Part 3 of this dissertation.

In the case of laboratory evolution with one selection condition, we predict an eventual shift toward genotypes that suppress population noise, as well as toward mutations in chemotaxis protein RBSs that allow the mean clockwise bias and adaptation time to specialize for this task. In this case, we predict that populations will reduce phenotypic diversity but run into a

lower limit of protein noise. These outcomes could be measured by performing single cell phenotype analyses and by re-sequencing the operon. Conversely, alternating selection in different assays or different length- and time-scales may lead to enhanced phenotypic noise and still other RBS mutations. In these cases, whole genome re-sequencing may show alterations to the operon structure or to the master regulators of chemotaxis.

Strains that are evolved in the lab could be compared to the wildtype ancestor in order to gain insight into the types of environments the latter evolved in. Furthermore, investigating phenotypic diversity in wild strains in comparison to domesticated and evolved laboratory strains may uncover differences that reflect the level of environmental diversity faced in their respective lifestyles.

## Discussion

Without changing the protein coding sequences or interrupting robust features such as perfect adaptation, the bacterial chemotaxis system exhibits significant plasticity in the shape of phenotypic distributions. Such plasticity can provide fitness advantages under chemotactic trade-offs. While we do not know what trade-offs wildtype *E. coli* populations have faced, our results suggest that the relationship between chemotactic phenotype and survival is highly sensitive to environmental time- and length-scales. Hence, we expect that the real-world ecology of chemotaxis will impose many trade-offs. Indeed, the same network in *E. coli* is tasked with processing chemical, oxidative, and temperature information on multiple scales simultaneously. Additionally, changes in the environment bring different growth conditions, which change the distribution of protein expression (Li & Hazelbauer, 2004; Scott, Gunderson, Mateescu, Zhang, & Hwa, 2010) and will naturally change the distribution of phenotypes as well. As new data on these niches and populations emerge, the framework we introduce in this dissertation could be used to investigate the significance of these trade-offs and their resulting phenotypic distributions.

A new feature of our conceptual framework is the distinction between performance and fitness. Organisms exhibit many behaviors which, to researchers, are not directly connected to survival and reproduction. These gaps in our understanding inhibit our abilities to understand the evolutionary significance of many organismal behaviors. Here, we demonstrated methods for broaching these questions quantitatively, and in so doing uncovered the relevant finding that nonlinearities in selection can strengthen or weaken trade-offs. This will be of general interest to those studying fitness trade-offs since the nature of selection can change the optimality of pure versus mixed population strategies.

In this study, we simplified the problem by focusing only on pairs of environments, but trade-off problems between more than two environments are certainly possible. Without modifying this framework, trade-offs between any arbitrary distribution of environments could be examined. Likewise, multiple different task types could be compared simultaneously. Due to the fact that such cases will impose more constraints on the chemotaxis system, stronger and more difficult problems are likely to arise. Other simplifications were that challenges and regrowth occurred in discrete sequential steps and that there was no direct inheritance or persistence of phenotype from mother to daughter cells. The relative importance of these features will depend on the relationship between their time-scales and those of the environmental challenges (Kussell & Leibler, 2005).

## Methods

### Single-cell model of chemotaxis with population-level model of gene expression

#### Flagellar motors

Bacterial flagellar motors switch between counterclockwise rotation, associated with relatively straight swimming, and clockwise rotation, associated with periods of tumbling. We model the bacterial flagellar motor as a bistable stochastically switching system (Sneddon, Pontius, & Emonet, 2012; Tu & Grinstein, 2005). The free energies of the states, and consequently the switching rates between states, are modulated by the concentration of

phosphorylated messenger protein CheY,  $Y_p$ . We assume that the free energy difference between the CCW and CW states is linear in the occupancy of the motor protein FliM by CheY-P. The rates  $k_+$  and  $k_-$  of switching out of the CW and CCW states, respectively, are then given by

$$k_{\pm} = \omega_0 e^{\pm \frac{G}{2} \left( \frac{1}{2} - \frac{Y_p}{Y_p + K_d} \right)}, \quad (2-1)$$

in which  $\omega_0$  sets the maximum rate of motor switching,  $G$  sets the scale of the free energy difference, and  $K_d$  is the FliM-CheY-P dissociation constant. Instantaneous CW bias  $CW$  as a function of CheY-P input is given by

$$CW = \frac{k_-}{k_+ + k_-}, \quad (2-2)$$

which describes a sigmoidal curve (Cluzel, Surette, & Leibler, 2000). Here  $g$  determines the steepness of the relationship, and  $K_d$  sets the location of the midpoint. The noise in the  $Y_p$  signal is modeled using a normal distribution  $N(Y_p)$  with mean  $Y_{p,0}$  and variance,  $\sigma_{Y_p}^2$ , the time-averaged CW bias  $CW_0$  is obtained by averaging the instantaneous CW bias according to

$$CW_0 = \int_{-\infty}^{\infty} CW(Y_p) N(Y_p) dY_p. \quad (2-3)$$

In our model, we make the simplifying assumption that each cell has one flagellum; therefore, the clockwise bias is equivalent to the tumble bias (Sneddon et al., 2012), or  $CW = TB$ . When the system is either unstimulated or fully adapted to a constant background, the system is said to be at steady state. In such conditions,  $Y_p = Y_{p,SS}$ ,  $CW_0 = CW_{SS} = TB_0 = TB_{SS}$ . The “tumble bias” we refer to in the main text is  $TB_{SS}$  and is set by  $Y_{p,SS}$  through Eq. (2-3), along with  $\sigma_{Y_p}^2$ , which is calculated below under “Linearization of the chemotaxis pathway model.” We show how  $Y_{p,SS}$  is calculated below under “Molecular model of the chemotaxis pathway.”

### Bacterial chemoreceptors

Bacteria sense changes in their external environment using transmembrane chemoreceptors. These receptors are sensitive to changes in the concentrations of various chemical stimuli as well as temperature, oxygen levels, and acidity. Receptors respond to stimuli by modulating their rates of switching between active and inactive conformations. Here we model the receptor response to the chemoattractant methyl-aspartate using a Monod-Wyman-Changeux model of mixed complexes of Tar and Tsr receptor types (Endres & Wingreen, 2006; Mello & Tu, 2005). Each MWC complex consists of  $N_{Tsr} = 4$  Tar and  $N_{Tar} = 2$  Tsr homodimers (Endres & Wingreen, 2006). Receptors within each complex are assumed to switch in an all-or-none fashion. The free energy of the active conformation is taken to decrease linearly with the methylation level  $m_c$  of the complex, as determined experimentally (Shimizu et al., 2010). For this model, the mean activity  $a$  of the complex as a function of  $m_c$  and the external methyl-aspartate stimulus  $L$  is

$$a(m_c, L) = \left(1 + e^{\varepsilon_0 + \varepsilon_1 m_c} f(L)\right)^{-1}, \quad (2-4)$$

in which  $\varepsilon_0$  and  $\varepsilon_1$  are constants, and the function

$$f(L) = \left( \frac{1 + L / K_{Tar}^{off}}{1 + L / K_{Tar}^{on}} \right)^{N_{Tar}} \left( \frac{1 + L / K_{Tsr}^{off}}{1 + L / K_{Tsr}^{on}} \right)^{N_{Tsr}}. \quad (2-5)$$

The constants  $K_{Tar}^{off}$ ,  $K_{Tar}^{on}$ ,  $K_{Tsr}^{off}$ , and  $K_{Tsr}^{on}$  characterize the binding of methyl-aspartate to Tar and Tsr in active and inactive conformations. In the models of the chemotaxis pathway below we use  $m$  to denote the mean methylation level of all MWC complexes in the cell and take  $a(m)$  to be the mean activity of all complexes in the cell, following previous studies (Emonet & Cluzel, 2008; Mello & Tu, 2005; Shimizu et al., 2010; Sneddon et al., 2012). This approximation is equivalent to assuming that the distribution of  $m_c$  across the cell is sharply peaked around  $m$  or, alternatively, that  $a(m_c)$  is linear in  $m_c$ .

## Molecular model of chemotaxis

Receptor activity adapts to persistent stimulus through methylation and demethylation of the receptors by the enzymes CheR and CheB, respectively. In modeling the kinetics of receptor modification, we follow previous work that successfully describes the adaptive response measured in populations in bacteria (Pontius et al., 2013; Shimizu et al., 2010). In this model, CheR binds preferentially to inactive receptors and CheB to active receptors. The average methylation level  $m$  of all MWC complexes therefore evolves according to

$$\frac{dm}{dt} = \frac{2N}{T_{Tot}} \left( \frac{k_r R_{Tot} T}{K_r + T} - \frac{k_b B_{p,Tot} T^*}{K_b + T^*} \right) + \eta_m(t), \quad (2-6)$$

in which  $T_{Tot}$ ,  $R_{Tot}$ , and  $B_{p,Tot}$  are the total concentrations of receptors, CheR, and phosphorylated CheB in the cell,  $K_r$  and  $K_b$  are Michaelis-Menten constants characterizing the enzyme-receptor binding, and  $k_r$  and  $k_b$  are the catalytic rates for receptor methylation and demethylation.  $T^*$  and  $T$  denote the concentrations of free active and inactive receptors, respectively. Since the number of enzyme-receptor complexes is small relative to the number of receptors, we make the approximations  $T^* + T \sim T_{Tot}$  and for the mean activity of the system,  $a \sim T^*/T_{Tot}$ . We define  $N = N_{Tar} + N_{Ts}$  as the size of the MWC complexes, so  $T_{Tot}/2N$  is the total concentration of MWC complexes in the cell. The term  $\eta_m(t)$  is a white noise source that introduces spontaneous fluctuations in methylation level. While models of the form of Eq. (2–6) correctly describe the adaptation dynamics of averaged populations, they generally fail to predict sufficiently high levels of noise(Pontius et al., 2013). Therefore, we set the intensity of the noise source  $\eta_m(t)$  to agree with experimental measurements, as discussed in the next section. Differentiating  $a(m, L)$  and using  $\partial a / \partial m = \varepsilon_1 a(1-a)$ , we may recast Eq. (2–6) to describe the evolution of the mean activity  $a$  of the system:

$$\frac{da}{dt} = \varepsilon_1 a(1-a) \frac{2N}{T_{Tot}} \left( \frac{k_r R_{Tot}(1-a)}{K_r / T_{Tot} + 1-a} - \frac{k_b B_{Tot} a}{K_b / T_{Tot} + a} \right) + \frac{\partial a}{\partial L} \dot{L} + \varepsilon_1 a(1-a) \eta_m(t) \quad (2-7)$$

Note that the stimulus term depends on the time derivative of the ligand concentration  $\dot{L}$ . At

steady state the steady state activity  $a_0$  is given by  $\frac{k_r R_{Tot} (1-a_0)}{K_r / T_{Tot} + 1 - a_0} = \frac{k_b B_{p,Tot} a_0}{K_b / T_{Tot} + a_0}$ .

In their active form, receptors promote the autophosphorylation of an associated histidine kinase CheA, which in turn phosphorylates CheB and the messenger protein CheY that regulates the activity of the flagellar motors. The concentration  $A_p$  of phosphorylated CheA is then described by

$$\frac{dA_p}{dt} = a_p (A_{Tot} - A_p) a - a_b A_p (B_{Tot} - B_{p,Tot}) - a_y A_p (Y_{Tot} - Y_p), \quad (2-8)$$

in which  $a_p$ ,  $a_b$ , and  $a_y$  are rate constants,  $A_{Tot}$ ,  $B_{Tot}$ , and  $Y_{Tot}$  are the total concentrations of CheA, CheB, and CheY, and  $B_p$  and  $Y_p$  are the concentrations of free CheB-P and CheY-P. CheB-P (either free or bound to a receptor) autodephosphorylates at a rate  $d_b$  and CheY-P is dephosphorylated by CheZ with a rate  $d_z$ . The levels of phosphorylated CheB and CheY then follow:

$$\frac{dB_{p,Tot}}{dt} = a_b A_p (B_{Tot} - B_{p,Tot}) - d_b B_{p,Tot}, \quad (2-9)$$

and

$$\frac{dY_p}{dt} = a_y A_p (Y_{tot} - Y_p) - d_z Z_{Tot} Y_p, \quad (2-10)$$

in which  $Z_{Tot}$  is the total concentration of CheZ molecules.

The molecular model depends on the biochemical parameters,  $k_r$ ,  $k_b$ ,  $K_r$ ,  $K_b$ ,  $a_p$ ,  $a_y$ ,  $d_z$ ,  $d_b$ ,  $a_b$ , which are the same for all cells since we consider isogenic populations (Methods section “Constant biochemical parameters of the model” below), and on the molecular abundance of  $A_{tot}$ ,  $T_{tot}$ ,  $R_{tot}$ ,  $B_{tot}$ ,  $Y_{tot}$ , and  $Z_{tot}$ .

#### Linearization of the molecular model

Eqs. (2–6,7,8,9,10) constitute a nonlinear system  $dX/dt = F(X) + S + H$  describing the evolution of  $X = (a, A_p, B_p, Y_p)$  in the presence of a stimulus  $S$  and noise source  $H$ .  $F$  is a vector-valued function specified by Eqs. (2–6,7,8,9,10). In the absence of stimulus  $S = 0$  the steady

state of the system  $X_0$  is the solution of  $F(X_0) = 0$ . For small stimuli and noise levels that induce only small changes  $\delta X = X - X_0$  about the steady-state, we may linearize the system to obtain

$$\delta \dot{X} = J \delta X + S + H, \quad (2-11)$$

in which  $J$  is the Jacobian of  $F$  evaluated at the steady state  $X_0$ :

$$J = \begin{pmatrix} \frac{\partial \dot{a}}{\partial a} & \dots & \frac{\partial \dot{a}}{\partial Y_p} \\ \vdots & \ddots & \vdots \\ \frac{\partial \dot{Y}_p}{\partial a} & \dots & \frac{\partial \dot{Y}_p}{\partial Y_p} \end{pmatrix}_{X=X_0}. \quad (2-12)$$

The eigenvalues of  $J$  for the model Eqs. (2–6,7,8,9,10) are generally negative, indicating that the system relaxes to its steady state after small perturbations. The methylation reactions of Eq. (2–6) are slow relative to the phosphorylation reactions described by Eqs. (2–8,9,10) and therefore effectively determine the rate of this relaxation. This rate is given by the largest (least negative) of the eigenvalues  $\lambda$  of  $J$ , which we use to define the relaxation time scale of the system

$$\tau = -\frac{1}{\max(\lambda)}. \quad (2-13)$$

We note that this rate sets the rate of relaxation to both external stimuli and intrinsic noise (Emonet & Cluzel, 2008; Park et al., 2010).

Magnitude of spontaneous fluctuations

Measurements(Park et al., 2010) have indicated that the variance  $\sigma_{Y_p}^2$  of intrinsic temporal fluctuations in CheY-P scales linearly with the relaxation time scale  $\tau$ , according to

$$\sigma_{Y_p}^2 = C\tau, \quad (2-14)$$

with  $C = 3.89 \times 10^{-3} \mu\text{M}^2/\text{s}$ . We assume these fluctuations arise solely from fluctuations in the mean methylation level  $m$ . Therefore, for a value of  $\tau$  calculated from the reaction constants and protein concentrations in a given cell, we choose the intensity of the noise source  $\eta_m(t)$  in

Eq. (6) so that  $\sigma_{Y_p}^2$  and  $\tau$  satisfy Eq. (2–14). Specifically, we first calculate  $\tau$  for a given cell and calculate the corresponding variance  $\sigma_{Y_p}^2$  from Eq. (2–14). Since the phosphorylation processes in Eqs. (2–8,9,10) are fast relative to the methylation process of Eq. (2–6), they may be considered to be in steady-state and Eq. (2–6) is effectively a one-dimensional Ornstein–Uhlenbeck process. We therefore can relate  $\sigma_{Y_p}^2$  to the variance of the intrinsic temporal fluctuations in the methylation level  $\sigma_m^2$  by

$$\sigma_m = \sigma_{Y_p} \left( \frac{dY_p}{da} \right)^{-1}. \quad (2-15)$$

Here,  $dY_p/da$  is calculated from the function  $Y_p(a)$ , Eq. (2–16) below, obtained from solving Eqs. (2–6,7,8,9,10) at steady state, as described fully in the next section. Since  $\tau$  corresponds to the relaxation time of the methylation process in Eq. (2–6), we then use  $\tau$  and  $\sigma_m^2$  to set the intensity of the noise source  $\eta_m(t)$  according to

$$\langle \eta_m(t) \eta_m(t') \rangle = 2\sigma_m^2 / \tau \delta(t - t') \quad (2-16)$$

in which  $\delta(t)$  is the Dirac delta.

#### Gene expression model

The reaction rates are assumed to be the same for all cells since the population we consider is isogenic. The total numbers of protein, however, do change from cell to cell and their distribution over the population are determined using a stochastic gene expression model described in this section.

We adapted a model (Lovdok et al., 2009) of noisy gene expression that produces individual cells each with an individual set of protein counts  $\mathbf{P} = [A_{Tot} \ W_{Tot} \ R_{Tot} \ B_{Tot} \ Y_{Tot} \ Z_{Tot} \ T_{Tot}]$ :

$$\mathbf{P} = \mathbf{P}_0 \left( \xi_{ex} + \sqrt{\xi_{ex}} \mathbf{A} \cdot \text{diag}(\eta) \cdot \xi_{in} \right), \quad (2-17)$$

where  $\mathbf{P}_0$  is the corresponding vector of mean protein levels in the population,  $\xi_{in}$  and  $\xi_{ex}$  are the intrinsic and extrinsic noise components (Swain et al., 2002), respectively,  $\eta$  is the scaling

of the intrinsic noise, and  $\mathbf{A}$  is the translational coupling matrix (Lovdok et al., 2009), a lower triangular matrix of correlation coefficients  $a_{ij}$  between proteins  $i$  and  $j$ . The intrinsic noise  $\xi_{in}$  is a vector of normally-distributed random variables with mean zero and variance one, providing individual uncorrelated noise sources for each protein. The extrinsic noise  $\xi_{ex}$  is a single lognormally-distributed random variable that provides correlated noise to all proteins together given by

$$\xi_{ex} = \frac{1}{e^{\frac{1}{2}(\omega\xi\ln(10))^2}} e^{\omega\xi\ln(10)}, \quad (2-18)$$

where  $\xi$  is a normally-distributed with mean zero and variance one, and  $\omega$  is a scaling parameter for the extrinsic noise.

Since many proteins of the pathway assemble into ultrastable membrane-associated complexes (Boldog, Grimme, Li, Sligar, & Hazelbauer, 2006; Zhang, Khursigara, Hartnell, & Subramaniam, 2007), the individual protein levels generated from the noisy gene expression model was further constrained by taking into account the experimentally observed stoichiometry: CheW docks to Tar and Tsr with 2:12 stoichiometry, CheA docks to receptor-associated CheW with 2:2 stoichiometry, and CheA is synthesized in two isoforms, CheAL and CheAS, with a 45:22 ratio (Li & Hazelbauer, 2004); only the CheAL form has kinase activity, CheZ docks to CheAS and has more activity than un-docked CheZ (Cantwell et al., 2003; Kentner & Sourjik, 2006, 2009; Schulmeister et al., 2008), so we assume for simplicity that only docked CheZ has significant activity. These relationships were used to determine the number of functional receptor complexes on a per-cell basis, producing final effective levels of  $Z_{tot}$ ,  $A_{tot}$ , and  $T_{tot}$  to be used in the single cell model described above. The extra copies of proteins not in complexes did not participate in signaling.

#### Constant biochemical parameters of the model

Before conducting any simulations or analysis, we performed a one-time fitting routine to fix some of the biochemical parameters, which we assume are the same for all cells since we consider isogenic populations. All of these parameter values were fixed from previous

experiments (Table 2–1) except for  $k_r$ ,  $k_b$ ,  $K_r$ ,  $K_b$  and  $a_p$ , which we fit to data. To perform the fitting, we set the population mean protein levels  $\mathbf{P}_0$  to the wildtype levels (Li & Hazelbauer, 2004) except where noted below to match a given dataset. Since the intrinsic and extrinsic noise scaling parameters  $\eta$  and  $\omega$  are unknown for wildtype cells, those were allowed to change along with the biochemical parameters that were being fitted. In summary, the biochemical parameters  $k_r$ ,  $k_b$ ,  $K_r$ ,  $K_b$ , and  $a_p$ , and the gene expression parameters  $\eta$  and  $\omega$  were used as the 7 fit parameters. After the fit was performed,  $\eta$  and  $\omega$  were allowed to vary again (i.e. in Figure 2–8 and the population optimization for Figure 2–9,10), but the biochemical parameters ( $k_r$ ,  $k_b$ ,  $K_r$ ,  $K_b$ ,  $a_p$ ,  $d_z$ ,  $d_b$ ,  $a_b$ ) were fixed permanently for all populations in all contexts.

As fit-data we used (i) measurements of the histogram of CW bias in a wildtype population and the adaptation times associated with each bin (Park et al., 2010) (Figure 2–1A); (ii) measurements of the population-average CW bias as a function of fold overexpression of the mean protein levels  $\mathbf{P}_0$  (Kollmann et al., 2005) (Figure 2–1B); and (iii) population-averaged relationship between receptor activity level and methylation rate (Shimizu et al., 2010) (Figure 2–1). To fit the later data we used our molecular model to simulate and reproduce the time-dependent experimental method used in these experiments: we simulated the response of CheY-P levels within populations of 100 immobilized cells to exponential ramps of ligand. We used the same ramp rates and “strain” ( $\Delta tsr$  cells) as in the experiments.

We used a cost function that was simply the sum squared error of all data points and corresponding model/simulation results. We minimized the cost function, allowing the 7 fit-parameters mentioned above to vary, using MATLAB’s pattern search optimization algorithm.

With a single set of parameter values, the resulting model agrees well with the fit data (Figure 2–1). Compared to single-cell measurements of the histogram of CW bias in the population, the model produces a similar spread (Figure 2–1A, bottom) and anti-correlation with adaptation time (Figure 2–1A, top) (Park et al., 2010). Despite this variation, the population-averaged CW bias is constrained within a functional range even when the mean level of proteins is globally upregulated (Figure 2–1B)—experimentally this was done by

inducing the expression of a master transcriptional regulator (Kollmann et al., 2005)—here we multiplied  $\mathbf{P}_0$  by the appropriate factor. This conservation shows that our model recapitulates and resolves a fundamental unexplained dichotomy in the chemotaxis pathway: population variability around the average is possible in addition to high robustness of the population average. Hence the pathway is sensitive to molecular noise at the single cell level, but robust at the population level. Finally, simulations of the population model to reproduce the experiment by Shimizu et al. (2010) show close agreement (Figure 2–1C), notably fitting the nonlinear behavior at low and high receptor activity levels without using a piecewise model or higher exponents in the methylation equation.

#### Phenotypic model of chemotaxis

The stochastic molecular model described above and its linearization specifies the stochastic behavior of the single cell in a given environment as a function of its biochemical parameters (e.g. reaction rates) and protein concentrations. In the following, we define the key phenotypic parameters of the system, adaptation time, tumble bias, and the dynamic range of CheY-P levels. We derive these quantities directly from the molecular model as a function of protein levels.

Consider the small changes in ligand concentration experienced by a cell moving in a gradient. In this linear regime, small perturbations in receptor activity around the mean steady-state value  $a_0$  (given by the steady state of Eq. (2–7)) will arise from either intrinsic molecular noise or from the external stimuli. The relaxation time of the system  $\tau$  (Eq. (2–13)) is determined by the time scale of methylation and demethylation, which are slow relative to all other reactions in the system (Table 2–1) and may therefore be considered at steady state relative to methylation. Under these conditions, we may construct a simplified version of the above pathway model with only a single SDE to describe the methylation dynamics. The end result is a phenotypic model specified only by the mean activity at steady-state  $a_0$ , the relaxation time scale  $\tau$ , and the total CheY concentration  $Y_{Tot}$  that controls the maximum level of CheY-P that the cells can reach and therefore the dynamic range of the response regulator.

In the phenotypic model, the dynamics of the mean receptor methylation level  $m$  are described by (Sneddon et al., 2012):

$$\frac{dm}{dt} = -\frac{1}{\tau}(m - m_0(L)) + \eta_m(t). \quad (2-19)$$

For a given ligand concentration  $L$ ,  $m_0(L)$  is the methylation level at which receptor activity is equal to its mean adapted level  $a_0$ . Therefore  $m_0$  satisfies  $a(m_0, L) = a_0$  with  $a$  given by Eq. (2-4) above and  $a_0$  given by the steady state of Eq. (2-7). The white noise source  $\eta_m$  is identical to that in Eq. (2-6) with intensity derived from  $\tau$  according to Eqs. (2-13,14,15,16).

The phosphorylation reactions described by Eqs. (2-8,9,10) are much faster than the methylation and demethylation reactions (Eq. (2-7)) that govern the slow adaptation of the cell and therefore are calculated using a steady-state approximation as in previous studies (Sneddon et al., 2012; Tu, Shimizu, & Berg, 2008; Vladimirov, Lovdok, Lebiedz, & Sourjik, 2008). Since the concentration of total CheB is small relative to total CheY ( $B_{Tot}/Y_{Tot} \ll 1$ ) and the rate of CheB phosphorylation is lower than the rate of CheY phosphorylation, the effect of CheB phosphorylation in Eq. (2-8) can be safely neglected. Solving Eqs. (2-8) and (2-10) then yields the following relationship between CheY-P concentration and the kinase activity  $a$ :

$$Y_p(a) = \frac{1}{2} \left( a \frac{a_p}{a_y} + Y_{tot} + a\alpha - \sqrt{-4aY_{tot}\alpha + \left( a \frac{a_p}{a_y} + Y_{tot} + a\alpha \right)^2} \right), \quad (2-20)$$

Where  $\alpha = \frac{A_{Tot}a_p}{Z_{Tot}d_z}$ . Phosphotransfer from CheA to CheY is rapid. Consequently, if  $Y_{tot}$  is sufficiently large that  $a_p \ll a_y Y_{tot}$ , then Eq. (20) reduces to  $Y_p(t) \equiv \alpha Y_{tot} a(t)$ . This linear relationship has been exploited by researchers using CheY–CheZ FRET as a read-out of kinase activity (Sourjik & Berg, 2001). Thus, for large  $Y_{tot}$ , the relationship between kinase activity  $a$  and CheY-P concentration is nearly linear with slope  $\alpha$ . (Further discussion under “Simulating performance of phenotypes.”)

In summary, we combined the phenotypic model in Eqs. (2–19,20) with the MWC receptor model in Eq. (2–4,5) and the flagellar motor switching model in Eq. (2–1,2,3) to produce a simplified model of the bacterial chemotaxis system in the linear regime. Using this model, an individual cell is fully specified by the three parameters: tumble bias, adaptation time, and the dynamic range of the response regulator CheY-P:

- The tumble bias can be obtained from the molecular model (Eqs. (2–6,7,8,9,10)) at steady state using the protein levels ( $A_{tot}$ ,  $T_{tot}$ , ...) and biochemical parameters ( $k_r$ ,  $k_b$ , ...) to first obtain  $a_0$  and  $Y_{p,SS}$  and then by using Eq. (2–3) to solve for the steady-state tumble bias as a function of  $Y_{p,SS}$ .
- The adaptation time can be obtained from Eqs. (2–12,13,14), which depend on the molecular model (Eqs. (2–6,7,8,9,10)) that is parameterized by the protein levels ( $A_{tot}$ ,  $T_{tot}$ , ...) and biochemical parameters ( $k_r$ ,  $k_b$ , ...). That value of adaptation time also directly sets the adaptation time in the phenotypic model described in Eq. (2–19).
- The dynamic range of the response regulator CheY-P is defined as  $Y_p(a=1)$  in Eq. (2–20) and is determined by the total number of CheY molecules in the cell,  $Y_{tot}$ . For large values of  $Y_{tot}$  the response regulator activity is linear with that of the kinase and therefore the maximum level of  $Y_p$  the cell can adopt is  $a$ . For lower values of  $Y_{tot}$ , the total amount of CheY proteins in the cells becomes limiting and the dynamic range of CheY-P diminishes proportionally to  $Y_{tot}$ .

The values of all parameters used in this study are given in Table 2–1.

#### Model parameter summary

Collectively our model therefore consists of the three classes of parameters:

- Biochemical parameters of the signaling network ( $k_r$ ,  $k_b$ ,  $K_r$ ,  $K_b$ ,  $a_p$ ,  $a_y$ ,  $d_z$ ,  $d_b$ ,  $a_b$ ) represent the physical kinetics of the proteins' enzymatic actions. In this dissertation, these parameters are fixed for all populations in all cases because we assume neither the protein-coding genes nor the pathway topology changes.

- Population parameters of the gene expression model ( $\mathbf{P}_0$ ,  $\eta$ ,  $\omega$ ) represent the genetic architecture (i.e. operons, promoters, and RBSs) of the chemotaxis genes shared by all individuals in the clonal population. In this dissertation, these parameters can vary at the population level (such as in Figure 2–8 and the population optimization for Figure 2–9,10) but are assumed to be the same among cells in a populations within a generation. Their role here is to determine the distribution of protein levels among individuals within a given population.
- Phenotypic parameters of the cell (adaptation time, tumble bias, dynamic range of the response regulator) control the dynamical behavior of the individual cell. These vary from cell to cell and are determined by the combination of the individual levels of protein generated by the populations' noisy gene expression parameters and the biochemical signaling network as described in Methods section “*Phenotypic Model of Chemotaxis*” above. These parameters were also varied manually to perform the parameter scans of cell dynamics.

#### Comparison of Molecular and Phenotypic Models

We tested the agreement between the molecular model specified by Eqs. (2–1,2,3,4,5,6,7,8,9,10) and the phenotypic model specified by Eqs. (2–1,2,3,4,5,19,20) in a simulation. First we performed deterministic simulations of immobilized cells being exposed to 50 s square pulses of attractant and compared the time traces of CheY-P output of the system (Figure 2–1DE) for a wide range of adaptation time, tumble bias, and  $Y_{\text{Tot}}$ . The two traces lie on top of each other, demonstrating agreement.

#### Stochastic simulations of the model in ecological challenges

##### Environment definitions

We simulated cell trajectories using the phenotypic model (Sneddon et al., 2012) in 3-D environments in which methyl-aspartate was diffusing. The sources of methyl-aspartate were

spherical and diffusion was modeled as a 1-D process with central symmetry extending from the center of the source, described by:

$$\frac{\partial L}{\partial t} = D \frac{1}{r^2} \frac{\partial}{\partial r} \left( r^2 \frac{\partial L}{\partial r} \right) \quad (2-21)$$

where  $L$  is the ligand concentration at radius  $r$ , in  $\mu\text{m}$ , from the center of the source and  $D$  is the diffusion coefficient of methyl-aspartate, in  $\mu\text{m}^2/\text{s}$ .

In the foraging simulations, the only boundary condition was that  $L$  goes to zero as  $r$  goes to infinity. The source simply diffused from its spherical initial condition, which was given by:

$$L(r, t=0) = \begin{cases} L_1 & r \leq R \\ 0 & r > R \end{cases}, \quad (2-22)$$

where  $L_1$  was the initial source concentration and  $R$  was the radius of the source. The solution of the gradient in space and time becomes

$$L(r, t) = L_1 \frac{1}{r} \sqrt{\frac{Dt}{\pi}} \left( e^{-\alpha^2} - e^{-\beta^2} \right) + L_1 \frac{1}{2} (\operatorname{erf}(\alpha) - \operatorname{erf}(\beta)), \quad (2-24)$$

where  $\alpha = \frac{r+R}{\sqrt{4Dt}}$  and  $\beta = \frac{r-R}{\sqrt{4Dt}}$ .

In the colonization simulations, there was an additional boundary condition to describe the persistence of the source as a permanent non-depleting zone:

$$L(r \leq R, t) = L_1, \quad (2-24)$$

resulting in the solution

$$L(r, t) = \begin{cases} L_1 & r \leq R \\ L_1 \frac{R}{r} \operatorname{erfc} \left( \frac{r-R}{\sqrt{2Dt}} \right) & r > R \end{cases}. \quad (2-25)$$

#### Simulating performance of phenotypes

To construct heatmaps, adaptation time was varied directly, and the internal parameters used to vary the tumble bias and dynamic range were  $Y_{pSS}$  and  $Y_{tot}$ , respectively. Adaptation time was scanned in 25 log-spaced steps over the interval [1,300] s.  $Y_{pSS}$  was scanned in 25 log-spaced steps over the interval [1.2,4]  $\mu\text{M}$  with an additional point at 0  $\mu\text{M}$ .  $Y_{tot}$  was scanned

in 10 log-spaced steps over the interval [820,82000] molecules/cell. For each combination of parameters, 6000–30000 replicates were simulated (more replicates were used for farther away sources).

To calculate foraging performance, individual cell replicates accumulated ligand along their trajectories during the simulation. At each time point,  $kL(t)dt$  was added to their total, where  $k$  is the uptake rate in  $\mu\text{mol}/\mu\text{M}/\text{s}$ ,  $L(t)$  is the concentration of ligand at the current cell position and time, and  $dt$  is the simulation timestep in seconds. Nutrient accumulation was cut-off after a certain time; for the cases in the main figures, this was 13 minutes—characterization of the effect other times are described below. For each phenotype, the performance was the average ligand accumulation of all replicates (Figure 2–3–1 left).

To calculate colonization performance, each cell replicate was first awarded an arrival time in minutes upon its first crossing of  $r = R$ . If it failed to cross in 15 min, its arrival time was infinity. Since we define performance as a quantity to be maximized rather than minimized, the performance of each replicate was defined as the reciprocal of the arrival time in  $\text{min}^{-1}$ ; infinite arrival time resulted in zero performance. The replicates of each phenotype were then averaged together to get the performance as a function of phenotype (Figure 2–3–2 left).

Replicate cells began at a single point on the spherical shell  $r = r_0$ , where  $r_0$  is the distance away that the source appears to the cells. Simulations in both tasks were performed for 15 minutes for several values of  $r_0$  (Figure 2–3–1,2 left). For all subsequent analysis, the heatmaps were smoothed and resampled at higher resolution in phenotype space (2–3–1,2 right). Performance was first smoothed over the original cell parameter mesh using a Gaussian kernel. A resampled parameter mesh was created on a 200 x 200 grid within the existing range of cell parameters. The performance values at the new grid points were interpolated from the smoothed performance heatmaps using spline interpolation. The same procedure was used for the fitness landscapes described later, but importantly all fitness calculations were performed on original unsmoothed raw data, then smoothing was applied, so we did not smooth twice.

To find the specialist in each environments, the top performing phenotype on the high-resolution parameter grid was screened out (Figure 2–3–1,2, diamonds). To plot the Pareto front for two environments, we scattered the performance of all values of adaptation time and  $Y_{pss}$  (for a given  $Y_{Tot}$ ) on the high-resolution grid to obtain a cloud in chemotactic performance space. We then screened out phenotypes which were *not outperformed* in environment 1 and *not outperformed* in environment 2 to form the Pareto front.

Changing time limits was explicitly considered in the Results for the colonization case. For foraging, reducing the time limit has little effect on sources that are nearby, but for far sources, it limits the success of high tumble bias dramatically, exaggerating the trends observed in the far cases (Figure 2–3–3). In this regime, time is a key parameter since the cells must explore to reach the front of the source before foraging it appreciably. As such, limiting the time has a disproportionate effect on these phenotypes.

As a result of these disproportionate effects in far environments, trade-offs become stronger when time is restricted (Figure 2–5). For the same four examples of two-environment near–far trade-offs, reducing the time consistently increases the curvature of the Pareto front. When 3 minutes are given, the transition of trade-offs from weak to strong occurs at a much more similar pair of environments. Therefore, if the environment has frequent turnover events, for example caused by turbulence that equilibrates the gradient, it strengthens trade-offs substantially.

In the cases shown in the Results section,  $L_1$  was 100 mM for foraging and 10 mM for colonization. If  $L_1$  is reduced (Figure 2–3–4), the colonization case is relatively unaffected, except that the trend in farther sources become exaggerated because cells have to explore longer before finding a detectable signal. There are more substantial changes to the foraging case. For farther sources especially, the preferred phenotypes switch to having high tumble bias. In these cases, exploration reduces the chances of the cells to see ligand because they became too spread out; rather, staying in one place and waiting for the diffusing nutrient front to arrive became the preferred strategy.

As we derived in equation (2–20), the dynamic range of CheY-P depends on  $Y_{Tot}$ , which sets the asymptotic value of CheY-P. In cells with low  $Y_{Tot}$ , phosphotransfer is hindered, reducing information transfer from the kinase to the motor and thus deteriorating performance. Cell performance is limited by low  $Y_{Tot}$ , but once it is high enough to reach the linear regime between kinase activity and CheY-P concentration, additional CheY does not add much benefit since the dynamic range of CheY-P activity will then become limited by the number of kinases.

We see in our simulations (Figure 2–3–5) that, above about  $Y_{Tot} = 10591$  molecules/cell, the performance does not appreciably change because this condition of linearity is met. From this, we conclude that there is no trade-off on  $Y_{Tot}$  apart from the cost of protein synthesis, and that cells should express enough CheY to reach the Pareto front. Beyond that, there is minimal increase in performance. In our analysis of the Pareto fronts, we used  $Y_{Tot} = 29469$  mol./cell for all cells; the results do not change significantly if the next higher or lower levels of  $Y_{Tot}$  are used instead.

#### Calculating fitness from performance

Fitness was assigned based on performance via a selection function. The fitness of each individual simulation trajectory was calculated, then all trajectories of a given phenotype were averaged together to produce the fitness of a given phenotype. This is clearly distinct from calculating the fitness of each phenotype's average performance. We used this procedure to create fitness landscapes which were then smoothed and resampled exactly as we did with the performance heatmaps.

Fitness was calculated on a single-cell (i.e. single-replicate) basis. For Figure 2–6, in the foraging case, our metabolic formula was  $f = \left[ 1 + (K / N_{col.})^n \right]^{-1}$ , where  $K$  is the amount of nutrition required for survival and  $n$  is the dependency; for colonization, our time-limit model was  $f = H(T_L - T_{arr.})$ , where  $T_L$  is the time limit, and  $H$  is the Heaviside step function.

For Figure 2–7, for the foraging case, different levels of nutrition were associated with discrete transitions to different physiological states. Below a survival threshold  $T_{survive}$ , the

individual dies, resulting in an outcome of 0 to signify no progeny. If the nutrition is above a higher division threshold  $T_{divide}$ , the individual gives rise to 2 progeny. Nutrition in between the two thresholds results in survival of the individual, or an outcome of 1 progeny. This model can be written as:  $f = H(N_{col} - T_{survive}) + H(N_{col} - T_{divide})$ . For colonization, if success depends on arrival time within a certain time limit  $K$ , but that dependency  $n$  is not absolute (i.e. infinite), this was described by a sigmoidal function like the Hill equation:

$$f(V) = 1 - \left(1 + \frac{K^n}{T_{arr.}^n}\right)^{-1}.$$

For each selection function and for each environment, the approach described above was used to create a lookup table for fitness as a function of phenotype. In order to calculate population fitness below, we first calculated the fitness of individual cells that are initially defined only by their levels of chemotaxis proteins. In order to find  $Y_{p,ss}$ , we solve the system of Eqs. (2–5, 7, 8, 9, 10). To find adaptation time we use the definitions in Eqs. (2–11, 12, 13).  $Y_{tot}$  is given as one of the protein levels. Given these three phenotypic parameters, we interpolate on the lookup table for any combination of task, environment, and selection function to give the corresponding fitness of that phenotype.

### Optimization of gene expression parameters under trade-offs

To optimize population fitness, we first defined a general expression for population fitness beginning with the fitness of a single phenotype. Chemotaxis is non-deterministic, hence, in each environment  $g$ , an individual phenotype  $\bar{x}$  had a distribution of performance  $V$ , or  $p(V | \bar{x}, g)$ , where  $\bar{x}$  is a vector of adaptation time, tumble bias, and CheY-P dynamic range. Fitness was a function of single-cell performance  $f(V)$ . To calculate the fitness of a phenotype in a given environment, we took the expected value of its fitness over its distribution of performance  $\langle f \rangle_{\bar{x}, g} = \int f(V) p(V | \bar{x}, g) dV$ . This should not be confused with the fitness of

the average performance  $f(\langle V \rangle|_{\bar{x}, g}) = f\left(\int p(V | \bar{x}, g) dV\right)$ .

We assume for simplicity that populations encounter challenges sequentially, all cells in the population experience each challenge simultaneously and in the same way, populations must survive through all environments, and individuals do not directly inherit phenotypes. Hence, within a given environment, a population consisting of many cells with different phenotypes has fitness equal to the average of its constituent cells  $\langle f \rangle_{P,g} = \int P(\bar{x}) \langle f \rangle_{\bar{x},g} dx$ , where  $P(\bar{x})$  is the population distribution of phenotypes. Following this, population fitness from one environment to the next is multiplicative. In the long term this results in a geometric mean across environments, weighted by the probability of encountering each environment:

$$F = \exp\left(\int \log\left(\int \langle f \rangle_{P,g}\right) h(g) dg\right), \quad (2-26)$$

where  $h(g)$  is the distribution of environments. This formula is consistent with previous derivations (Haccou & Iwasa, 1995) but has been extended to include stochastic performance of individual cells and a distinction between fitness and performance.

While equation (2–26) provides a general solution, in the specific cases analyzed in this study, the populations consist of a finite number of different phenotypes and for simplicity we show cases that compare two discrete environments  $g_1$  and  $g_2$  with occurrence probability  $h$  and  $(1 - h)$ . As such, the discrete calculation of population fitness becomes:

$$F = \left( \sum_{\xi=1}^{N_{pop}} \frac{f_{\xi,g_1}}{N_{pop}} \right)^h \left( \sum_{\xi=1}^{N_{pop}} \frac{f_{\xi,g_2}}{N_{pop}} \right)^{(1-h)}, \quad (2-27)$$

where  $\xi$  indexes the cells in the population,  $N_{pop}$  is the number of cells in the population, and  $f_{\xi,g}$  is the fitness of the phenotype of cell  $\xi$  in environment  $g$  determined using a look-up table constructed from simulation data as described above.

The trade-off problem itself is thus parameterized by:  $h$ ,  $g_1$ ,  $g_2$ , and the form and parameters of  $f(V)$  that gave rise to the look-up table. For example, in the case of foraging these are the nutritional requirement  $K$  and the dependency  $n$ ; for colonization there is only the time limit  $T_L$ . These we collectively called the trade-off parameters.

The population gene expression parameters generate a list of individuals with different phenotypes as described above. We can optimize the fitness of the population as a whole (Figure 2–9,10) by first calculating population fitness  $F$  (Eq. (2–27)) for a set of trade-off parameters. We then used MATLAB’s pattern search optimization function on the population fitness formula, allowing only the gene expression parameters  $\mathbf{P}_0$ ,  $\eta$ , and  $\omega$  to vary, but not the trade-off parameters, the biochemical parameters, or any other parameters. The noise parameters  $\eta$  and  $\omega$  initially had a lower constraint set to 0.04 and 0.02 respectively (Figure 2–9), then were changed to reflect biological measurements (Figure 2–10) as described below, and  $h$  was 0.8. From this we obtained the optimized population parameters for strong and weak trade-offs (performed separately). For each type of ecological task, the strong and weak trade-offs are between the same pair of near and far environments, with the same form of selection function, but each has a different set of selection function parameters.

Since there is always some irreducible noise in biology, we used experimental observations to provide lower bounds for the noise parameters in our model. For a limit on the intrinsic component, we took the wildtype level of intrinsic noise, which we obtained by fitting the model to wildtype data (described above). Multiple studies have described the advantage of reduced intrinsic noise in chemotaxis, so we assume wildtype cells are likely to be functioning at or near the minimum intrinsic noise. In order to apply this constraint, we ensure that the intrinsic noise scaling parameter and mean protein levels are constrained within the optimization algorithm such that the condition  $\eta\mathbf{P}_0 \geq \eta^{wt}\mathbf{P}_0^{wt}$  is maintained.

There is also a lower bound on the minimum total protein noise, defined as the coefficient of variation squared, measured in single *E. coli* cells to be about 0.09 for proteins with a mean expression level of above 100 copies per cell (Taniguchi et al., 2010). This constraint in practice acts more on extrinsic noise than on intrinsic noise since in our case the latter is typically fairly low. To enforce this constraint computationally, we ensure that  $\mathbf{P}_0$ ,  $\eta$ , and  $\omega$  of Eq. (2–2 through 2–18) are chosen by the optimization such that the squared coefficient of variation of every protein is above 0.09. This typically has the effect of keeping  $\omega$  above about 0.09, depending on

$P_0$  and  $\eta$ . Increases in global expression levels of up to approximately 3 fold are observed for different strains and growth media (Li & Hazelbauer, 2004), and using mutations in *flgM*, increases up to 7 fold are possible (Kollmann et al., 2005). Hence, we set our upper limit of mean expression levels at 5 fold to work within that range.

Receptor Parameters				
Name	Description	Type	Value	Reference
$\varepsilon_0$	Basal energy of receptor cluster	Fixed	6 k <sub>B</sub> T	(Shimizu et al., 2010)
$\varepsilon_1$	Receptor energy change per methyl group addition	Fixed	-1 k <sub>B</sub> T	(Shimizu et al., 2010)
$K_{TAR}^{off}$	Tar <sub>off</sub> -meAsp diss. constant	Fixed	18.2 μM	(Shimizu et al., 2010)
$K_{TAR}^{on}$	Tar <sub>on</sub> -meAsp diss. constant	Fixed	3000 μM	(Shimizu et al., 2010)
$K_{TSR}^{off}$	Tsr <sub>off</sub> -meAsp diss. constant	Fixed	10 <sup>4</sup> μM	(Endres & Wingreen, 2006)
$K_{TSR}^{on}$	Tsr <sub>on</sub> -meAsp diss. constant	Fixed	10 <sup>9</sup> μM	(Endres & Wingreen, 2006)
$N_{TAR}$	Number of Tar receptor dimers	Fixed	2 (6*)	(Shimizu et al., 2010), (Li & Hazelbauer, 2004)
$N_{TSR}$	Number of Tsr receptor dimers	Fixed	4 (0*)	(Shimizu et al., 2010), (Li & Hazelbauer, 2004)
Signaling Parameters				
Name	Description	Type	Value	Reference
$k_r$	Catalytic rate of CheR	Fitted	350 s <sup>-1</sup>	this study
$K_r$	Equilibrium constant of CheR activity	Fitted	300 μM	this study
$k_b$	Catalytic rate of CheB	Fitted	266 s <sup>-1</sup>	this study
$K_b$	Equilibrium constant of CheB activity	Fitted	200 μM	this study
$a_P$	CheA autophosphorylation rate	Fitted	12.5 s <sup>-1</sup>	this study
$a_B$	Rate of CheB phosphorylation by CheA	Fixed	15 μM <sup>-1</sup> s <sup>-1</sup>	Stewart, Jahreis, and Parkinson, 2000(Stewart, Jahreis, & Parkinson, 2000)
$d_B$	CheB autodephosphorylation rate	Fixed	0.5 s <sup>-1</sup>	Stewart, 1993(Stewart, 1993), (Kentner & Sourjik, 2006)
$a_Y$	Rate of CheY phosphorylation by CheA	Fixed	50 μM <sup>-1</sup> s <sup>-1</sup>	this study
$d_Z$	Rate of CheY desphosphorylation by CheZ	Fixed	5 μM <sup>-1</sup> s <sup>-1</sup>	this study
Motor Parameters				
Name	Description	Type	Value	Reference
$\omega_0$	Basal switching frequency	Fixed	1.3 s <sup>-1</sup>	(Sneddon et al., 2012), Cluzel et al., 2000(Cluzel et al., 2000)
$g_1$	Transition energy of motor	Fixed	40 k <sub>B</sub> T	(Sneddon et al., 2012), Cluzel et al., 2000(Cluzel et al., 2000)
$K_D$	Dissociation constant of CheY-motor interaction	Fixed	3.06 μM	(Sneddon et al., 2012), Cluzel et al., 2000(Cluzel et al., 2000)
Simulation Parameters				
Name	Description	Type	Value	Reference
$v$	Cell speed	Fixed	20 μm s <sup>-1</sup>	(Sneddon et al., 2012), (Berg & Brown, 1972)
$D_{ROT}$	Rotational diffusion	Fixed	0.062 rad s <sup>-1</sup>	(Sneddon et al., 2012), (Berg & Brown, 1972)
$k_{rot}$	Post-tumble redirection angle Gamma distribution shape parameter	Fixed	4	(Sneddon et al., 2012), (Berg & Brown, 1972)
$\theta_{rot}$	Post-tumble redirection angle Gamma distribution scale parameter	Fixed	18.32	(Sneddon et al., 2012), (Berg & Brown, 1972)

$D$	Diffusion coefficient of methyl-aspartate	Fixed	550 $\mu\text{m}^2 \text{s}^{-1}$	(Lewus & Ford, 2001)
$k$	Nutrient pickup rate	Fixed	$10^{-4}$ $\mu\text{mol}/\mu\text{M}/\text{s}$	<i>This study</i>
<b>Gene expression parameters</b>				
Name	Description	Type	Value	Reference
$\langle T \rangle$	Population mean receptors per cell (Tar + Tsr)	Population variable, fixed during fitting	15000 mol./cell	(Li & Hazelbauer, 2004)
$\langle A \rangle$	Population mean CheA proteins per cell	Population variable, fixed during fitting	6700 mol./cell	(Li & Hazelbauer, 2004)
$\langle W \rangle$	Population mean CheW proteins per cell	Population variable, fixed during fitting	6700 mol./cell	(Li & Hazelbauer, 2004)
$\langle R \rangle$	Population mean CheR proteins per cell	Population variable, fixed during fitting	140 mol./cell	(Li & Hazelbauer, 2004)
$\langle B \rangle$	Population mean CheB proteins per cell	Population variable, fixed during fitting	240 mol./cell	(Li & Hazelbauer, 2004)
$\langle Y \rangle$	Population mean CheY proteins per cell	Population variable, fixed during fitting	8200 mol./cell	(Li & Hazelbauer, 2004)
$\langle Z \rangle$	Population mean CheZ proteins per cell	Population variable, fixed during fitting	3200 mol./cell	(Li & Hazelbauer, 2004)
$x$	Conversion between mol./cell and $\mu\text{M}$ for proteins	Fixed	833 $\mu\text{M}/\text{mol.}/\text{cell}$	<i>this study</i>
$A_{RB}$	Translational coupling coefficient between CheR and CheB	Fixed	0.485	(Lovdok et al., 2009)
$A_{BY}$	Translational coupling coefficient between CheB and CheY	Fixed	0.210	(Lovdok et al., 2009)
$A_{YZ}$	Translational coupling coefficient between CheY and CheZ	Fixed	0.250	(Lovdok et al., 2009)
$\eta$	Intrinsic noise scaling coefficient	Population variable, fitted during fitting	0.125	<i>this study</i>
$\omega$	Extrinsic noise scaling coefficient	Population variable, fitted during fitting	0.26	<i>this study</i>

**Table 2–1. Parameter Values and Variables.**

\*Values in parentheses were used when directly comparison to Shimizu et al. (2010) to reflect the Tsr knockout mutation used in that study.

## References

- Berg, H. C., & Brown, D. A. (1972). Chemotaxis in *Escherichia coli* analysed by three-dimensional tracking. *Nature*, 239(5374), 500-504.
- Blackburn, N., Fenchel, T., & Mitchell, J. (1998). Microscale nutrient patches in planktonic habitats shown by chemotactic bacteria. *Science*, 282(5397), 2254-2256. doi: DOI 10.1126/science.282.5397.2254
- Boldog, T., Grimme, S., Li, M., Sligar, S. G., & Hazelbauer, G. L. (2006). Nanodiscs separate chemoreceptor oligomeric states and reveal their signaling properties. *Proc Natl Acad Sci U S A*, 103(31), 11509-11514. doi: 10.1073/pnas.0604988103
- Bruggeman, F. J., Bluthgen, N., & Westerhoff, H. V. (2009). Noise Management by Molecular Networks. *PLoS Comput Biol*, 5(9). doi: ARTN e1000506 DOI 10.1371/journal.pcbi.1000506
- Cantwell, B. J., Draheim, R. R., Weart, R. B., Nguyen, C., Stewart, R. C., & Manson, M. D. (2003). CheZ phosphatase localizes to chemoreceptor patches via CheA-short. *J Bacteriol*, 185(7), 2354-2361.
- Cluzel, P., Surette, M., & Leibler, S. (2000). An ultrasensitive bacterial motor revealed by monitoring signaling proteins in single cells. *Science*, 287(5458), 1652-1655.
- Dufour, Y. S., Fu, X., Hernandez-Nunez, L., & Emonet, T. (2014). Limits of feedback control in bacterial chemotaxis. *PLoS Comput Biol*, 10(6), e1003694. doi: 10.1371/journal.pcbi.1003694
- Emonet, T., & Cluzel, P. (2008). Relationship between cellular response and behavioral variability in bacterial chemotaxis. *Proc Natl Acad Sci U S A*, 105(9), 3304-3309. doi: 10.1073/pnas.0705463105
- Endres, R. G., & Wingreen, N. S. (2006). Precise adaptation in bacterial chemotaxis through "assistance neighborhoods". *Proceedings of the National Academy of Sciences of the United States of America*, 103(35), 13040-13044. doi: 10.1073/pnas.0603101103

- Freed, N. E., Silander, O. K., Stecher, B., Bohm, A., Hardt, W. D., & Ackermann, M. (2008). A simple screen to identify promoters conferring high levels of phenotypic noise. *PLoS Genet*, 4(12), e1000307. doi: 10.1371/journal.pgen.1000307
- Haccou, P., & Iwasa, Y. (1995). Optimal Mixed Strategies in Stochastic Environments. *Theoretical Population Biology*, 47(2), 212-243. doi: DOI 10.1006/tppb.1995.1009
- Kalinin, Y., Neumann, S., Sourjik, V., & Wu, M. M. (2010). Responses of Escherichia coli Bacteria to Two Opposing Chemoattractant Gradients Depend on the Chemoreceptor Ratio. *Journal of Bacteriology*, 192(7), 1796-1800. doi: Doi 10.1128/Jb.01507-09
- Kentner, D., & Sourjik, V. (2006). Spatial organization of the bacterial chemotaxis system. *Current Opinion in Microbiology*, 9(6), 619-624. doi: DOI 10.1016/j.mib.2006.10.012
- Kentner, D., & Sourjik, V. (2009). Dynamic map of protein interactions in the Escherichia coli chemotaxis pathway. *Molecular Systems Biology*, 5. doi: Artn 238 Doi 10.1038/Msb.2008.77
- Kollmann, M., Lovdok, L., Bartholome, K., Timmer, J., & Sourjik, V. (2005). Design principles of a bacterial signalling network. *Nature*, 438(7067), 504-507.
- Kussell, E., & Leibler, S. (2005). Phenotypic diversity, population growth, and information in fluctuating environments. *Science*, 309(5743), 2075-2078. doi: 10.1126/science.1114383
- Lane, M. C., Lockatell, V., Monterosso, G., Lamphier, D., Weinert, J., Hebel, J. R., . . . Mobley, H. L. T. (2005). Role of motility in the colonization of uropathogenic Escherichia coli in the urinary tract. *Infection and Immunity*, 73(11), 7644-7656. doi: Doi 10.1128/Iai.73.11.7644-7656.2005
- Lanfranconi, M. P., Alvarez, H. M., & Studdert, C. A. (2003). A strain isolated from gas oil-contaminated soil displays chemotaxis towards gas oil and hexadecane. *Environ Microbiol*, 5(10), 1002-1008.
- Lewus, P., & Ford, R. M. (2001). Quantification of random motility and chemotaxis bacterial transport coefficients using individual-cell and population-scale assays. *Biotechnology and Bioengineering*, 75(3), 292-304. doi: Doi 10.1002/Bit.10021

- Li, M. S., & Hazelbauer, G. L. (2004). Cellular stoichiometry of the components of the chemotaxis signaling complex. *Journal of Bacteriology*, 186(12), 3687-3694. doi: DOI 10.1128/Jb.186.12.3687-3694.2004
- Lovdok, L., Bentele, K., Vladimirov, N., Muller, A., Pop, F. S., Lebiedz, D., . . . Sourjik, V. (2009). Role of translational coupling in robustness of bacterial chemotaxis pathway. *PLoS Biol*, 7(8), e1000171. doi: 10.1371/journal.pbio.1000171
- Lovdok, L., Kollmann, M., & Sourjik, V. (2007). Co-expression of signaling proteins improves robustness of the bacterial chemotaxis pathway. *Journal of Biotechnology*, 129(2), 173-180. doi: DOI 10.1016/j.jbiotec.2007.01.024
- Mello, B. A., & Tu, Y. (2005). An allosteric model for heterogeneous receptor complexes: understanding bacterial chemotaxis responses to multiple stimuli. *Proc Natl Acad Sci U S A*, 102(48), 17354-17359. doi: 10.1073/pnas.0506961102
- Mesibov, R., & Adler, J. (1972). Chemotaxis toward Amino-Acids in Escherichia-Coli. *Journal of Bacteriology*, 112(1), 315-&.
- Miller-Jensen, K., Skupsky, R., Shah, P. S., Arkin, A. P., & Schaffer, D. V. (2013). Genetic selection for context-dependent stochastic phenotypes: Sp1 and TATA mutations increase phenotypic noise in HIV-1 gene expression. *PLoS Comput Biol*, 9(7), e1003135. doi: 10.1371/journal.pcbi.1003135
- Oleksiuk, O., Jakovljevic, V., Vladimirov, N., Carvalho, R., Paster, E., Ryu, W. S., . . . Sourjik, V. (2011). Thermal robustness of signaling in bacterial chemotaxis. *Cell*, 145(2), 312-321. doi: 10.1016/j.cell.2011.03.013
- Park, H., Guet, C. C., Emonet, T., & Cluzel, P. (2011). Fine-Tuning of Chemotactic Response in *E. coli* Determined by High-Throughput Capillary Assay. *Current Microbiology*, 62(3), 764-769. doi: DOI 10.1007/s00284-010-9778-z
- Park, H., Pontius, W., Guet, C.C., Marko, J.F., Emonet, T., & Cluzel, P. (2010). Interdependence of behavioural variability and response to small stimuli in bacteria. *Nature*, 468(7325), 819-823.

- Pontius, W., Sneddon, M. W., & Emonet, T. (2013). Adaptation dynamics in densely clustered chemoreceptors. *PLoS Comput Biol*, 9(9), e1003230. doi: 10.1371/journal.pcbi.1003230
- Schulmeister, S., Ruttorf, M., Thiem, S., Kentner, D., Lebiedz, D., & Sourjik, V. (2008). Protein exchange dynamics at chemoreceptor clusters in Escherichia coli. *Proc Natl Acad Sci U S A*, 105(17), 6403-6408. doi: 10.1073/pnas.0710611105
- Scott, M., Gunderson, C. W., Mateescu, E. M., Zhang, Z., & Hwa, T. (2010). Interdependence of cell growth and gene expression: origins and consequences. *Science*, 330(6007), 1099-1102. doi: 10.1126/science.1192588
- Shimizu, T. S., Tu, Y. H., & Berg, H. C. (2010). A modular gradient-sensing network for chemotaxis in Escherichia coli revealed by responses to time-varying stimuli. *Molecular Systems Biology*, 6. doi: Artn 382 Doi 10.1038/Msb.2010.37
- Shoval, O., Sheftel, H., Shinar, G., Hart, Y., Ramote, O., Mayo, A., . . . Alon, U. (2012). Evolutionary trade-offs, Pareto optimality, and the geometry of phenotype space. *Science*, 336(6085), 1157-1160. doi: 10.1126/science.1217405
- Sneddon, M. W., Pontius, W., & Emonet, T. (2012). Stochastic coordination of multiple actuators reduces latency and improves chemotactic response in bacteria. *Proceedings of the National Academy of Sciences of the United States of America*, 109(3), 805-810. doi: 10.1073/pnas.1113706109
- Sourjik, V., & Berg, H. C. (2001). Using fluorescent resonance energy transfer (FRET) to study interactions of cytoplasmic and motor proteins in chemotaxis of E-coli. *Biophysical Journal*, 80(1), 198a-198a.
- Stewart, R. C. (1993). Activating and inhibitory mutations in the regulatory domain of CheB, the methylesterase in bacterial chemotaxis. *J Biol Chem*, 268(3), 1921-1930.
- Stewart, R. C., Jahreis, K., & Parkinson, J. S. (2000). Rapid phosphotransfer to CheY from a CheA protein lacking the CheY-binding domain. *Biochemistry*, 39(43), 13157-13165.
- Swain, P. S., Elowitz, M. B., & Siggia, E. D. (2002). Intrinsic and extrinsic contributions to stochasticity in gene expression. *Proc Natl Acad Sci U S A*, 99(20), 12795-12800.

Taniguchi, Y., Choi, P. J., Li, G. W., Chen, H., Babu, M., Hearn, J., . . . Xie, X. S. (2010).

Quantifying *E. coli* proteome and transcriptome with single-molecule sensitivity in single cells. *Science*, 329(5991), 533-538. doi: 10.1126/science.1188308

Tu, Y., & Grinstein, G. (2005). How white noise generates power-law switching in bacterial flagellar motors. *Phys Rev Lett*, 94(20), 208101.

Tu, Y., Shimizu, T. S., & Berg, H. C. (2008). Modeling the chemotactic response of *Escherichia coli* to time-varying stimuli. *Proc Natl Acad Sci U S A*, 105(39), 14855-14860. doi: 10.1073/pnas.0807569105

Vladimirov, N., Lovdok, L., Lebiedz, D., & Sourjik, V. (2008). Dependence of bacterial chemotaxis on gradient shape and adaptation rate. *PLoS Comput Biol*, 4(12), e1000242. doi: 10.1371/journal.pcbi.1000242

Zhang, P., Khursigara, C. M., Hartnell, L. M., & Subramaniam, S. (2007). Direct visualization of *Escherichia coli* chemotaxis receptor arrays using cryo-electron microscopy. *Proc Natl Acad Sci U S A*, 104(10), 3777-3781. doi: 10.1073/pnas.0610106104





## Part 3: Experiments

Clonal cells contain subpopulations with different chemotactic performance 

### Introduction

Individual *Escherichia coli* bacteria exhibit substantial differences in chemotactic behavior despite sharing the same genetically encoded machinery. This has been experimentally characterized in cells that are immobilized, either on the surface of a glass slide (Cluzel, Surette, & Leibler, 2000; Park et al., 2010; Spudich & Koshland, 1976) or in an optical trap (Mears, Koirala, Rao, Golding, & Chemla, 2014). In freely-swimming wildtype cells interacting with their environment, however, it is unknown how this variability affects chemotactic performance in a gradient, either on a single-cell basis or on the population as a whole. Predictions about such outcomes are made in Part 2, but must be tested experimentally.

In this Part, we characterize the consequences of phenotypic diversity for population performance first by using the classic capillary assay and then by tracking cells in a microfluidic chemoattractant gradient. As cells explore the environment and climb a gradient, we find that a clonal wildtype population segregates in space and time into behaviorally distinct subpopulations. Some subpopulations explore and climb the gradient faster than others. When the gradient is reversed, however, and cells are challenged to localize near a source, different subpopulations perform best. Following simulation results in Part 2, these results support the existence of near–far trade-off in *E. coli* chemotaxis, which may be a type of the canonical exploration–exploitation trade-off widely discussed in the context of foraging of patchy environments (Eliassen, Jorgensen, Mangel, & Giske, 2007; Krakauer & RodriguezGirones, 1995; Seymour, Marcos, & Stocker, 2009; Stocker, Seymour, Samadani, Hunt, & Polz, 2008; Taylor & Stocker, 2012).

In order to test the underlying role of chemotaxis protein copy number, we constructed a strain in which CheR was expressed under inducible control. By tuning the mean expression level of CheR, we found that cells with low CheR climbed shallower gradients faster, whereas higher levels produce better performance in steeper gradients. Additionally, capillaries filled with higher concentration of attractant selected for subpopulations with higher CheR than capillaries with lower concentrations. This “steepness” trade-off is also consistent with theoretical predictions from Part 2 and with recently published models (Dufour, Fu, Hernandez-Nunez, & Emonet, 2014). In total, our result that wildtype populations contains different cells that are specialized to different tasks provides experimental support for our theoretical claim that behavioral heterogeneity may provide robustness in fluctuating environments.

## Results

Single-cell capillary assay exerts selection on protein level

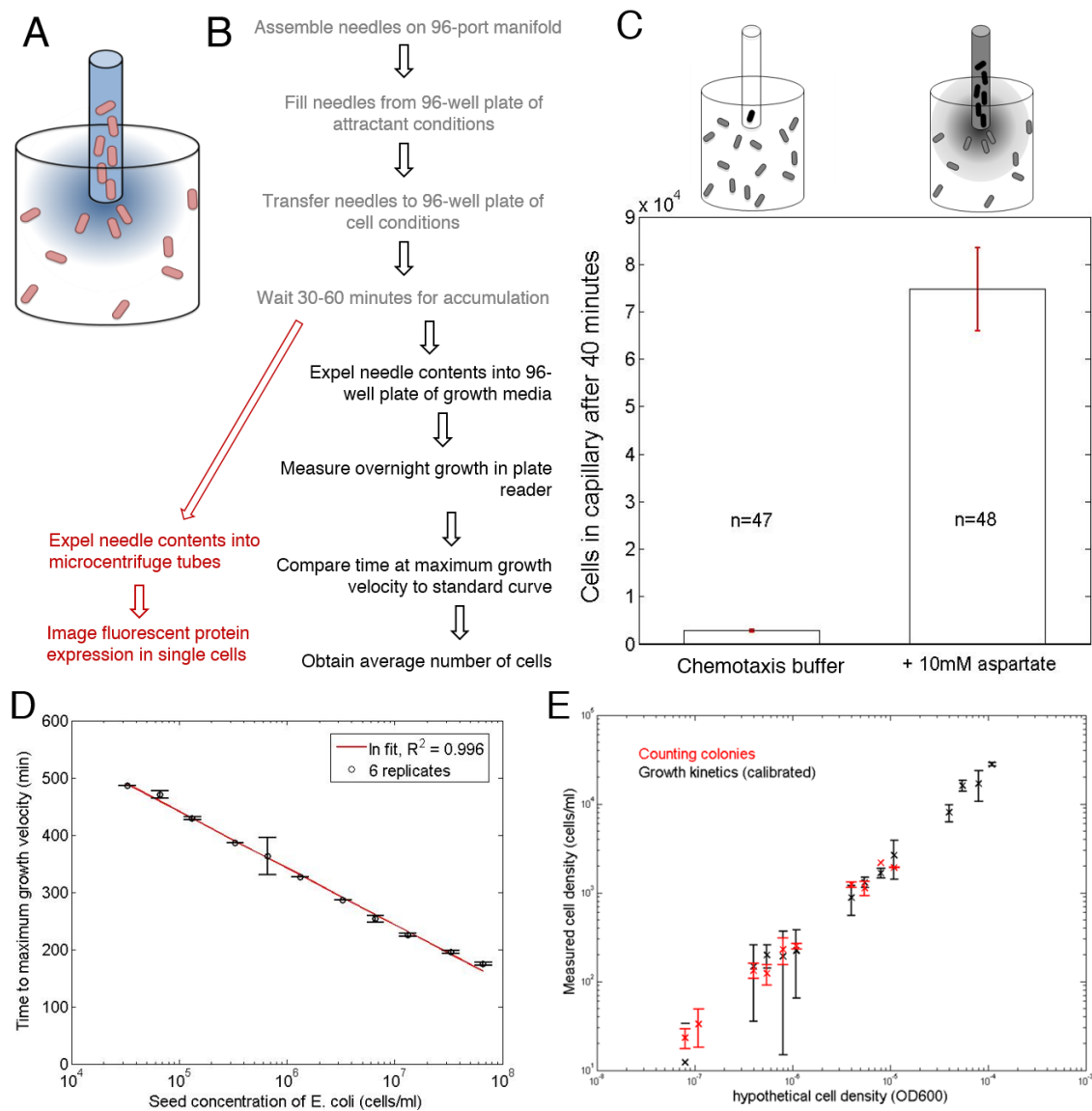
To test cell performance we first tried Adler’s capillary assay. This assay consists of presenting an attractant-filled capillary tube to a well of cells in buffer and counting the number of cells that swim into the capillary over a certain time (Mesibov & Adler, 1972) (Figure 3–1A). This can be modified to a high-throughput version performed on 96-well plates of cells (Bainer, Park, & Cluzel, 2003; Park, Guet, Emonet, & Cluzel, 2011) (Figure 3–1B). We validated our use of this assay by demonstrating a specific response to the amino acid aspartate (Figure 3–1C) after calibrating the counting of cells (Figure 3–1DE).

We presented cells with capillaries containing a dilution series of aspartate and constructed a dose-response curve that followed the trend of Adler’s early findings (Figure 3–2A), although substantial day-to-day variability was observed. To see if cell phenotype plays a role in capillary assay performance, we used a strain that is deleted for CheR on the chromosome and expresses a YFP-CheR fusion from an inducible promoter on a low-copy plasmid (NB: This is not the same strain we use later, which expresses mCherry-CheR from a single-copy

chromosomal promoter). When we raised the mean expression level of CheR in the population with increasing levels of the inducer isopropylthiogalactopyranoside (IPTG), we found that this resulted in substantially different average performance, with an intermediate induction level performing optimally (Figure 3–2B). The fact that performance tapers off at high and low YFP-CheR is consistent with expectations since these cells would have very low or very high tumble bias, respectively.

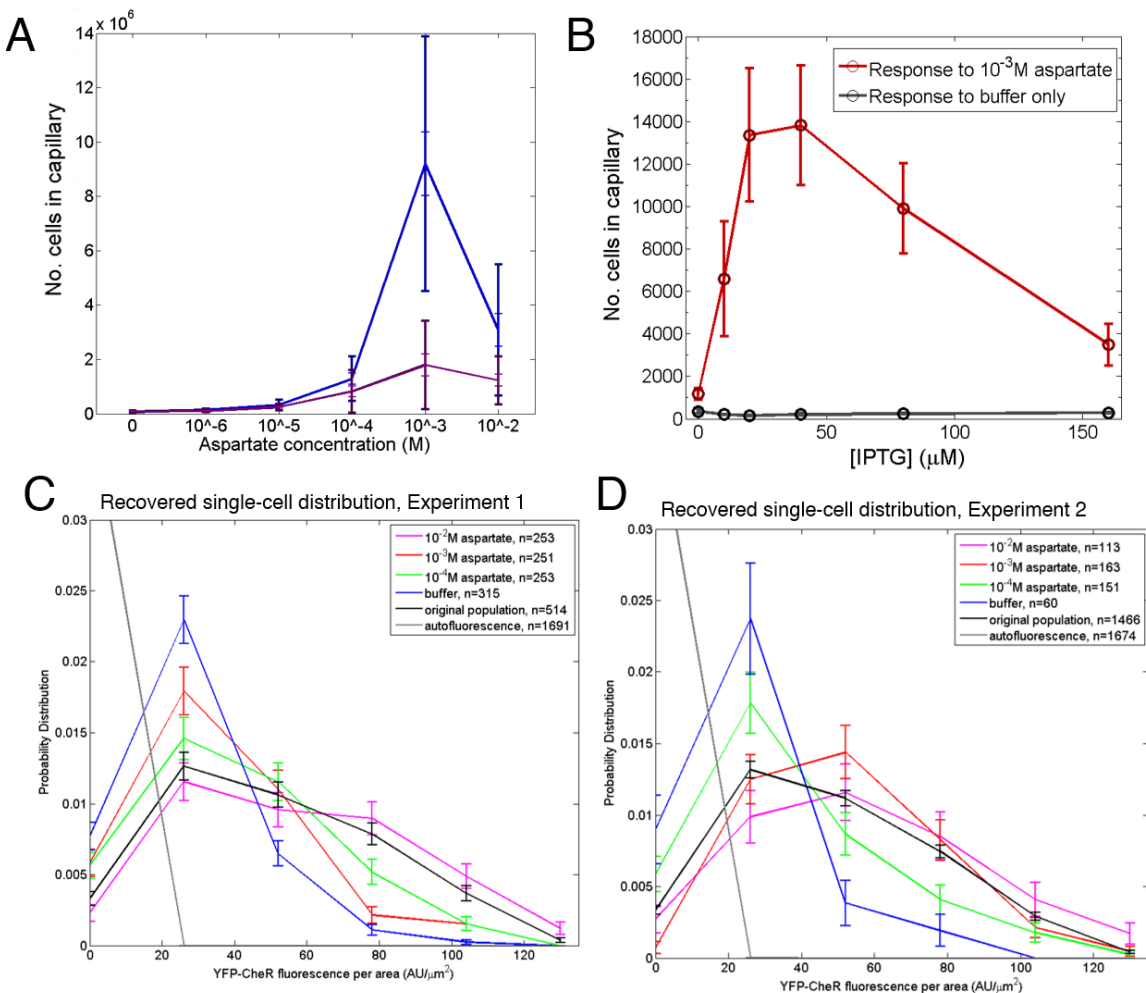
To continue this analysis at the single-cell level, we used an intermediate level of CheR induction and presented the same population with many separate capillary attractant concentrations. Following the red arrow in the flow chart in Figure 3–1B, instead of counting the cells, we expelled the cells that successfully entered the capillary onto agarose pads and imaged fluorescence levels in single cells at 100X magnification. We then compared the original distribution of YFP-CheR expression to the distributions in the winning subpopulations (Figure 3–2CD, two full experiment replicates).

Although replicates of the assay look slightly different, some trends in the winning distribution of CheR relative to the original distribution can be observed as a function of capillary attractant condition. For the highest concentration of aspartate in the capillary (Figure 3–2CD, 10 mM, magenta lines), high expression levels of YFP-CheR are more common than in the seed distribution, whereas lower concentrations of aspartate in the capillary result in winning populations with distributions of YFP-CheR shifted to lower levels. Finally, in capillaries filled with buffer only, which contained cells that only entered due to chance, the winning distribution had a YFP-CheR distribution that was most down-shifted, which as we show later (Figure 3–8) corresponds to a population with much longer runs.



**Figure 3-1. Quantification of high-throughput capillary assay performance**

**A.** Schematic of capillary assay. Cells (red ovals) in a well with buffer (wide cylinder) swim into a capillary (narrow cylinder) filled with attractant (blue color). **B.** Flow chart of high-throughput capillary assay procedure. Black: method for traditional cell counting. Red: method for measuring single-cell distributions. **C.** High throughput capillary assay response of RP437 cells,  $n$  = number of wells on 96-well plate with that condition. **D.** Calibration curve of growth kinetics in plate reader for use as a quantification method for high throughput capillary assay (8 wells per condition). **E.** Verification of agreement between growth-kinetics quantification method in D (black points) with traditional CFU counting (red points). In this figure, error bars represent +/- standard error of the mean (SEM).

**Figure 3-2. Effect of variability in YFP-CheR expression on capillary assay performance**

**A.** High-throughput capillary assay response of RP437 cells to several dilutions of aspartate on one plate, 12 wells per condition. Blue and purple series are different experiments on different 96-well plates. Inner error bars are  $\pm$  SEM, outer error bars are  $\pm$  standard deviation. **B.** High-throughput capillary assay response to either buffer (gray) or 1 mM aspartate (red) of IPTG-inducible YFP-CheR expressing cells grown in different concentration of IPTG. Single plate, 6–8 wells per condition. Error bars are  $\pm$  SEM. **C.** Distributions of YFP-CheR fluorescence (normalized to cell area) in subpopulations of cells that successfully entered capillaries with different chemoattractant conditions (different colors) compared to the seed population (black) on a single plate. Gray: autofluorescence of wildtype cells in identical imaging conditions.  $n$  = number of cells measured (Note: number of cells measured is not correlated with number of cells in capillary). Error bars are  $\pm \sqrt{n_{bin}}$ . **D.** Replicate of C.

These findings show that different levels of CheR produce different performance on average and that different conditions can select for different subpopulations of CheR expression. The trends are roughly consistent with simulation predictions from Part 2 and recent modeling work (Dufour et al., 2014), wherein steeper gradients or nearby strong sources require higher tumble bias and shorter adaptation time compared to shallower gradients or farther sources. High tumble bias and short adaptation time are both produced by elevated CheR, and the converse by reduced CheR. This assay was not replicable enough to explore this potential agreement in greater detail (Figure 3–2A blue versus purple, Figure 3–2C versus D), so we continued pursuit of this topic in a microfluidic platform that offered more precise control of the cells' microenvironment.

#### Microfluidic measurements of chemotactic behavior of cells and populations

We created a microfluidic device to track individuals within a clonal population as they performed chemotaxis in different gradient conditions (Figure 3–3). The main chamber of the device in which cells were tracked was 10 mm across by 1 mm wide by 10  $\mu\text{m}$  deep. These dimensions ensured that cells were always in the focal plane of a 10X objective and were in an essentially one-dimensional environment. In order to accurately track the spatiotemporal evolution of the population, the design had to be such the gradient was constant in time, cells were not pushed by flows, and all cells began the assay at the same location.

The first two constraints were satisfied by a source–sink gradient system in which circulation of buffer on one side and chemoattractant on the other were separated from the main channel by thin hydrogel barriers (Figure 3–3, gray regions). These membranes, made of poly(ethylene glycol), prohibited bulk flow that would push cells, but allowed chemoattractant to diffuse across and, after equilibration, form a stable gradient. We used a non-metabolizable attractant, alpha-methyl-aspartate, and mixed it with fluorescein dye to allow the gradient to be visualized via fluorescence microscopy. Fluorescein and meAsp have similar diffusion coefficients ( $5 \times 10^{-10}$  vs.  $5.5 \times 10^{-10} \text{ m}^2\text{s}^{-1}$ ) (Lewus & Ford, 2001). To meet the third constraint, cells were loaded behind a pressure-actuated gate (Figure 3–3B , blue line), which pinched off

the first 0.1 mm of the main chamber, detaining the population at one end of the device until the assay was begun.

At the start of the assay, the pressure-actuated gate was lifted and an automated acquisition program was simultaneously initiated. One-minute movies were captured at 10X magnification across the device in locations spaced ~1 mm apart, scanning from origin to end repeatedly in a raster pattern over several hours (Figure 3–4A), to image the expansion of the population. Before and after each movie, a fluorescence image was captured to measure the gradient profile (Figure 3–3A).

We performed particle tracking on each movie (Methods), which yielded a trajectory for each individual cell (Figure 3–4B). To characterize individual cell behavior, we calculated tumble bias by assigning each frame in a cell’s trajectory as either run or tumble (Methods). The tumble bias of each cell was then the fraction of the trajectory spent tumbling. By arranging this data by stage position and acquisition time (Figure 3–4D), this procedure furnished us space–time distributions of cell density, tumble bias, and methyl-aspartate concentration.

Clonal populations segregate spatiotemporally into distinct subpopulations

We first performed the assay without chemoattractant to measure the baseline exploration behavior of wildtype bacteria. The evolution of cell density across the device over time demonstrates population diffusion (Figure 3–5E). The tumbling probability was higher near the start point of the device, with the expanding diffusive front being composed of low tumble bias cells (Figure 3–5F). This demonstrates spatial separation of the population by tumble bias over time. Indeed a distribution of tumble bias was observed in the assay (Figure 3–5G), with the mean position of low tumble bias cells progressing faster from the origin due to diffusion than the mean position of high tumble bias cells (Figure 3–5H). Therefore, in the absence of a gradient, the fraction of wildtype cells that have low tumble bias explore the farthest.

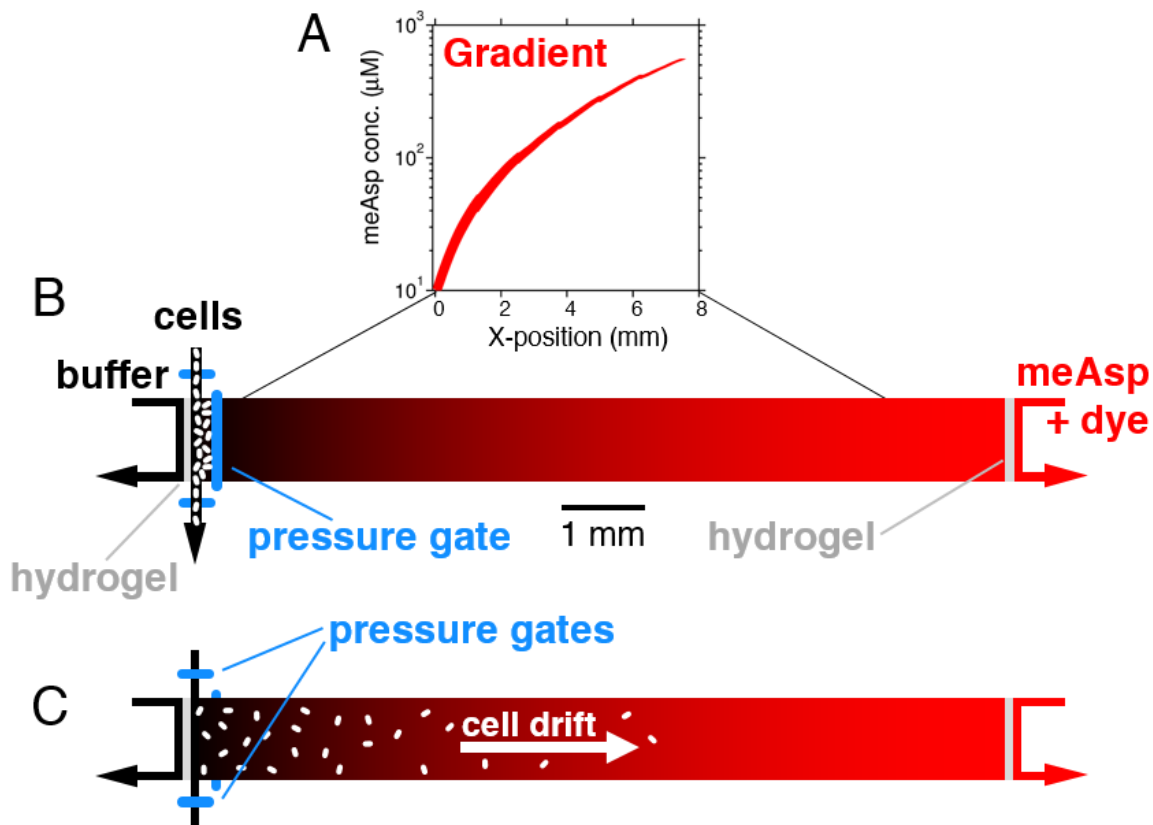


**Figure 3–3. Characterization of chemotaxis phenotypes in a gradient.**

**A.** Gradient of methyl-aspartate (meAsp) and fluorescein in a microfluidic device measured via fluorescence microscopy. After a 6 hr equilibration, 3 hrs of measurements are shown superimposed, demonstrating high stability of the profile. During each experiment, several 1.3 mm-long images are acquired across the main chamber at 10X magnification through a YFP filter set. After background subtraction, correction for the illumination field, and calibration to maximum fluorescein concentration, the intensity is averaged across the non-gradient dimension to obtain 1-D profiles of the gradient. These profiles are arranged according to the stage position and time. **B.** Schematic of the pre-experiment device setup, approximately to scale. Hydrogel barriers (gray) separate continuous flow of buffer and attractant to allow gradient establishment by diffusion and to prevent cross-flow in the main channel. Then cells (white ovals) are loaded behind a pressure-actuated control valve gate (blue bar). **C.** To start the experiment, the stream of cells into the main chamber is first shut off with pressure gates, and then cells are released into main channel simultaneously by lifting the large pressure gate, allowing them to drift up the gradient (red color) by chemotaxis without flow. Note: gradient profile in A was measured by A.

J. Waite.

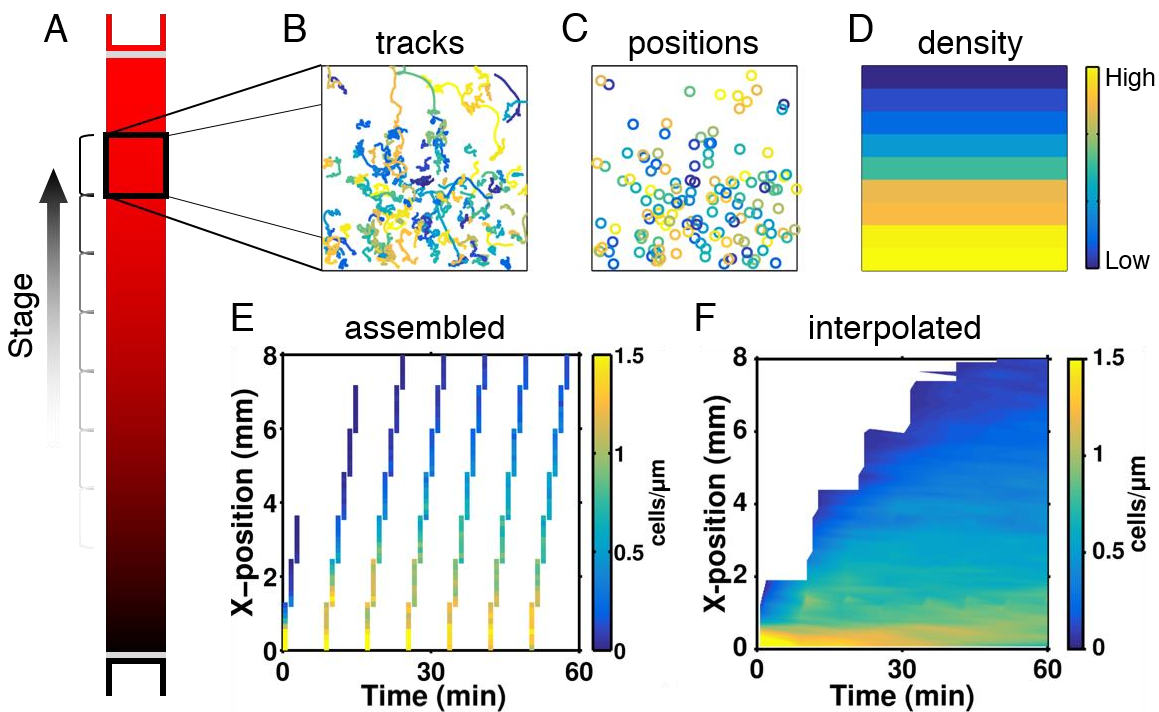


**Figure 3–4. Acquiring and processing data from the microfluidic gradient experiment.**

**A.** Cells are released into the gradient (see Figure 3–3), then a motorized stage scans the chamber, taking 1 min movies at 10X magnification in phase contrast spaced 1.2 mm apart. The movies consist of 1.3 mm square frames captured at 8 per second. **B–E** Example of data from an experiment wherein wildtype RP437 cells are exposed to a gradient from 0 to 1 mM meAsp over 10 mm over several hours (see also Figure 3–5 IJKL). **B–C.** Example of data from the first movie of the experiment. From each movie, cell tracks were extracted (B), giving the mean position of cells (C) and tumble bias (shown in Figure 3–5J). Positions were binned in spatial stripes perpendicular to the gradient to calculate the cell density across the frame (D). **E.** Many density measurements as in D are taken across the device over time and assembled on a space and time coordinate system using the X-position of the stage and the time at which the movie was taken. Each vertical strip comes from one movie. **F.** Additional space and time points are interpolated from the data in E to achieve a smooth kymograph to better visualize the cell density as the population climbs the meAsp gradient. Regions with fewer than 10 cells were omitted.

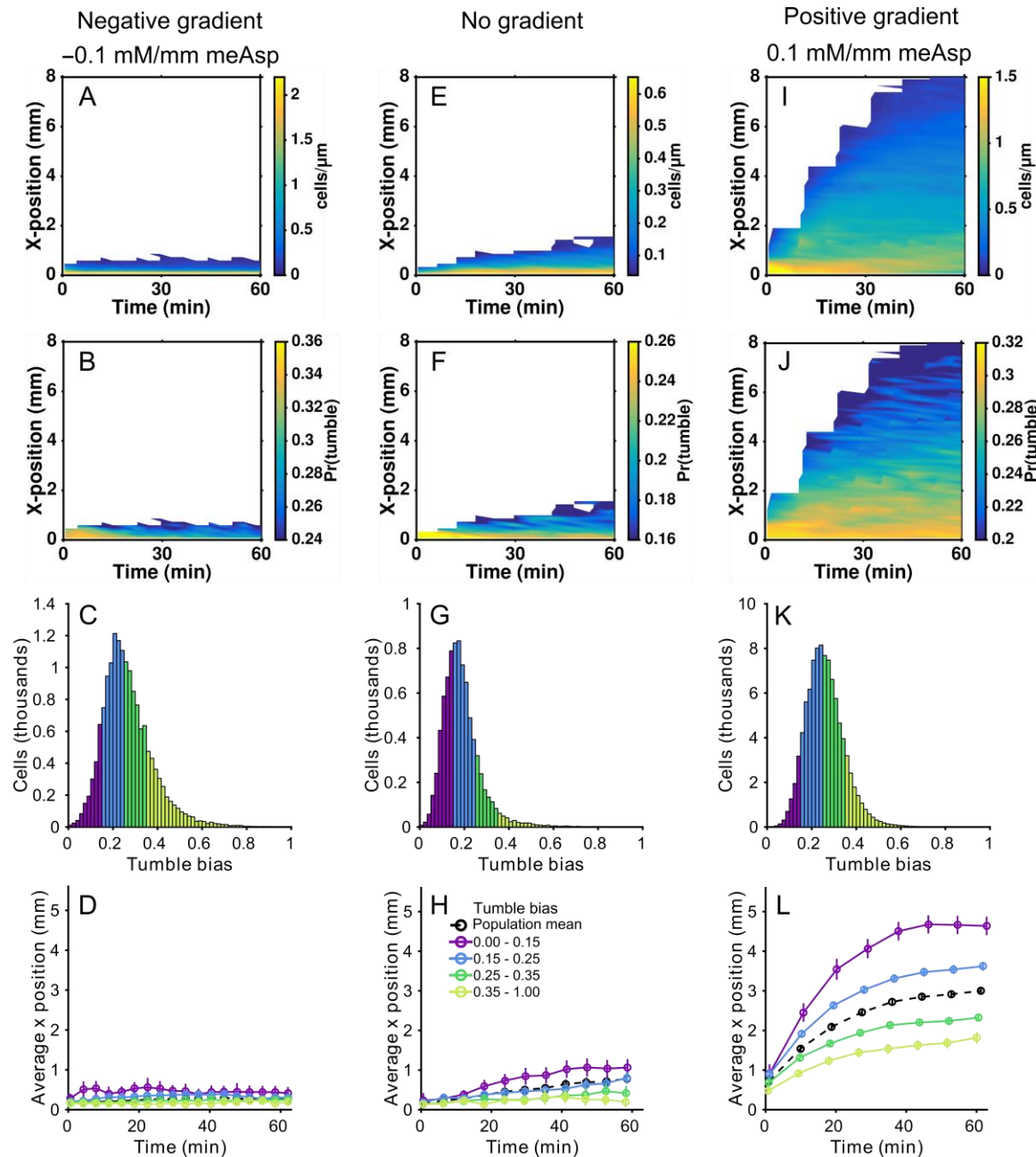


**Figure 3–5. (Opposite page) Performance of different phenotypes in different environments.**

Comparison of wildtype performance in three environments: no gradient (E–H); 0.1 mM/mm gradient of meAsp (I–L) with cells beginning at 0 mM; –0.1 mM/mm gradient with cells beginning at 1 mM (A–D). **A, E, I.** Kymographs of cell density along the device over time demonstrate diffusion (E), gradient-climbing (I), and localization at a source (A). Kymographs were generated by interpolating between raw measurements as shown in Figure 3–4. **B, F, J.** Average tumbling probability across  $x$  and time determined by analyzing run and tumble states of all trajectories. Only locations with at least 10 cells were included. **C, G, K.** Tumble bias distributions of the populations. Only tracks longer than 15 sec were included to reduce error. **D, H, L.** Performance of populations and subpopulations. Mean position over time of the entire population (black dashed line and black circles) or of the same population separated into subpopulations by tumble bias (solid colored lines and circles). Each time point contains data from one pass of the stage. Error bars indicate  $\pm 2\times$ SEM. For E–H, only the first 5 mm of the 10 mm main chamber was scanned. For I–L and A–D, 8 mm and 3 mm were scanned, respectively. In each column, two experimental replicates were combined. Note: Diffusion experiment in E–H performed by A. J. Waite.

When we performed the assay with a chemoattractant gradient going from 0 to 1 mM methyl-aspartate across the device, the distribution of cell density moved up the gradient faster than in the no-gradient case (Figure 3–5I). As in the diffusion case, the population separated spatially into different subpopulations of tumble bias (Figure 3–5J), with low tumble bias cells at the front. Accordingly, tracking the mean position of low tumble bias cells over time demonstrates the fastest gradient climbing performance (Figure 3–5L).

We hypothesized that the apparent separation of cells by tumble bias was more due to stable underlying phenotypic diversity in the steady-state tumble bias rather than a transient response of cells with the same tumble bias to differences in the local gradient. Simulations of diversified versus non-diversified populations support this hypothesis (Figure 3–6). We used the virtual wildtype population from Part 2, which has a distribution of steady-state tumble bias across cells, and simulated its performance in the gradient and geometry of our

microfluidic device (Methods). We then treated the simulated trajectories as if they were experimental measurements and calculated tumble bias based on the observed tumble probability within discrete time and space windows.

Different tumble probability was observed across the simulated device similarly to the experiment (Figure 3–6A). Simulating a population of cells with a single phenotype instead of the wildtype distribution resulted in a very homogeneous probability of tumbling observed across the experiment, comparing unfavorably with the data (Figure 3–6B). This implies that the observed diversity of tumbling probability in space and time can be plausibly accounted for by underlying phenotypic diversity rather than by differential response of identical cells in different regions.

These two cases demonstrate that wildtype populations are behaviorally heterogeneous and that there exist subpopulations with differential performance. However, they also apparently suggest that low tumble bias is the superior strategy both with and without a gradient. This seemed to be unlikely to be true at extremely low tumble bias, since at zero tumble bias, cells are known to be non-chemotactic. To directly measure the performance of non-tumbling cells, we performed the assay with a mutant that is deleted for the response regulator CheY, without which they are permanently running (Figure 3–7). A gradient was not used since cells not expressing CheY are non-chemotactic (Sourjik & Berg, 2000).

The progress of the mean position over time of these cells was inferior to even the worst (i.e. highest) tumble bias subpopulation among wildtype cells climbing a gradient. The opposite was observed relative to the diffusing wildtype population, however, with non-tumbling cells performed at least as well as the best (i.e. lowest) tumble bias subpopulation. This identifies a key distinction that tumble bias can be reduced to zero for optimal diffusion, but a non-zero tumble bias is required for optimal gradient climbing.

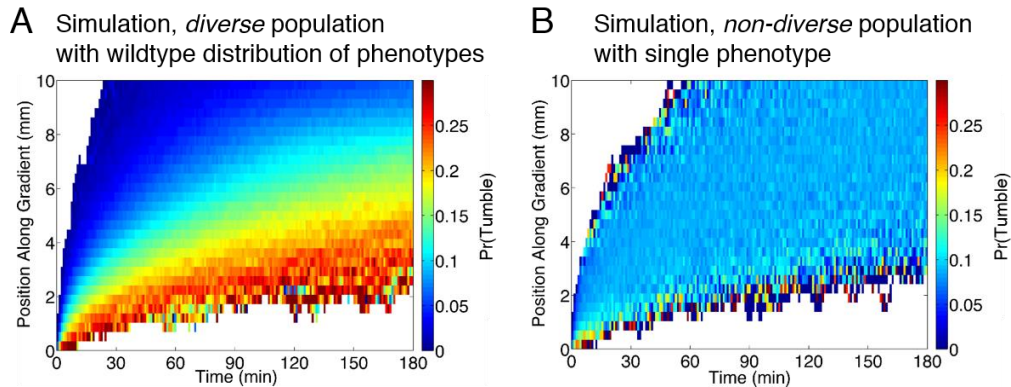


**Figure 3–6. Simulations of diverse or non-diverse populations in a microfluidic device.**

**A.** Simulation of virtual wildtype population in microfluidic gradient environment. Apparent tumble bias was calculated in the same way as the experiment: the probability of observing tumbles within a given space and time window. The distribution of phenotypes was slightly biased toward lower tumble bias because the model is based on single motor data and having multiple motors tends to slightly increase tumble bias. **B.** Same as A, but using a homogenous population consisting of a single phenotype with the mean tumble bias and adaptation time of the wildtype population. Note: Simulations were run by D. Chawla.

Another fundamental chemotactic task is to hold position near a source. To test this we reversed the direction of the gradient, with cells beginning at 1 mM methyl-aspartate and concentration tapering to 0 at the other end of the device. When placed in this negative gradient, the cell density was much more tightly constrained to the source than in the diffusion case, with no cells moving past 1 mm over the assay (Figure 3–5A). Despite the close-packing of cells, we still observed phenotypic separation of phenotypes (Figure 3–5B), behavioral variability (Figure 3–5C), and differential performance (Figure 3–5D), albeit on a 10-fold smaller length-scale. The rank order of performance by tumble bias was reversed relative to the other two cases, however, with the highest tumble bias cells maintaining mean position closest to the source. This suggests a trade-off between exploration for new sources and exploitation of sources once found.

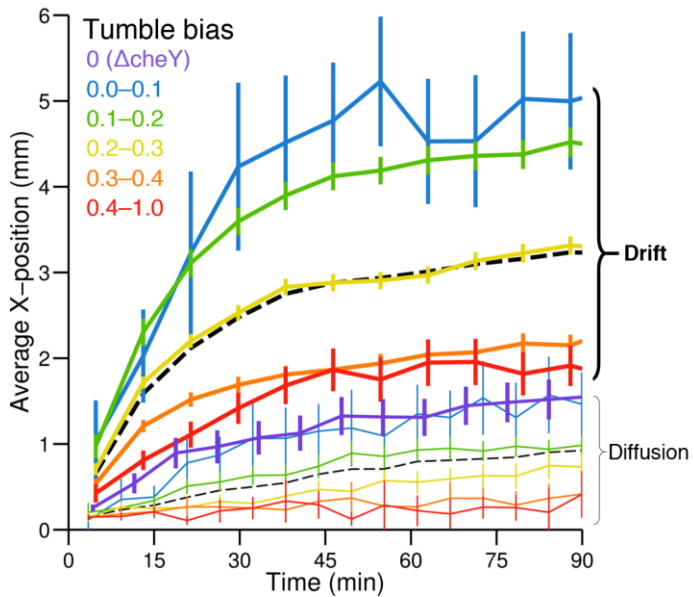


**Figure 3–7. Diffusion of non-tumbling cells compared to wildtype drift and diffusion.**

The thick purple line is the average position versus time of VS100 cells, a strain deleted for CheY which does not tumble, in no gradient. For comparison, the thick dashed black line is the mean position versus time of wildtype RP437 cells in a 0.1 mM/mm gradient of meAsp, with thick colored lines (except purple) that are cells of the same population binned on tumble bias as indicated. The thin lines are the same as the thick lines, except for the no-gradient case. Error bars are  $\pm 2 \times \text{SEM}$ . Diffusion and drift lines come from the same data from Figure 3–5, E and I respectively, with different binning to show finer resolution near zero tumble bias.

Tuning protein levels changes behavior and gradient-specific performance

Changes in protein concentration are known to change tumble bias and adaptation timescale (Kollmann, Lovdok, Bartholome, Timmer, & Sourjik, 2005; Korobkova, Emonet, Vilar, Shimizu, & Cluzel, 2004; Park et al., 2010), and theoretical work described in Part 2 suggests that the observed diversity in these parameters may be due to underlying stochasticity in the levels of proteins. For example, the adaptation enzyme CheR controls not only the rate of adaptation, but also the steady-state activity of the receptors. Hence variability in CheR is implicated as a factor underlying chemotactic diversity. We constructed a strain

that was deleted for native CheR and expressed CheR fused to mCherry from the chromosomal *lac* operon. By growing the cells with lower or higher levels of the *lac* inducer IPTG, populations had lower or higher distributions of tumble bias (Figure 3–8D). For a higher IPTG level, the tumble bias distribution was very close to that of the wildtype population, with a lower IPTG level resulting in a population that was shifted toward zero tumble bias.

We sought to use this strain and the wildtype strain to establish a mapping between protein concentration, tumble bias, and drift velocity in different gradients. To do so, we needed a device that could measure the steady-state velocity of cells climbing a wide range of gradients. We created a device that had a large source chamber, a large sink chamber, and a 1 mm long by 1 mm wide by 100  $\mu\text{m}$  deep bridge between them over which a gradient was established (Figure 3–8AB). Cells were loaded uniformly throughout the device and cell flux was imaged across the bridge and quantified using phase-differential microscopy (Colin, Zhang, & Wilson, 2014). By repeating the experiment with different concentrations in the source, different steepness of the gradient was achieved, and drift velocity was measured in each case. Here the gradient steepness was defined in terms of the change in receptor free energy in order to linearize the relationship between gradient steep and drift velocity (Figure 3–8C, Methods). In order to correct for differences in cell speed between experiments, the gradient steepness and drift velocity were appropriately adjusted by the cell speed (Methods). Linear regression was performed to extract the relationship between gradient steepness and drift velocity (Figure 3–8E). In all cases, steeper gradients elicited higher drift velocity from the same population.

Reflecting their identical distributions of tumble bias, the gradient–performance relationship of the high CheR induction cells matched that of the wildtype cells. This relationship was significantly different in low CheR induction cells. Importantly, the performance line of low CheR cells crosses that of high CheR and wildtype cells. As such, low CheR cells had higher performance in shallow gradients whereas high CheR and wildtype cells had higher performance in steep gradients.

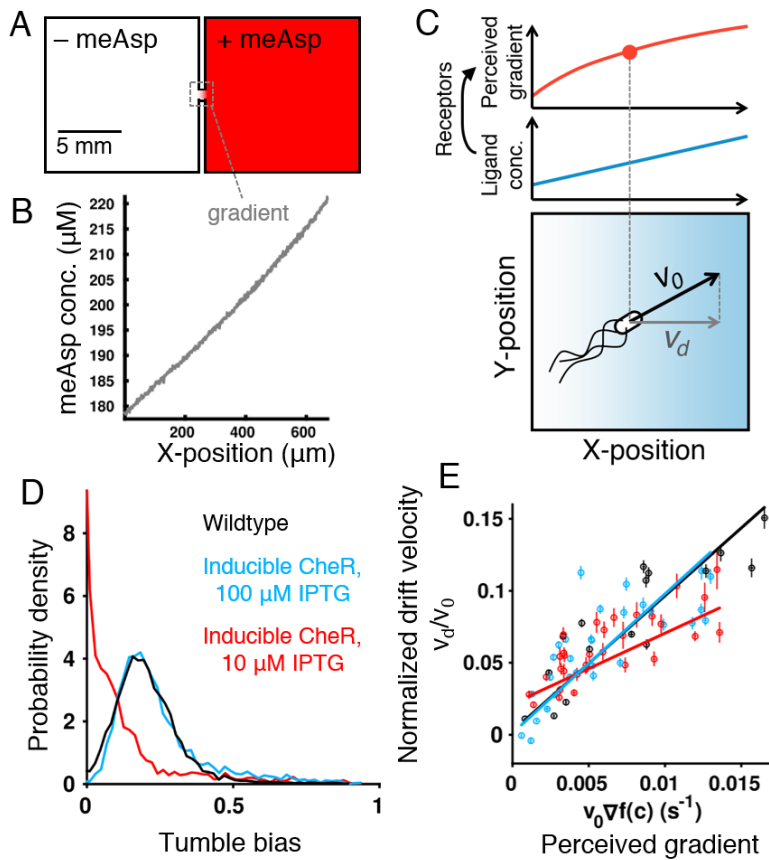


**Figure 3–8. CheR expression affects phenotypic distribution and chemotactic performance.**

**A.** Two-chambered PDMS devices were used to generate stable, linear gradients of different steepness. Movies were captured of swimming cells (100 s at 10X and 100 fps) in the gradient region (gray dashed box). **B.** Gradient steepness determined by averaging images of fluorescein, taken before and after the video. **C.** Cartoon diagram of drift velocity,  $V_d$ , cell speed,  $v_0$ , and perceived gradient,  $\nabla f(c)$ , via nonlinear chemoreception of the meAsp gradient. **D.** Induction of mCherry-CheR expression (red) in TE230 cells with 10  $\mu\text{M}$  IPTG results in a very low tumble bias distribution. Increasing induction to 100  $\mu\text{M}$  (light blue) shifts the tumble bias distribution up to overlap with the wildtype distribution (black). **E.** ΦDM (Colin et al., 2014) was used to determine population drift velocity. Cell speed was used to normalize drift velocity and adjust the perceived gradient in order to combine experiments. Cells with wildtype tumble bias (black) or TE230 induced to a similar distribution (blue) perform better in steep gradients, while TE230 induced to have lower tumble bias than wildtype (red) perform better in shallow gradients. Lines: weighted linear regression. Error on points: 2xSEM. Note: Data gathered by A. J. Waite.

This suggests a specialization for different gradients that originates in different levels of protein and is consistent with expectations based on theory. These predictions are that steep gradients require higher tumble bias and shorter adaptation time for optimal performance than in shallow gradients, which is reflected here in the differential performance of different CheR expression levels.

## Discussion

One of the earliest major findings in the study of bacterial chemotaxis was that different cells in a clonal population take different amounts of time to respond to the same stimulus (Spudich & Koshland, 1976). This study arguably served as the conceptual basis for future studies of single-cell heterogeneity. Decades later, we understand much more about the molecular components of the pathway, but still the functional consequences of variability in these components had only been discussed theoretically (Levin, Morton-Firth, Abouhamad, Bourret, & Bray, 1998). Here, we provide experimental evidence that this variability results in clonal populations assorting by phenotype over space and time, with different phenotypes performing better depending on the environment.

The fact that different CheR concentrations produced specialization for different gradient steepness is consistent with theoretically predicted trade-offs (Dufour et al., 2014). For optimal drift velocity, cells must achieve maximum contrast between run duration up and run duration down the gradient, which is only possible if the adaptation time and tumble bias are appropriately matched to the gradient slope. Specifically, fast adaptation time and high tumble bias tend to place cells in the correct operating regime when in steep gradients, and the opposite parameters are required for shallow gradients. This is reflected in our result that cells expressing high levels of CheR, which increases tumble bias and decreases adaptation time, perform better in steep gradients while cells with low levels perform better in shallow ones.

Simulations in Part 2 have predicted that there are trade-offs between sources that appear near cells versus far away (Frankel et al., 2014), and this is largely borne out in our

experimental comparison between positive and negative gradients. Following simulations results, the highest tumble bias cells perform best when the cells are at the source because of their reduced diffusivity, whereas lower tumble bias cells conversely have a better chance of making it to a faraway source.

## Methods

### Modified high-throughput capillary assay

We used either wildtype RP437 or TE26, a RP437-derived CheR deletion strain with a low-copy plasmid encoding IPTG-inducible expression of YFP-CheR and ampicillin resistance. Frozen stocks were streaked on LB for RP437 or LB with ampicillin for TE26. Single colonies were picked and grown overnight in tryptone broth (TB) for RP437 or TB with ampicillin for TE26. Overnight saturated cultures were subcultured in 20 ml of TB and grown to mid-exponential phase (about 4 hours). If TE26 was used, ampicillin and IPTG was added to the TB. Cells were then washed three times in motility medium (MM; phosphate buffer pH 7.0 with 0.1 mM EDTA and 0.01 mM L-methionine) by centrifugation in a benchtop centrifuge for 5 min at 3 krpm and resuspended in MM and diluted to an equivalent OD of 0.01.

We followed the high-throughput capillary assay designed by Bainer et al. (2003) and Park et al. (2011). Briefly, a 96-well-plate pipetting device consisting of 96 nozzles was fitted with 96 syringe needles that served as the capillaries. A syringe pump was attached to a port on the device that allowed liquid to be drawn in or pushed out of the needles simultaneously.

A 96-well plate was filled with different attractant conditions to be used inside the capillaries. Here we used different concentrations of aspartate in motility medium (MM; phosphate buffer pH 7.0 with 0.1 mM EDTA and 0.01 mM L-methionine). The 96 capillary array was placed in the plate and the syringe pump was used to fill the capillaries.

The capillary array was then transferred to another 96-well plate with each well containing 200  $\mu$ l of washed, diluted cells in MM. A spacer was used that ensured that the tip of the capillary was submerged a few millimeters into the well. Once the capillaries were submerged,

the apparatus was incubated for 30 min at 30°C. For the standard assay, the apparatus was then transferred to a 96-well plate that had 200 µl Luria broth (LB) growth media in each well and the contents of the capillaries was expelled. The plate of LB plus capillary contents was then grown overnight in a plate reader with continuous shaking at 37°C and OD<sub>600</sub> measured every 10 minutes. This produced a growth curve for each well, and the time at maximum growth velocity was used to measure the number of initial cells via the following calibration method.

To calibrate, different known dilutions of cells were grown in LB in the plate reader and the same preparations were serially diluted and plated on LB agar. Colonies were counted by scanning agar plates and using standard image analysis methods in MATLAB consisting of thresholding, Gaussian filtering, and watershed region counting.

For the single-cell version of the experiment, to measure the distribution of fluorescence in winning subpopulations, after the 30 minute incubation, the capillary apparatus was purged onto a dry 96-well plate and the droplets of liquid were carefully recovered by pipetting, then replicate wells were combined and spotted onto pads made from 1% agarose in MM. Cells were imaged at 100X magnification in phase contrast and in fluorescence through a YFP filter set and high pressure mercury lamp. MicrobeTracker (Sliusarenko, Heinritz, Emonet, & Jacobs-Wagner, 2011) software in MATLAB was used to quantify fluorescence intensity per area in cells.

### Microfluidic device design and fabrication

Microfluidic devices were constructed from the biocompatible and oxygen-permeable silicone elastomer polydimethylsiloxane (PDMS) on coverglass following standard soft lithography protocols for two-layer devices with Quake valves (Figure 3–9) (Melin & Quake, 2007). The master molds for the device consisted of two silicon wafers with features created using ultraviolet (UV) photoresist lithography in a class 100 cleanroom (Becton, Yale University). The bottom wafer had features for the sample channels (i.e. those through which cells, buffers, and chemoattractants were flowed) and was created using SU-8 negative resist.

Portions of the sample layer that were designed be opened and closed by pressure actuated valves were created with a second coat of SPR positive resist on the same wafer. The exception was that the region to be pinched off by the large gate that was used to detained cells on one side of the main chamber was made using SU-8, not SPR. The second, top wafer contained features for the control channels that close the collapsible features in by the bottom wafer. The top wafer was created using SU-8 negative resist.

Silicon wafers were first cleaned using buffered oxide etch, then spin-coated with the abovementioned photoresists using manufacturer specifications to achieve 10  $\mu\text{m}$  layers of each photoresist. The resists were then cured using UV light exposure through photomasks designed in CAD software and printed by CAD/Art Services Inc. (Bandon, Oregon), again following photoresist manufacturer specifications. Subsequently, wafers were baked and the uncured photoresist was dissolved. After curing the SPR coat, the features were then baked further to produce a rounded profile to ensure complete valve closure. After both wafers were complete, a protective coat of silane was applied by vapor deposition.

To cast and manufacture the two-layer device, the top wafer was coated with a 5 mm thick layer of degassed 10:1 PDMS-to-curing agent ratio, both provided from a kit (Sylgard 184, Dow Corning). For the bottom layer, a 20:1 mixture was prepared and spin coated to create an even 100  $\mu\text{m}$  thick layer. The two layers were partially baked for 45 minutes at 70°C. The top layer was then cut and separated from the wafer, holes were punched using a sharpened 20 gauge blunt-tip needle to make external connections to the control valve lines, then aligned and laminated onto the bottom layer. The stacked layers were baked together for 2 hours at 70°C and cooled overnight. The laminated layers were then cut out and punched to make external connections with the sample lines.

To complete the device, the cut and punched PDMS devices were bonded to coverglass. The PDMS was cleaned of fingerprints and dust using office tape followed by rinsing with isopropanol, methanol, then Millipore filtered water. The glass was rinsed with acetone, isopropanol, methanol, then Millipore filtered water. The two pieces were plasma treated for

60 seconds (Harrick Plasma, Ithaca, NY), laminated, then baked on a 80°C hotplate for 30 minutes to establish a covalent bond. Before use, the chambers were incubated at room temperature for at least 24 hours to ensure robust polymerization of the hydrogel within the device described in the next section.

#### Microfluidic gradient experiment

For microfluidic chemotaxis assays, cells were streaked from frozen stocks onto LB agar plates. Colonies were picked and grown overnight to saturation in M9-Glycerol medium (M9G; standard M9 salts supplemented with 1%w/v glycerol and 0.1%w/v casein hydrolysate), then diluted into fresh M9G media in a volume of 15–20 ml and regrown to mid-exponential phase ( $OD_{600} = 0.15$ ) with shaking at 30°C. Cells were then washed 3 times in chemotaxis buffer (CB; M9 salts with 0.1 mM EDTA, 0.01 mM L-methionine, and 10 mM DL-lactate, 0.05%w/v polyvinylpyrrolidone-40). This was done by centrifugation for 5 min at 3 krpm in a benchtop centrifuge, supernatant was aspirated, and pellet resuspended in 1 ml CB gently by agitation without pipetting. The cells were finally resuspended in 0.5 ml of CB, corresponding to an  $OD_{600}$  of 3–4. For the negative gradient experiment, cells were washed and resuspended in CB with 1 mM methyl-aspartate and 10  $\mu$ M fluorescein.

Before setting up the device, it was first injected with 5  $\mu$ l 10%w/v benzophenone in acetone, which was allowed to absorb into the PDMS for about 15 minutes. This organic photoinitiator permeated the PDMS and ensured robust hydrogel polymerization at the fluid–PDMS interface.

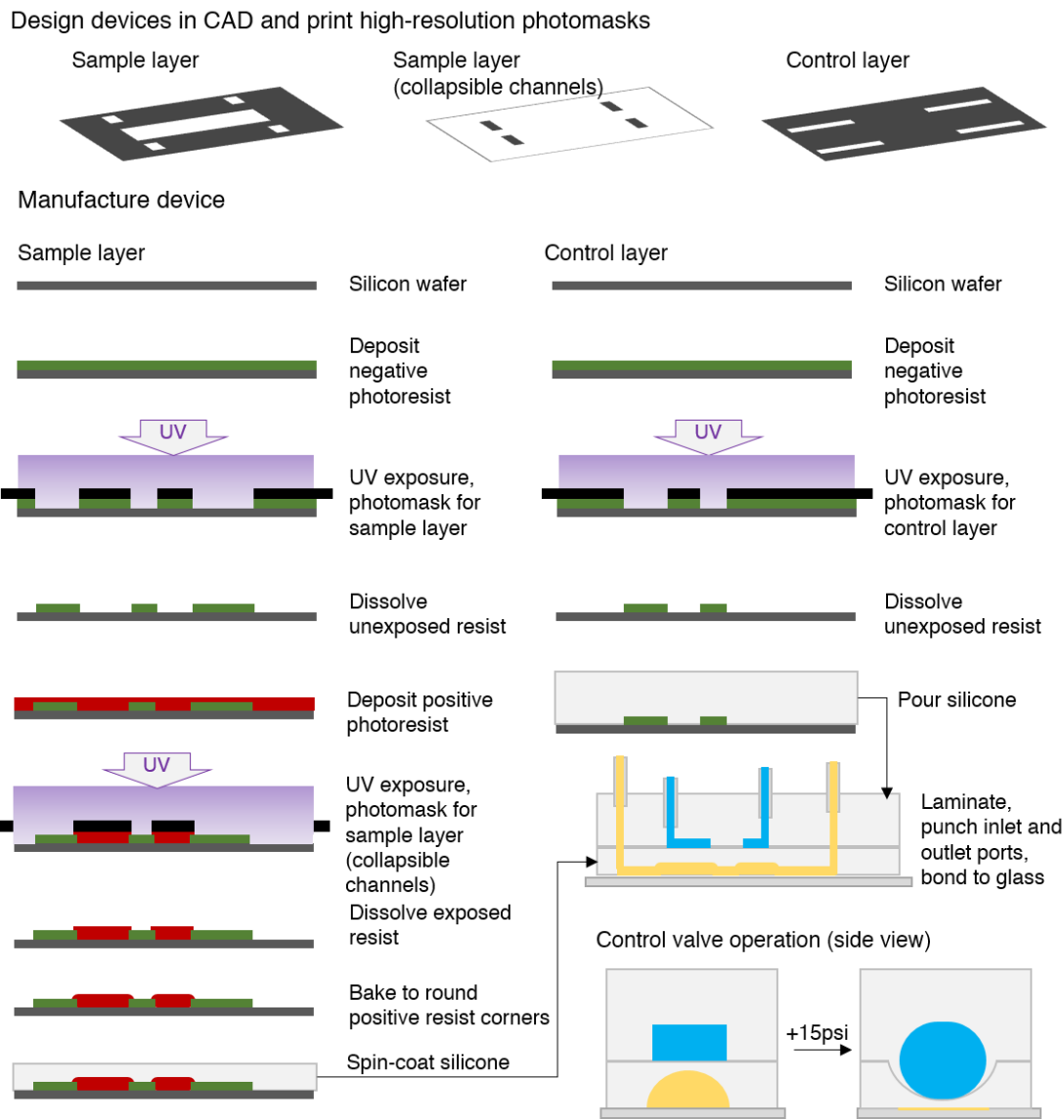


**Figure 3–9. Fabrication of two-layer PDMS microfluidic devices**

Standard protocol for creating devices with Quake valves: pneumatically-operated control gates (lower right corner). Two wafers are made, one for the sample channels (left column), and one for the control valves (right column). Unlike the control wafer, the sample wafer uses a second mask (top row) for a second photoresist in addition to the standard negative photoresist (green). This positive resist (red), when subjected to additional baking will round its profile, allowing it to be completely collapsed under vertical deformation (lower right corner). After wafers are made, they are used to cast PDMS (light gray), a silicone polymer that is somewhat flexible, permeable to oxygen, but impermeable to aqueous solutions, and which is generally considered biocompatible for experimental purposes.

Sample lines were connected to reservoirs mounted on a manifold of manual stopcocks allowing for independent selection between tank pressure regulated at tunable 0-3 psi of compressed nitrogen (“on”) or atmospheric pressure (“off”). The lines were primed and reservoirs filled by introducing negative pressure into the manifold through an auxiliary port and subsequently connected to the PDMS device via stainless steel 20 gauge connector blunt stubs. The valve lines were similarly set-up, except all lines were filled halfway with water, no reservoirs were used, the manifold had computer-controlled solenoid valves, and the tank pressure was regulated to 15 psi.

Hydrogel walls were created by polymerization of photoreactive derivative of poly(ethylene glycol) (PEG) using UV light, which was delivered from a high pressure mercury lamp or a UV LED illuminator (SOLA light engine from Lumencor, Beaverton, OR) through a DAPI filter block. The chamber was first flooded with wall solution (10% v/v PEG-diacrylate 700 average molecular weight, 0.05% w/v LAP photoinitiator, and 1 ng/ml resorufin) introduced through one of the sample lines. Stopping down the microscope back aperture allowed us to expose a small circle within the frame about 100  $\mu\text{m}$  in diameter through a 10X objective. Using continuous exposure and an automated stage, a stripe of hydrogel polymerization was “drawn” across the device to make the wall. The chamber was then flushed with CB from a different sample line until no resorufin dye remained (about 60 min).

Source and sink solutions were continuously circulated on either side of the observation chamber through channels that were separated by the hydrogel walls so that diffusion was possible without cross flow. In both the gradient and no-gradient experiments, the sink solution was CB. In the gradient case, 1 mM methyl-aspartate and 10  $\mu\text{M}$  fluorescein in CB was used as the source, whereas in the no-gradient case, CB was used. Six hours of circulation was performed before starting the experiment in order to establish and stabilize the gradient. For the negative gradient, the sink and source solutions were reversed.

Cells were then loaded into one of the sample line reservoirs and cycled into a section of device separate from the main channel to avoid disturbing the gradient. The cell-retaining gate

was then closed and cells were flowed into a narrow strip on the starting side of the main channel behind the gate. All valves surrounding the main channel were then closed, and the experiment was started by simultaneously beginning the automated acquisition and opening the cell-retaining gate.

A custom written MATLAB script was used to control the automated stage (Prior) of the microscope (Nikon Ti) via the MicroManager interface (<https://www.micro-manager.org/>). The script acquired movies across the device in a tiling fashion at 10x such that each frame was about 1 mm wide and the difference between acquisition positions was about 1 mm. At each position, 1 minute of phase contrast video was acquired to capture cell swimming preceded and followed by a single frame of fluorescence acquired through the YFP block to capture the fluorescein gradient. Fluorescein has approximately the same diffusion coefficient as methyl-aspartate, making it a good indicator of the methyl-aspartate gradient in the device. This main channel was scanned in this manner over 8 mm for the positive gradient (5 mm for no-gradient, 3 mm for negative gradient) and over 3 hours after the cell-retaining gate was lifted.

The illumination source for fluorescence was an LED illuminator (SOLA light engine from Lumencor, Beaverton, OR). Movies were recorded using an EM-CCD camera (Andor) at 1024 x 1024 resolution to a striped hard disk array in a Dell workstation at 8 fps

Single-cell tracking and run/tumble processing.

Since cell bodies in phase contrast microscopy are dark, we identified objects by thresholding on pixels intensity 6 standard deviations darker than the mean of the distribution of all pixel intensities in the frame. To find the center of the resulting objects, we used the radial-symmetry-center method described by R. Parthasarathy and available at [http://physics.uoregon.edu/~raghu/particle\\_tracking.html](http://physics.uoregon.edu/~raghu/particle_tracking.html). We tracked the motions of objects from frame to frame using the U-track software package developed by G. Danuser and available at <http://lccb.hms.harvard.edu/software.html>.

We created a MATLAB script that identified runs and tumbles in individual trajectories. For every point-to-point transition, we calculated the speed and the acceleration. These two

quantities were normalized by the mean run speed. We also calculated the angular velocity. We then fit these 3 variables with a sum of trivariate Gaussians (i.e. 3 Gaussians in a 3-variable domain). Points corresponding to runs occupied different regions of this space than do those corresponding to tumbles, so we then used clustering to assign run or tumble state probabilities to each point based on its position relative to the tri-Gaussian model. Since mean run speed is not initially known, an educated guess was used, then iterations of fitting and clustering are performed to refine the run and tumble assignments. The fitted trivariate Gaussian model was also refined by developing a reference data set with thousands of trajectories of wildtype cells swimming on slides in the absence of stimulus.

### Analysis of trajectories

Each microfluidic gradient experiment produced roughly 150 short movies of cells swimming throughout the device. Tracking and run/tumble processing was run on all movies at the Yale High Performance Computing facility or on Dell workstations. Filtering was done to remove non-cell objects that met certain criteria: run speeds that were less than 5 or greater than 40  $\mu\text{m/s}$  and mean squared displacement that was less than 50  $\mu\text{m}^2/\text{s}$ . Within-movie positions were added to stage positions to localize individual tracks within the device. This summing was also done on time information to achieve spatiotemporal positioning of cells throughout the device.

Movies were subdivided into 6 to 10 spatial bins along the gradient axis, depending on the experiment, to calculate the cell density and average tumble bias across the device. Whenever we calculated an average across trajectories, we weighted by the trajectory duration. For measurements that involved binning on tumble bias, only tracks with tumble bias falling in a certain range were screened out and analyzed as above. For all kymographs and heat maps that are shown over a continuous space-time domain, values at additional space and time points between measured movies were linearly interpolated from the data using the linear ScatteredInterpolant method in MATLAB.

To calculate the mean position as a function of time, we took each scan of the microscopy stage across the device as a single time point. The average position of all cells detected in each scan was calculated to produce the mean position. The time points are determined by the temporal midpoint of each stage scan. To calculate the mean position of individual bins of tumble bias, only cells with a certain tumble bias had their positions averaged.

The shape of the methyl-aspartate gradient was reconstructed from the fluorescein images by first normalizing each image to a flat-field image acquired in a uniform fluorescence field (typically fluorescence reference slides from Ted Pella, Redding, CA) to correct for systematic distortions in fluorescence illumination across the frame, then rescaling to minimum and maximum fluorescence measurements captured at the source and sink circulation loops of the device. The intensity profile was averaged across the non-gradient direction to produce a 1-D profile along the gradient axis for each fluorescence image. Then, using the time and position at which the frame was captured during the experiment, these were assembled into a 2-D space-time matrix of concentration.

#### Simulations of cell behavior in microfluidic device geometry

The same cell model and simulation framework from Part 2 were used. Phenotypes in the virtual wildtype population were generated from the fit to wildtype data (Figure 2–1) (Frankel et al., 2014). The single phenotype used for the homogenous population was the mean tumble bias and mean adaptation time of the wildtype model. Note that this model is slightly shifted toward lower tumble bias compared to our experimental wildtype cells because it is based on single motor clockwise bias data. The free swimming cells in our experiment have multiple flagella, which very slightly increases the tumble bias relative to single motor clockwise bias (Mears et al., 2014; Sneddon, Pontius, & Emonet, 2012).

New boundary conditions were added to match the experimental device. The environment was bounded as follows: x from 0 to 10000  $\mu\text{m}$ , y from 0 to 1000  $\mu\text{m}$ , and z from 0 to 10  $\mu\text{m}$ . The x boundaries were reflecting. The y boundaries were toroidal. The z boundaries were “aligning”: cells attempting to cross the “floor” or “ceiling” of the device had their heading

vector reoriented to lie in the z plane. Following the microfluidic device design, this condition prevented cells from traveling perpendicular to the gradient for extended periods of time in the z dimension and constrained them roughly in a single z plane. The aligning condition was not used for the y boundaries to avoid unnecessary computational overhead in resolving edge and corner crossings, and since the experimental geometry actually permits cells to run perpendicular to the gradient in the y direction for some time.

To match the experiment's initial condition, cell positions were initialized within a small stripe inside the virtual device: x from 0 to 100  $\mu\text{m}$  and across the device in y. Within that region, positions and headings were randomized. A linear gradient of meAsp from 0 to 1 mM was applied and cells were pre-equilibrated while being held in place with random orientations. At time 0, they were allowed to swim. After a 180 minute simulation, all trajectories of all cells were broken into space–time bins exactly as if movies had been acquired. The average apparent tumble bias within each bin was calculated as if from experimental data.

#### Construction of strain with inducible CheR expression

Cells were grown in standard recipes for Luria broth (LB), Super-optimal broth (SOB), or SOB with catabolite repression (SOC) as specified. Plates were made with media plus 1.5% agar and antibiotics as specified. We found that RP437 has an extremely low recombination efficiency compared to MG1655, so we first recombined the insert into MG1655 then used P1 phage transduction to transfer the insert to RP437.

Gibson assembly (Gibson et al., 2009) was used to create a plasmid containing the recombination insert. The complete insert consisted of a *mCherry::cheR* fusion sequence followed by an FRT-sequence-bounded kanamycin resistance cassette. The *mCherry* fragment was PCR amplified from pTE46. The *cheR* fragment was PCR amplified from RP437 genomic DNA. The FRT-*kanR*-FRT cassette was PCR amplified from pCP15 (Cherepanov & Wackernagel, 1995). The vector for the final plasmid construct was pUC19.

The assembled recombination insert was PCR amplified from the resulting plasmid with primers containing homology for the region following chromosomal *pLac* in MG1655. Linear

insert fragments were gel purified. They were PCR amplified again from the fragment using the same template and gel purified again. Before transforming with the fragment, MG1655 cells were first transformed with pKD46 (Datsenko & Wanner, 2000) encoding a lambda-red recombinase cassette, and selected on LB with ampicillin (100 µg/ml) plates at 30°C. Then an overnight culture was prepared in 5 ml SOC with 100 µg/ml ampicillin. To 5 ml SOB with 100 µg/ml ampicillin and 1 mM arabinose or with no arabinose, 10 µl of overnight culture was added and grown to OD 0.6 (about 3 hours). The subculture was centrifuged at 6krpm for 7.5 minutes at 4°C and the supernatant aspirated. The pellet was washed with 1 ml 10% glycerol in a 4°C temperature-controlled room 3 times by centrifugation for 3 min at 6 krpm, then resuspended in 50 µl 10% glycerol. To the suspension 1 µg of recombination insert fragment DNA was added and electroporated, followed by immediate recovery in 1 ml SOC at 37°C for 2 hours. The culture was then washed twice with 1 ml M63 salts by centrifugation for 3 min at 6krpm, then resuspended in 100 µl of M63 salts and spread on LB agar with kanamycin 50µg/ml. Plates were incubated overnight at 43°C to remove pKD46. Colonies were streaked out twice on LB agar with 50µg/ml kanamycin to purify and screened for ampicillin sensitivity. The insertion site was PCR amplified from a genomic DNA prep and verified by sequencing.

To create the P1 phage donor lysate, overnight saturated culture of the donor strain in LB was first diluted 1:100 into 3 ml transduction growth medium (TG; LB with 5 mM CaCl<sub>2</sub> and 0.2%w/v glucose). The subculture was grown 30 min at 37°C, then 75 µl P1 phage stock was added and incubated for 3 hours. Subsequently 10 µl of chloroform was added. The sample was then pelleted and the aqueous supernatant was saved and stored at 4°C.

In order to transduce mutations from donor lysate into the recipient strain, the overnight saturated culture in LB of the recipient strain was diluted 1:100 into 10 ml TG until late exponential phase at 37°C. The cells were pelleted and resuspended in 2.5 ml transduction reaction medium (TR; LB with 5 mM CaCl<sub>2</sub> and 100 mM MgSO<sub>4</sub>). A dilution series was prepared from 1:1:0 up to 1:0:1 of recipient cells, TR, and donor lysate in a total volume of 200 µl. Transduction reactions were incubated without shaking at 37°C for 30 min. The cells were

then grown in 1 ml of LB combined with 200 µl of 1 M sodium citrate pH 5.5 for 1 hour at 37°C with shaking. The cells were then pelleted and resuspended in 100 µl transduction selection medium (TS; LB with 20 mM sodium citrate) and plated on TS agar with 25 µg/ml kanamycin and grown overnight at 37°C. Large colonies were selected and colony-purified twice on TS agar and 25 µg/ml kanamycin.

Following transduction, the KanR marker was removed via FRT excision by first transforming with pCP20 and selecting on LB 100 µg/ml Amp at 30°C overnight to remove the FRT-bounded region, then re-streaking on LB with no antibiotic and growing overnight at 43°C to remove pCP20. Sensitivity to kanamycin and to ampicillin were then verified. This strain was dubbed TE230.

#### Measurement of drift velocity via phase-differential microscopy

Note: this assay was performed by Adam Waite. Devices were designed following Colin et al. (2014), using the fabrication methods described above under “Microfluidic device design and fabrication.” The side chambers were 15 mm x 15 mm with a depth of 100 µm with a bridge between them that was 1 mm long.

Cells were grown exactly as in the microfluidic gradient experiment, except that, when TE230 was used, IPTG was added to the liquid growth medium. Mid-exponential-phase cells were split into two aliquots, then pelleted and resuspended in either CB or CB plus methyl-asparate and fluorescein. The ratio of methyl-asparate and fluorescein was held constant but the total concentration was varied across experiments to achieve different gradients that were still directly comparable in fluorescence measurements. The buffer-only cells were loaded into one chamber and the other preparation into the other chamber, then the device was sealed and incubated 90 minutes at 30°C to allow the gradient and cell flux to reach steady-state across the bridge.

The device was then placed on the inverted fluorescence microscope with a 10X objective and 100-second-long phase contrast movies were captured at the bridge with fluorescence stills of the gradient being taken before and after. Fluorescence illumination was done with a SOLA

light engine. Movies were recorded using a CMOS (Hamamatsu) camera at 512 x 512 resolution to a striped hard disk array in a Dell workstation at 100 fps.

The resultant movies contained a dense and deep field of cells from which we calculated the drift velocity using the ΦDM technique described by Colin, et al. (2014). Briefly, the Fourier transform of the images was taken and the phase shift over time was calculated. To calculate the cell speed required to normalize the result from one experiment to the next, we first thresholded the pixel intensity of each frame of the phase contrast image was to isolate only the in-plane cells. From these we used the particle tracking described above under “Computational analysis of single-cell trajectories” to generate short trajectories that gave short measurements of speed which were averaged together across all trajectories across the experiment.

In order to calculate the gradient steepness, it was necessary to correct for the fact that the sensitivity of the receptors to chemoattractant is sigmoidal (Sourjik & Berg, 2002). Following Colin, et al. and others, we used a standard MWC model of the change in receptor free energy as a function of methyl-aspartate concentration  $f(c) = \ln[(K_I + c)/(K_A + c)]$ , where  $K_I = 18 \mu\text{M}$  is the binding affinity of the inactive receptors and  $K_A = 3 \mu\text{M}$  is the binding affinity of the active receptors for meAsp. For each movie, we fit this function to the gradient profile in order to extract the gradient of the receptor free energy,  $\nabla f(c)$ , which was used as the effective gradient as sensed by the cells. This quantity was multiplied by the cell speed, which directly determines the rate at which the cells perceive the gradient, to normalize between experiments.

Three types of cells were used: wildtype cells, TE230 cells with 10  $\mu\text{M}$  IPTG, and TE230 with 100  $\mu\text{M}$  IPTG. For each type, many ΦDM experiments were performed by altering the concentration of methyl-aspartate that was added to one side to create different gradients. Linear regression was then performed on the drift velocity versus gradient data for each cell type. Distributions of tumble bias of these cells were also measured at the time of the

experiment by placing 10  $\mu$ l diluted cell preparation on a glass slide without a gradient and taking several 2 minute movies and analyzing trajectories for tumble bias.

## References

- Bainer, R., Park, H., & Cluzel, P. (2003). A high-throughput capillary assay for bacterial chemotaxis. *J Microbiol Methods*, 55(1), 315-319.
- Cherepanov, P. P., & Wackernagel, W. (1995). Gene disruption in Escherichia coli: TcR and KmR cassettes with the option of Flp-catalyzed excision of the antibiotic-resistance determinant. *Gene*, 158(1), 9-14.
- Cluzel, P., Surette, M., & Leibler, S. (2000). An ultrasensitive bacterial motor revealed by monitoring signaling proteins in single cells. *Science*, 287(5458), 1652-1655.
- Colin, R., Zhang, R., & Wilson, L. G. (2014). Fast, high-throughput measurement of collective behaviour in a bacterial population. *Journal of the Royal Society Interface*, 11(98). doi: Artn 20140486 Doi 10.1098/rsif.2014.0486
- Datsenko, K. A., & Wanner, B. L. (2000). One-step inactivation of chromosomal genes in Escherichia coli K-12 using PCR products. *Proc Natl Acad Sci U S A*, 97(12), 6640-6645. doi: 10.1073/pnas.120163297
- Dufour, Y. S., Fu, X., Hernandez-Nunez, L., & Emonet, T. (2014). Limits of feedback control in bacterial chemotaxis. *PLoS Comput Biol*, 10(6), e1003694. doi: 10.1371/journal.pcbi.1003694
- Eliassen, S., Jorgensen, C., Mangel, M., & Giske, J. (2007). Exploration or exploitation: life expectancy changes the value of learning in foraging strategies. *Oikos*, 116(3), 513-523. doi: DOI 10.1111/j.2006.0030-1299.15462.x
- Frankel, N. W., Pontius, W., Dufour, Y. S., Long, J., Hernandez-Nunez, L., & Emonet, T. (2014). Adaptability of non-genetic diversity in bacterial chemotaxis. *eLife*, 3. doi: 10.7554/eLife.03526

- Gibson, D. G., Young, L., Chuang, R. Y., Venter, J. C., Hutchison, C. A., 3rd, & Smith, H. O. (2009). Enzymatic assembly of DNA molecules up to several hundred kilobases. *Nat Methods*, 6(5), 343-345. doi: 10.1038/nmeth.1318
- Kollmann, M., Lovdok, L., Bartholome, K., Timmer, J., & Sourjik, V. (2005). Design principles of a bacterial signalling network. *Nature*, 438(7067), 504-507.
- Korobkova, E., Emonet, T., Vilar, J. M. G., Shimizu, T. S., & Cluzel, P. (2004). From molecular noise to behavioural variability in a single bacterium. *Nature*, 428(6982), 574-578. doi: Doi 10.1038/Nature02404
- Krakauer, D. C., & RodriguezGirones, M. A. (1995). Searching and learning in a random environment. *Journal of Theoretical Biology*, 177(4), 417-429. doi: DOI 10.1006/jtbi.1995.0258
- Levin, M. D., Morton-Firth, C. J., Abouhamad, W. N., Bourret, R. B., & Bray, D. (1998). Origins of individual swimming behavior in bacteria. *Biophysical journal*, 74(1), 175-181. doi: 10.1016/S0006-3495(98)77777-X
- Lewus, P., & Ford, R. M. (2001). Quantification of random motility and chemotaxis bacterial transport coefficients using individual-cell and population-scale assays. *Biotechnology and Bioengineering*, 75(3), 292-304. doi: Doi 10.1002/Bit.10021
- Mears, P. J., Koirala, S., Rao, C. V., Golding, I., & Chemla, Y. R. (2014). Escherichia coli swimming is robust against variations in flagellar number. *eLife*, 3, e01916. doi: 10.7554/eLife.01916
- Melin, J., & Quake, S. R. (2007). Microfluidic large-scale integration: the evolution of design rules for biological automation. *Annu Rev Biophys Biomol Struct*, 36, 213-231. doi: 10.1146/annurev.biophys.36.040306.132646
- Mesibov, R., & Adler, J. (1972). Chemotaxis toward Amino-Acids in Escherichia-Coli. *Journal of Bacteriology*, 112(1), 315-&.

- Park, H., Guet, C. C., Emonet, T., & Cluzel, P. (2011). Fine-Tuning of Chemotactic Response in *E. coli* Determined by High-Throughput Capillary Assay. *Current Microbiology*, 62(3), 764-769. doi: DOI 10.1007/s00284-010-9778-z
- Park, H., Pontius, W., Guet, C. C., Marko, J. F., Emonet, T., & Cluzel, P. (2010). Interdependence of behavioural variability and response to small stimuli in bacteria. *Nature*, 468(7325), 819-823. doi: 10.1038/nature09551
- Seymour, J. R., Marcos, & Stocker, R. (2009). Resource Patch Formation and Exploitation throughout the Marine Microbial Food Web. *American Naturalist*, 173(1), E15-E29. doi: Doi 10.1086/593004
- Sliusarenko, O., Heinritz, J., Emonet, T., & Jacobs-Wagner, C. (2011). High-throughput, subpixel precision analysis of bacterial morphogenesis and intracellular spatio-temporal dynamics. *Mol Microbiol*, 80(3), 612-627. doi: 10.1111/j.1365-2958.2011.07579.x
- Sneddon, M. W., Pontius, W., & Emonet, T. (2012). Stochastic coordination of multiple actuators reduces latency and improves chemotactic response in bacteria. *Proceedings of the National Academy of Sciences of the United States of America*, 109(3), 805-810. doi: 10.1073/pnas.1113706109
- Sourjik, V., & Berg, H. C. (2000). Localization of components of the chemotaxis machinery of *Escherichia coli* using fluorescent protein fusions. *Molecular Microbiology*, 37(4), 740-751. doi: DOI 10.1046/j.1365-2958.2000.02044.x
- Sourjik, V., & Berg, H. C. (2002). Receptor sensitivity in bacterial chemotaxis. *Proceedings of the National Academy of Sciences of the United States of America*, 99(1), 123-127. doi: DOI 10.1073/pnas.011589998
- Spudich, J. L., & Koshland, D. E. (1976). Non-Genetic Individuality - Chance in Single Cell. *Nature*, 262(5568), 467-471.
- Stocker, R., Seymour, J. R., Samadani, A., Hunt, D. E., & Polz, M. F. (2008). Rapid chemotactic response enables marine bacteria to exploit ephemeral microscale nutrient patches.

*Proceedings of the National Academy of Sciences of the United States of America*, 105(11),

4209-4214. doi: DOI 10.1073/pnas.0709765105

Taylor, J. R., & Stocker, R. (2012). Trade-Offs of Chemotactic Foraging in Turbulent Water.

*Science*, 338(6107), 675-679. doi: DOI 10.1126/science.1219417





## Part 4: Conclusion

Connecting simulations to experiments,  
molecules to behavior 

A new framework, a new starting point

Although the present study still leaves many facets of this topic unexplored, I hope that it will serve as a starting point for further investigations into the sources and consequences of phenotypic heterogeneity. With respect to bacterial chemotaxis, future experiments should establish correlations between protein concentration and behavior at the single-cell level to complete the mapping between molecules and behavior. At the population scale, selection on chemotactic performance in different environments could be performed in a laboratory evolution experiment to discern whether variability in performance provides a fitness advantage. Both of these projects are ongoing topics of research.

A new feature of this framework is that the relationship between genotype and phenotype has been expanded to allow consideration of the role of protein levels. While genotype broadly defined could be said to include both protein coding sequences and regulators of genetic noise, treating the role of protein levels as a separate step allowed us to quantitatively analyze the contribution of this noise apart from changes in the proteins themselves. We see applications of this approach in the evolutionary study of signal transduction, wherein cell-to-cell differences in the levels of signaling proteins may have an impact on behavior on par with changing the biochemistry of the proteins themselves (Ferrell, Tsai, & Yang, 2011).

While we have used *E. coli* as a model system due to the wealth of experimental data, the framework we develop here is also relevant to chemotaxis of other bacterial species and even of the cells of higher organisms. Multicellular organisms also exhibit different motion strategies in their constituent cells, from the singular approach of human sperm to the

different motility patterns of neutrophils as they navigate the body to sites of infection and capture invading organisms (Eisenbach & Lengeler, 2004). Our framework could be used to investigate several interesting questions in such systems: How does behavioral diversity of single cells affect the fitness of the organism, and when is the diversification of a single cell type supplanted by the commitment of a new developmental cell lineage?

## A broader perspective

All cellular navigation systems use the interactions of proteins to process information obtained from the environment and convert it into a decision about how to move. Variations in the amounts or stoichiometries of these proteins can therefore lead to variations in this decision-making process. As a result, whenever cells are moving, whether they be infectious bacteria on their way to a host tissue or immune cells on their way to intercept them, the genetic blueprint of the chemotaxis pathway is not sufficient to predict population behavior. Indeed, the deviations from the average behavior may themselves constitute an adaptive strategy.

Trade-offs may also exist in the chemotaxis behaviors of other human bacterial pathogens. The closely related chemotaxis system in *Salmonella enterica* is required for virulence (Stecher et al., 2004), as is the substantially different motility system of *Borrelia burgdorferi* (Sze, Zhang, Kariu, Pal, & Li, 2012). On the other hand, pathogens such as *Pseudomonas aeruginosa* have multiple motility systems to tackle different environments during infection (O'Toole & Kolter, 1998). It is possible that phenotypic diversification within a single navigation system may bridge the gap between one system and many by allowing populations to adapt to greater environmental variation without developing a new biological module.

From the simplest two-component systems to the most elaborate signal transduction cascades, proteins responsible for sensing environmental signals are usually distinct from those involved in making behavioral decisions. Often, the output of many types of receptor proteins are fed into a much smaller number of signal transduction pathways. While cells can

control their sensitivity to different signals by regulating the expression of different receptors, the integration of multiple signals through a central group of proteins will place conflicting demands on those core proteins. Thus, while horizontal integration is beautifully economical and a ubiquitous feature of biological pathways, our study illustrates that it is also likely to introduce trade-offs by design.

Finally, biology broadly speaking is replete with noise. Although the concept of non-genetic individuality may have been initially coined in reference to *E. coli* chemotaxis (Spudich & Koshland, 1976), we now know that many other biological systems exhibit substantial non-genetic cell-to-cell variability, including stem cell differentiation (Huang, 2009), bacterial sporulation (Maamar, Raj, & Dubnau, 2007), and cancer cell response to chemotherapy (Spencer, Gaudet, Albeck, Burke, & Sorger, 2009). Different systems may have different mechanistic drivers that create, constrain, and adapt this variability. In all cases, however, it is conceivable that through genetic changes to drivers of non-genetic diversity, populations of cells may achieve higher collective success in tackling biological trade-off problems. This form of diversity may constitute an evolutionary stepping stone on the path from one to multiple biological modules.

## References

- Eisenbach, Michael, & Lengeler, Joseph W. (2004). *Chemotaxis*. London: Imperial College Press.
- Ferrell, J. E., Jr., Tsai, T. Y., & Yang, Q. (2011). Modeling the cell cycle: why do certain circuits oscillate? *Cell*, 144(6), 874-885. doi: 10.1016/j.cell.2011.03.006
- Huang, S. (2009). Non-genetic heterogeneity of cells in development: more than just noise. *Development*, 136(23), 3853-3862. doi: Doi 10.1242/Dev.035139
- Maamar, H., Raj, A., & Dubnau, D. (2007). Noise in Gene Expression Determines Cell Fate in *Bacillus subtilis*. *Science*.

O'Toole, G. A., & Kolter, R. (1998). Flagellar and twitching motility are necessary for *Pseudomonas aeruginosa* biofilm development. *Mol Microbiol*, 30(2), 295-304.

Spencer, S. L., Gaudet, S., Albeck, J. G., Burke, J. M., & Sorger, P. K. (2009). Non-genetic origins of cell-to-cell variability in TRAIL-induced apoptosis. *Nature*, 459(7245), 428-432. doi: 10.1038/nature08012

Spudich, J. L., & Koshland, D. E. (1976). Non-Genetic Individuality - Chance in Single Cell. *Nature*, 262(5568), 467-471.

Stecher, B., Hapfelmeier, S., Muller, C., Kremer, M., Stallmach, T., & Hardt, W. D. (2004). Flagella and chemotaxis are required for efficient induction of *Salmonella enterica* serovar Typhimurium colitis in streptomycin-pretreated mice. *Infect Immun*, 72(7), 4138-4150. doi: 10.1128/IAI.72.7.4138-4150.2004

Sze, C. W., Zhang, K., Kariu, T., Pal, U., & Li, C. (2012). *Borrelia burgdorferi* needs chemotaxis to establish infection in mammals and to accomplish its enzootic cycle. *Infect Immun*, 80(7), 2485-2492. doi: 10.1128/IAI.00145-12



